The Power Harvesting Ratio: Design and Power Estimation of Vibration Energy Harvesters

By

Alexander Vadimovich Pedchenko

Dissertation

Submitted to the Faculty of the

Graduate School of Vanderbilt University

in partial fulfillment of the requirements

for the degree of

DOCTOR OF PHILOSOPHY

in

Mechanical Engineering

December, 2015

Nashville, Tennessee

Approved:

Eric Barth, Ph.D.

Thomas Withrow, Ph.D.

Michael Goldfarb, Ph.D.

Douglas Adams, Ph.D.

Kenneth Pence, Ph.D.

To my grandparents, for serving as examples of how knowledge betters a person.

To my parents and grandfather, for their much-appreciated support in all my endeavors.

In loving memory of my grandmother, who has positively impacted the education of many during her teaching career, but whose positive impact on my life is much greater than I could express with mere words.

ACKNOWLEDGMENTS

During my seven years of graduate school at Vanderbilt (I pursued a Master's during the first two, so please stop judging) I have come to accept that many things during this stage of my life were ephemeral in nature. I have seen friends come and go, roommates move in and move out, and have grieved over the loss of the most conveniently located Starbucks I have ever had the privilege of getting coffee at. However, the one aspect which I am glad to say has remained constant, is my relationship with my advisor. During all my time here, Eric Barth has remained a wise mentor, a caring support, and a great friend. I want to thank him for being all three though great success and stupendous failures, during pleasant coffee breaks and sleepless deadline chases, in good times and in bad, in sickness and in health (seven years is quite a commitment after all). But jokes aside, I don't know whether the work described in this dissertation would have been possible without Dr. Barth, but I do know that it would not have been possible for me to do it without him. For this, I offer him my warmest thanks.

During the course of my research my luck was not limited to my advisor. I am certain that the Vanderbilt Department of Mechanical Engineering has facilitated my pursuit of a doctoral degree to an extent other graduate students would probably find offensive. Starting with faculty, I want to thank Don Truex for kindly lending me his electrical expertise at a moment's notice on many occasions. I want to thank Suzanne Weiss for doing so much extra work on my behalf (I can never apologize enough for the plethora of forgotten deadlines) and providing the type of support one would only expect from family. In addition to my advisor, I want to thank the other members of my defense committee: Dr. Michael Goldfarb, Dr. Doug Adams, Dr. Kenneth Pence, and Dr. Thomas Withrow. Each was kind enough to not only serve on my committee, but to also offer invaluable advice for improving my research outside of the time they served as committee members. In addition to expressing my sincere gratitude to each of them, I want to give a special thanks to Dr. Adams and Dr. Withrow. The former for letting me make use of his expertise in the field of vibrations by providing crucial technical advice, lending lab equipment, and introducing me to the incredibly helpful and kind engineers at his research facility – the Laboratory for Systems and Integrity and Reliability. The latter for, in many ways, being my second adviser. Tom's work ethic, perfectionism, practical knowledge, critical thinking, humor, sense of fairness, and genuine nature have helped better both, my research, and myself. The help and support I have received from Dr. Withrow is second only to my adviser.

A great number of graduate students have made very significant contributions, be they direct or indirect, to this dissertational work. I want to start by thanking my colleague and first close friend I made in grad school – Mark Hofacker. His contribution to the herein presented research is quite significant, especially in regard to the physical design of the experimental harvester. I consider myself very fortunate to have worked with such an intelligent, dedicated, and humorous human being. I want to thank Bryn Pitt, as he was instrumental in securing my first journal publication. In-between bouts of his frequent ridicule (which I'm sure he thinks have made me stronger), he has shown genuine care and support which I have truly come to appreciate during the last few months of working on my dissertation. After discovering that I simply have to find more capable individuals to secure publications, I was very fortunate to meet Janette Meyer, a postdoctoral researcher at `Dr. Adam's lab. To say that the journal article in Section 0 would not have happened without her is not being kind, it's being objectively honest. Janette's expertise on collecting

vibration data was crucial to shifting my own perception of my research from as being completely theoretical to appearing to be highly practically applicable. Janette also made me aware that the difference in knowledge and wisdom between an experienced postdoc and a Ph.D. candidate is not unlike that existing between a college and a high school graduate. Her sharpness of mind and clever scientific approach have in many ways rekindled the awe of science I had when I first started graduate school. I want to thank Eissa Ledoux from Dr. Goldfarb's lab. Even though she was not directly involved in my research, she has aided me in many ways, especially during the last month. Her unparalleled work ethic and altruistic nature have allowed me to spend much more time to improve the quality of the present manuscript, while the kindness of her heart has raised my morale on countless occasions and have made me earnestly wish I had a sister like her. Lastly, I want to thank all the present and past member of Olin Hall 504. Even though, as I'm putting the finishing touches on my dissertation, I'm excitedly thinking of how happy I will be to finally graduate, I know I will miss "the lab." I have been incredibly lucky to have worked with such wonderful individuals and wish each one of them success and happiness in all of their future endeavors. I hope that this same success and happiness will also follow "the lab" itself for many, many years after I'm gone.

I am afraid that as I have listed member of the faculty and student body who were instrumental in helping me complete this work I have inevitably missed names. If I did so, please forgive me and write it off to sleep deprivation.

Many people mention their family when acknowledging those that have helped them in achieving their greatest accomplishments. I hypothesize that a very small portion of those people happen to be the only children that are rottenly spoiled. There is no doubt in my mind that I belong to this highly elite and mostly scoffed at subset. The amount of love, support, kindness and assistance that my family showered upon me during my research makes me believe that it is their names that belong after the "by" on the title page, instead of my own. I want to express my utmost gratitude to my mom and dad, Tanya and Vadim, who have done as much as humanly possible to make my life as easy and pleasant as it can be. I'd also like to thank my grandfather, Vasya, and my late grandmother, Nadya, for doing the same during the early stages of my life. I will never forget their kindness and love and can only hope that one day I will make as great of a parent and grandparent.

TABLE OF CONTENTS

LIST OF TABLES

LIST OF FIGURES

I. INTRODUCTION

1. Overview

The objective of the research described within this manuscript is to advance the field of vibration energy harvesting. Specifically, the sought improvement is a substantial increase in power generation of vibration energy harvesters from multifrequency excitation sources and excitation sources comprised of components the frequencies and/or amplitudes of which vary with time. This improvement is achieved via the development, experimental validation, and use of two new analytical tools/methods.

These two devised techniques use information about the expected frequency behavior of the excitation source, the dynamics of the harvester, and the dynamics of the harvester's electrical load to predict the harvester's dynamic stability and average power generation. Provided the dynamics of the harvester and its electrical load are linear, these tools can be used to optimize the harvester's power generation, or to quickly calculate the expected average power generation of unique or unusual harvester architectures.

2. Background and Motivation

In 2012, of the 607,000 road bridges in the United States, 67,000 bridges were classified as structurally deficient and another 85,000 bridges were classified as functionally obsolete; combined, these numbers comprise 25% of the U.S. bridge total [1]. It was also noted in 2012 that the average age of the nation's bridges was 43 years and that a vast majority of those bridges were designed for 50-year service lives [2]. Most bridges are inspected only once every 24 months with the caveat that "structures with advanced deterioration or other conditions warranting close monitoring may be inspected more frequently" [3]. The poor state of many of the nation's bridges and the need for more frequent inspections of those in particularly bad shape have contributed to a great demand for structural monitoring that cannot be satisfied conventionally in a timely manner. This fact has led to a rising level of interest in remote structural monitoring. A 2001 report for the Minnesota Department of Transportation explicitly recommended that at-risk bridges should be actively monitored utilizing bridge health-sensing equipment to detect approaching failure [4].

Multiple options currently exist for structural health monitoring. Strategic placement of strain gauges [5], pattern recognition performed on acceleration data [6], and acoustic emissions monitoring [7] have all been noted in literature as viable methods for detecting structural deterioration. These method can all be implemented to function remotely. However, irrespective of choice of monitoring technique, its implementation will require electrical power to enable sensing and data transmission.

The most obvious method for procuring this power is by using existing power lines; however, wiring new power and communication lines to the sensors is time consuming and expensive [8]. In contrast, the

use of a wireless sensor network employing self-contained power facilitates deployment/installation and offers greater flexibility in the layout of the sensor nodes. The greater flexibility does not only serve to expand possible node placement to previously inaccessible locations, but it also simplifies changing the node layout should the need occur in the future, as cabling would not have to be considered [9].

Batteries are another overt candidate for providing power for structural monitoring. However, given the need to replace or recharge batteries periodically motivates a more maintenance-free solution, such as scavenging energy from the environment. Two common energy harvesting techniques are solar and wind power generation. These methods, however, are also imperfect for the given application. Low level power generation benefits from the generator and sensor being in close proximity to each other to limit cabling power losses. Given that solar and wind power generators need to be exposed to the respective elements from which they harvest energy, this limits available mounting options on a bridge. This is especially true for solar energy harvesting, as bridge sensors often need to be located in places with extremely low light intensities [5]. Additionally, the available power provided by solar and wind generators does not necessarily coincide with power demands for sensing. Conversely, since a bridge is mechanically excited during its customary use, an electromechanical harvester that harvests energy from the bridge's vibrations does not features this drawback. Conceptually, such a device needs little maintenance, decreases the length of necessary electrical leads to the sensing elements, and is guaranteed to generate power during periods when the bridge is exposed to frequent dynamic loading.

The three most prevalent forms of electromechanical harvesting are electrostatic, piezoelectric, and electromagnetic [10-18]. Electrostatic generation requires the incorporation of an external voltage source, making it a suboptimal choice for autonomous install-and-forget power generation [19]. Piezoelectric generators tend to have limited lifetimes, as their performance degrades with the persistent direct straining of the piezoelectric material [10], and these materials tend to have rather poor mechanical properties [19]. Due to these undesirable qualities associated with electrostatic and piezoelectric generation, and due to its relatively greater robustness and controllability [20], electromagnetic generation is a superior candidate for harvesting energy from bridge vibrations. Developing this type of electromechanical harvesting to serve as a method for delivering power to structural sensors for monitoring bridges was the chief motivation for this dissertational work.

3. Overview of Existing Research for Addressing Single Operational Frequency of Vibration Harvesters

Most conventional electromagnetic vibration energy harvesters are similar in behavior to a linear mass-spring-damper [9, 19]. Inherently, such devices are able to harvest significant power only when their excitation frequency is at, or very close to, the device's mechanical natural frequency [10, 15, 19, 21]. This limitation is problematic for the application in question for several reasons: (1) different bridges vibrate at

different frequencies [22]; (2) frequencies present in the vibration of a particular bridge will vary depending on traffic conditions [6]; and (3) a bridge will oscillate at several different frequencies simultaneously at any given mounting point for the harvester [22].

A significant amount of research has focused on addressing these issues associated with the single operating frequency of vibration energy harvesters. Most of the approaches existing in the literature can typically be grouped into one of two categories: (1) widening the power harvesting bandwidth of the generator by using an array of multiple harvesters with different natural frequencies; or (2) tuning the natural frequency of the generator to match the dominant frequency of the excitation [19].

Sari et al [23] and Ferrari et al [24] describe how an array comprised of multiple conventional cantilever beam generators having slightly different natural frequencies will result in a frequency bandwidth, as opposed to a single frequency, within which substantial energy capture occurs. Zhu et al [9] and Challa et al [16] experimentally investigate different approaches to alter the stiffness (and thereby the natural frequency) of a cantilever beam-type generator by using a linear motor to adjust the distance between a grounded magnet and another magnet on the cantilever. Peters et al [14] and Lallart et al [25] show that piezoelectric actuators could also be employed to alter a generator's effective stiffness for frequency tuning. These methods provide increased power generation at the cost of increased design complexity. The generator arrays require assembly of multiple non-interfering generators, while the tuning techniques typically require additional actuation to alter the harvester's equivalent mechanical stiffness. Alternative tuning methods aimed at avoiding the need for additional actuation were explored by Cammarano et al [15] and Bowden et al [26]. The proposed techniques still attempt to match the harvester's natural frequency to the dominant frequency of the excitation source, but the tuning is accomplished solely via an adjustable electrical load. Electrical tuning has become increasingly popular, and often is claimed to provide lucrative gains in terms of generated power. For example Renno et al [27] claims that by optimizing certain electrical components, "one can harvest maximum power everywhere in the frequency domain". However, since the researchers do not consider stability of the overall harvester dynamics, they do not realize that in fact it is impossible to ensure maximum power transfer to a load to exist in a certain frequency bandwidth. This fact is analytically confirmed using the introduced stability assessment technique and experimentally validated later in the present manuscript.

Other approaches to addressing the single operating frequency problem of vibration generators are listed in references [19] and [18], which provide a thorough review of the literature. Regardless of the approach taken, however, new tools for predicting performance are needed. The literature currently contains a gap for such tools, especially with regard to multifrequency excitation and active loads. This gap was directly alluded to by Beeby et al when he claimed that current power metrics are not "ideal" as they "…ignore important factors such as bandwidth," because "insufficient data exists in literature to enable this

(bandwidth considerations) to be included" [28]. It is precisely this gap, formed by the need for a better power metric, and the currently unrecognized need for stability evaluation in electrical load tuning, that is addressed by the research describe in this work.

4. Organization of Dissertational Work

The research described in this dissertational work details the development and application of analytical tools and control techniques to evaluate the performance of vibration energy harvesters for non-standard excitation (i.e., when the excitation is not comprised of a single, unvarying frequency). Specifically, the goal is to advance the understanding of how the interaction between the excitation source, the harvester's mechanical dynamics, and the harvester's electrical load affects stability and power generation. A thorough understanding of the interplay between these three components allows to quickly and easily predict the behavior of vibration energy harvesters, even when complex dynamics and multifrequency excitation are involved. Therefore the developed research tools can be used to guide a harvester's mechanical and electrical design and tuning to increase power generation from a given excitation source.

The present manuscript describes the derivation, development, experimental validation, and use of these analytical tools to provide insight into maximizing power generation. The manuscript is organized as follows.

Section II provides an overview of the derivation and development of the analytical tools for assessing a harvester's stability and power generation given its particular dynamics and the electrical load to which it delivers power. Section III offers a description of the harvester designed and constructed for experimental validation. The subsections of Section III describe the testing carried out on the developed analytical tools with the help of the constructed harvester. Section IV describes how the analytical tool developed for estimating harvester power generation can be used in optimization and tuning; the section also lists some conclusions drawn from the insight provided by this tool about vibration energy harvesting in general. Sections 0 and 0 contain an accepted and a submitted journal article, respectively, and Section 0 contains a publication planned to be submitted in the future. These sections contain more in-depth descriptions of the topics discussed in Sections II-IV, and can be referred to for additional information as needed. Section V provides a summary of the dissertational work's achievements and lists the technical contributions of the accepted, submitted, and planned publications. Lastly, Section 0 lists the literature referred to throughout the course of the research.

II. MODELING APPROACH AND DEVELOPMENT OF PHR AND STABILITY ASSESSMENT

As mentioned in the previous section, the central theoretical contribution of the presented research is the development of analytical tools that assess harvester stability and help estimate power generation when the harvester's excitation is comprised of multiple frequency components.

The power generation estimation tool ultimately yields a particular harvester's total expected average power generation. However, it has an additional advantage. Because power generation is presented as a function of frequency, the proposed technique allows to quickly quantify the amount of power being contributed by each individual frequency component. The method also helps understand the interplay that exists between the harvester's internal dynamics, its electrical load, and the excitation from which it generates power.

The stability assessment tool is a Nyquist stability criterion-based approach for evaluating whether a particular electrical load can be implemented with a certain harvester. More complicated, active electrical loading is beginning to be considered by researchers as a means to increase harvester power generation in cases when excitation does not consist of just a single, constant frequency. As this type of loading can potentially bring about unstable closed-loop behavior in the harvesting system, the stability assessment tool was derived to serve as a preliminary requirement for using a particular electrical load.

The development of these tools, as well as the associated implications, are detailed below. The derivations of both tools originate with the modeling approach presented in the following section.

1. Modeling Approach

The development of the electromagnetic vibration energy harvester model used in the presented research starts with the standard lumped-parameter approach frequently seen in literature and shown below in Figure 1.

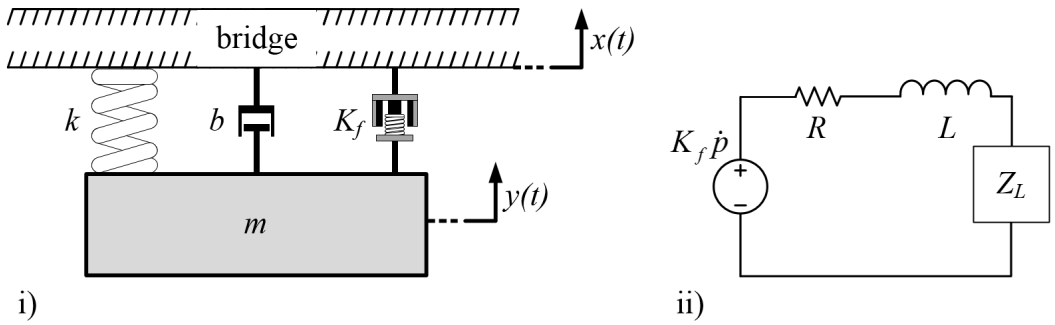

Figure 1: (i) Lumped parameter representation of a traditional vibration energy harvester (ii) Electrical components of a traditional vibration energy harvester

In the above figure, the harvester consists of a proof mass m connected to an excitation source (e.g., bridge) through a linear spring with stiffness coefficient k, and a linear damper with damping coefficient b. A linear electromagnetic motor with a torque/back EMF constant K_f is placed between the input excitation and the proof mass – in parallel with the damper and spring. Relative velocity between the proof mass (rigidly connected to the motor's coil) and the input excitation (rigidly connected to the motor's housing and magnetic core) generates a back EMF voltage in the motor coil. The coil's (electrical resistance R, electrical inductance L) two ends are attached to an electrical load (represented as a generalized electrical impedance Z_L). In this form, the harvester's electromechanical behavior is described by a system of two equations representing the coupled mechanical and electrical dynamics:

$$m\ddot{x} = m(\ddot{x} - \ddot{y}) + b(\dot{x} - \dot{y}) + k(x - y) + K_f i = m\ddot{p} + b\dot{p} + kp + K_f i \tag{1}$$

$$K_f \dot{p} = L\frac{di}{dt} + Ri + v_L \tag{2}$$

where x is the displacement associated with the excitation, y is the displacement associated with the proof mass, $p \stackrel{\text{def}}{=} x - y$ is the relative displacement between the excitation and the proof mass, i is the current flowing through the motor's coil, and v_L is the voltage across the electrical load.

This harvester model represented by equations (1) and (2) is ubiquitous in literature [26, 29]; in order to be more directly useful for the purpose of the present research, this canonical model is transformed into a form more conducive to power generation analysis.

Load matching is a key component in achieving efficient vibration energy harvesting. According to Stephen, "…the concept of load matching must be applied within the domain to which power is being delivered" [30]. Because in vibration energy harvesting power is transferred from the mechanical to the electrical domain, in order to analyze the effect of the electrical load on power generation, the harvester's dynamics described by (1) and (2) were cast entirely into the electrical domain. The Laplace transform was then used on this electrical domain equivalent of the harvester system in order to facilitate stability analysis as descried in Section 2 and to enable a novel approach to estimating power generation discussed in Section 3.

These transformations ultimately result in the vibration energy harvester dynamics defined by (1) and (2) being represented by the Thévenin equivalent circuit shown in Figure 2. In this representation, $V_{exo}(s)$ is an excitation-dependent exogenous voltage source, $Z_S(s)$ is the source impedance of the harvester (this source impedance encompasses both, the mechanical and electrical components), and $Z_L(s)$ is the impedance of the harvester's electrical load. The intermediate steps and assumptions involved in obtaining the below circuit representation of the harvester are listed on pages 37-39.

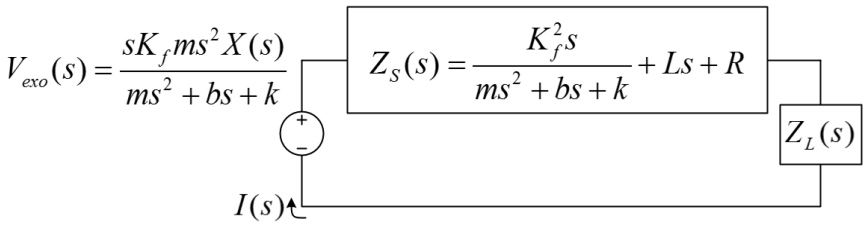

Figure 2: Thévenin equivalent circuit representation of the vibration energy harvester

This choice of using the Thévenin equivalent, s-domain circuit as the harvester model is not arbitrary. As previously mentioned, this modeling approach greatly facilitates stability analysis and power generation estimation; this will be explicitly demonstrated in the following two sections. An additional key benefit of this modeling approach, and the reason that $V_{exo}(s)$ is termed an *exogenous* voltage source, is that in this representation of the harvester, the displacement associated with the excitation source, not the relative displacement associated with the electromagnetic motor, affects the voltage source. This simplifies the problem by creating a perception of an ideal voltage source that is not affected by the choice of the harvester's electrical load, which in turn, simplifies the analysis of how the electrical load effects power generation. A similar "decoupling" modeling approach was pursed for the same reason by Kong et al [31].

2. Stability Considerations

The harvester model shown in Figure 2 allows the expression of system dynamics in transfer function form. This, in turn, enables the use of standard linear control theory techniques to directly assess the effect the electrical load impedance has on the overall stability and stability robustness of the harvester.

Consider the transfer function describing the relationship between the current flowing through the Thévenin equivalent circuit in Figure 2 and the exogenous voltage shown in (3)

$$\frac{I(s)}{V_{exo}(s)} = \frac{1}{Z_S(s) + Z_L(s)}. \tag{3}$$

This transfer function can be represented by the feedback system shown in Figure 3.

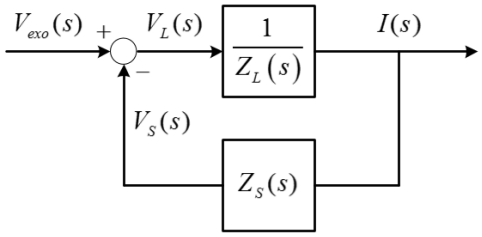

Figure 3: Feedback system with closed-loop dynamics equivalent to dynamics of the harvester

According to fundamental linear control theory, the "closed-loop" stability of the above-depicted system can be analyzed using the open-loop transfer function shown in (4)

$$G_{OL}(s) = \frac{Z_s(s)}{Z_L(s)}. \tag{4}$$

The first observation that should be made about this open-loop transfer function is that $Z_S(s)$, as it is defined in Figure 2, is a passive system which does not contribute any unstable poles to $G_{OL}(s)$. This implies that any and all unstable "open-loop" poles are produced by nonminimum-phase zeros of $Z_L(s)$. This fact can be used in conjunction with the Nyquist Stability Criterion to impose certain conditions on the choice of the electrical load to guarantee harvester stability. These conditions depend on the number of nonminimum-phase zeros in $Z_L(s)$.

If there are no nonminimum-phase zeros in $Z_L(s)$, (5) provides the necessary and sufficient condition to ensure overall harvester stability

$$-180° \leq \measuredangle G_{OL}(s) \leq 180°. \tag{5}$$

Because, as already mentioned, $Z_S(s)$ is passive, any passive load impedance $Z_L(s)$ will result in the above condition being satisfied (i.e., any passive load will produce stable harvester dynamics). Alternatively, when the load is active, (4) and (5) can be used as a selection prerequisite for $Z_L(s)$ that should be satisfied to ensure stable harvester dynamics. Additionally, if active electronics are involved, the encirclement criterion can enable the calculation of stability margins to assess stability robustness.

Conversely, if $Z_L(s)$ has nonminimum-phase zeros, it will contribute unstable open-loop poles to $G_{OL}(s)$. In this case, the Nyquist Stability Criterion stipulates that the plot of the Nyquist contour of $G_{OL}(s)$ must have as many counterclockwise encirclements of the critical point $(-1 + j \cdot 0)$ as there are nonminimum-phase zeros in $Z_L(s)$. Unfortunately, in this case, the Nyquist Stability Criterion cannot be used to arrive at clearly defined criteria for $Z_L(s)$ to ensure overall system stability. However, it can be shown that if the phase of $Z_L(s)$ satisfies (6)

$$-90° \leq \measuredangle Z_L(s) \leq 90° \tag{6}$$

for all $s = j\omega$, the Nyquist plot of $G_{OL}(s)$ will not have any encirclements. If this is the case and $Z_L(s)$ possesses one or more nonminimum-phase zeros, the harvester dynamics are guaranteed to be unstable. A noteworthy example of such a $Z_L(s)$ is a control law which attempts to enforce the maximum power transfer theorem (MPTT) dictated electrical load at all frequencies. This example, including the proof of it causing

unstable harvester behavior can be found in Section 0-6.1.1 on p. 68. Validation of the predicted unstable behavior can be found on pp. 76-77.

3. A Multifrequency Power Generation Metric – Power Harvesting Ratio

In addition to facilitating the stability analysis given the impedance of a particular electrical load, the modeling approach presented in Section II-1 serves as the basis for the derivation of a power generation technique. This linear technique provides an estimate of the average power generated by a harvester given the harvester's internal dynamics, the excitation to which it is exposed (note that the excitation can be comprised of multiple frequency components), and the impedance of its electrical load.

3.1. Derivation

This power generation estimation technique is developed under three assumptions: (1) the excitation consists of steady-state oscillations, (2) the harvester and its electrical load behave linearly and (3) the harvester's dynamics are confirmed as stable in accordance with the preceding Stability Considerations section. If these assumptions are met, the equation for average power absorbed by an impedance in an alternating current circuit shown below can be used:

$$\overline{\mathbb{P}} = \frac{1}{2}|V||I|\cos(\varphi), \tag{7}$$

where $\overline{\mathbb{P}}$ is the average power absorbed by the load impedance, $|V|$ is the amplitude of the sinusoidal voltage across this impedance, $|I|$ is the amplitude of the current running through this impedance and φ is the phase between V and I. Applying (7) and the listed assumptions to the Thévenin equivalent circuit representing the harvester shown in Figure 2 results in the expression for $\overline{\mathbb{P}}(\omega)$, the average power absorbed by the harvester's electrical load at a particular frequency ω, shown in (8):

$$\overline{\mathbb{P}}(\omega) = \frac{1}{2}|V_L(s)||I(s)|\cos\left(\measuredangle Z_L(s)\right)\Big|_{s=j\omega}. \tag{8}$$

By dividing both $|V_L(s)|$ and $|I(s)|$ by the amplitude of the exogenous voltage $|V_{exo}(s)|$, the relationship between the average power absorbed by the load and the "input voltage" into the system is obtained as shown in (9):

$$\frac{\overline{\mathbb{P}}(\omega)}{|V_{exo}(s)|^2}\Big|_{s=j\omega} = \frac{1}{2}\left|\frac{V_L(s)}{V_{exo}(s)}\right|\left|\frac{I(s)}{V_{exo}(s)}\right|\cos(\measuredangle Z_L(s))\Big|_{s=j\omega}. \tag{9}$$

Using the definition for $V_{exo}(s)$ from Figure 2, noting that under the assumption of a linear electrical load $V_L(s) = Z_L(s) \cdot I(s)$, and using the transfer function which describes the relationship between the current flowing through the Thévenin equivalent circuit and the exogenous voltage shown in (3), allows (9) to be transformed into (10), and subsequently (11):

$$\left.\frac{\overline{\mathbb{P}}(\omega)}{\left|\frac{K_f ms}{ms^2+bs+k}s^2X(s)\right|^2}\right|_{s=j\omega} = \frac{1}{2}\left|\frac{Z_L(s)}{Z_S(s)+Z_L(s)}\right|\left|\frac{1}{Z_S(s)+Z_L(s)}\right|\left.\cos(\measuredangle Z_L(s))\right|_{s=j\omega}, \tag{10}$$

$$\left.\frac{\overline{\mathbb{P}}(\omega)}{|s^2X(s)|^2}\right|_{s=j\omega} = \frac{1}{2}\left|\frac{Z_L(s)}{|Z_S(s)+Z_L(s)|^2}\right|\left|\frac{K_f ms}{ms^2+bs+k}\right|^2\left.\cos\big(\measuredangle Z_L(s)\big)\right|_{s=j\omega}. \tag{11}$$

Equation (11) defines the mathematical relationship between the acceleration of the excitation squared and the average power generated by the harvester at a particular frequency. This relationship, designated as the "power harvesting ratio" (PHR), is the sought-after multifrequency power generation metric; it is a principal contribution of this dissertational work and will be heavily utilized throughout the rest of the manuscript.

The form of the PHR, as it is shown in (11), was not arbitrarily chosen. The normalization with respect to excitation facilitates the calculation of the amount of power harvested from each frequency component; this is accomplished by simply multiplying (11) by the frequency spectrum of the excitation's acceleration amplitude squared. Acceleration is used in favor of displacement in order to portray a harvester's ability to generate power at different frequencies in an intuitively understandable way. Explicitly, if the excitation's acceleration is kept constant, $m\ddot{x}$, the quantity which may be interpreted as the exogenous physical input into the system shown in (1), stays constant as well. If, given this constraint, (11) is plotted versus excitation frequency, than if the resulting curve has a larger amplitude at frequency ω_1 than at frequency ω_2, the necessary implication is that the harvester operates more efficiently at ω_1 than it does at ω_2, since the harvester had an equal magnitude of input at both frequencies. However, if the normalization was performed with respect to displacement, $m\ddot{x}$ would grow in magnitude with frequency. The resulting curve would increase in amplitude at much higher frequencies, not due efficient operation, but due to the much larger magnitude of available input. An example of a plot of this type of curve can be seen in Figure 2 of [6]. This type of graphical portrayal of power generation may lead to an erroneous assumption that a given harvester's power generation increases monotonically with frequency.

To validate the claim that PHR can be used to accurately estimate a harvester's average power generation, the experimentation detailed in the following section was carried out.

III. EXPERIMENTAL VALIDATION

The setup used for experimental validation is shown in Figure 4 below.

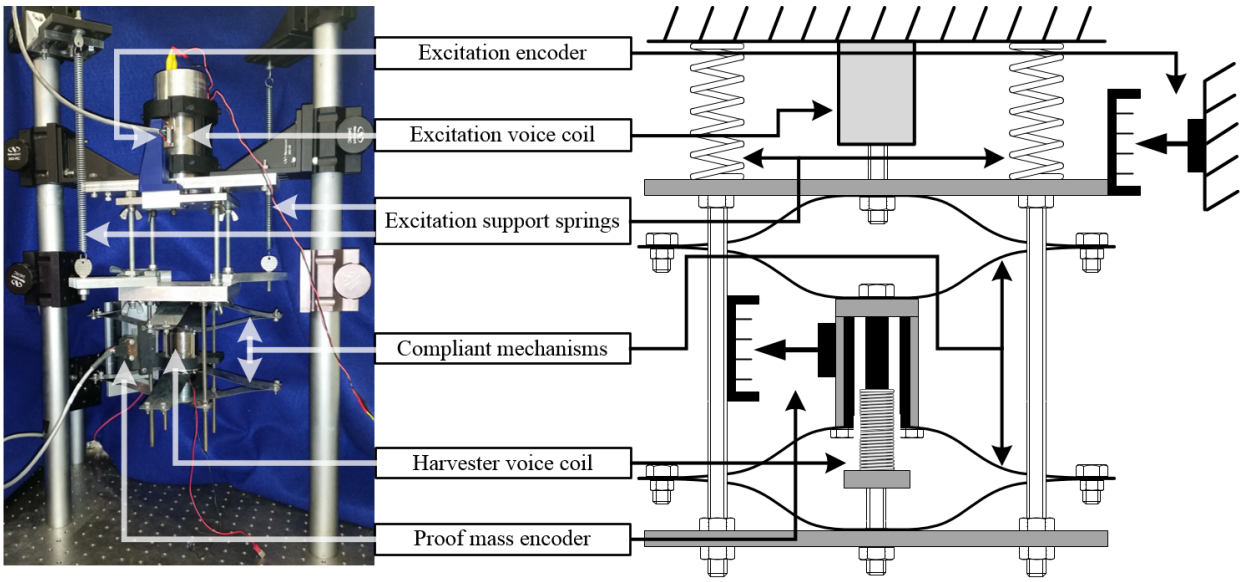

Figure 4: Photograph and schematic of experimental electromagnetic vibration energy harvester

The design incorporates compliant mechanisms which, not only serve as the elastic spring elements of the mass-spring-damper vibration energy harvester, but also minimize parasitic losses from friction by enforcing good alignment between the housing and coil of the linear motor responsible for energy harvesting. The linear motor's (BEI linear voice coil LA17-28-000A) housing is suspended by these compliant mechanisms, allowing it to move only along the intended axis without coming into contact with the motor's coil. The coil itself is rigidly attached to the excitation source. This accomplishes the alignment of the harvester's proof mass without the use of bearing surfaces, which tend to increase parasitic losses. In this configuration, the housing of the linear voice coil serves as a proof mass, the relative motion of which results in power generation.

In their design, the compliant mechanisms were approximated as beams that are cantilevered at one end and constrained to translate in the vertical direction at the other; this allowed their equivalent stiffness to be estimated using well-established cantilevered beam equations [32]. The width, length, and thickness of the compliant mechanisms were chosen to achieve a stiffness such that the harvester would have a natural frequency of 7.8 Hz, which is close to the middle of the frequency range of interest. This range of interest was chosen by noting that bridges' dominant modes of oscillation are typically in the range of 3-12 Hz [5, 6, 33, 34].

A larger voice coil (BEI linear voice coil LAH28-52-000A) was used as the mechanical excitation source for the harvester. It was powered using a Kepco BOP 36-6 servo amplifier. The displacement produced by

this linear voice coil and the displacement of the harvester's proof mass were measured using two optical encoders (U.S. Digital optical encoder modules EM1 used in conjunction with 500 counts/inch linear strips and x4 quadrature to produce 2000 count/inch resolution). The excitation encoder was used for closed-loop control of the excitation voice coil. Good alignment between this encoder and its linear strip was enforced by coupling the harvester and the excitation voice coil using a linear bearing which cannot be seen in the photograph shown in Figure 4 as it is behind the harvester. Two extension springs were used to help support the weight of the harvester, reducing the static load on the excitation voice coil, thereby allowing it to produce higher dynamic excitation forces. The voltage across the harvester's load was measured with a DAQ card and the current flowing through the harvester leads was measured using an inductive current probe (Agilent 1146A). MathWorks MATLAB and Simulink Real-time R2014a were used in conjunction with National Instruments PCI-6259 DAQ card for control of the experimental setup and for data acquisition.

The parameters governing the harvester dynamics (with the notable exception of the electrical load) needed to calculate the PHR are listed in Table 1. The harvester's linear voice coil's motor constant K_f, and inductance L, were taken directly from its data sheet. The motor's resistance R was measured. The built-in Simulink Model Parameter Estimation routine was used to determine the magnitudes of the proof mass m, the equivalent stiffness k, and the mechanical damping parameter b.

Table 1: Experimental harvester parameters

Parameter	Value
m	0.697 kg
b	6.925 N/(m/s)
k	1665 N/m
K_f	17.8 N/A or V/(m/s)
L	0.0031 H
R	7 Ω

1. Validating PHR for Single Frequency Component Excitation

This section presents a fundamental level validation of PHR carried out; the goal of the presented testing was to assess whether the PHR equation introduced in (11) is capable of predicting harvester power generation given that the excitation is comprised of only a single frequency. In the testing described in this section, the electrical load was restricted to passive components and chosen according to MPTT implemented at the natural frequency of the harvester. The calculations used for solving for the necessary load impedance, and the quantitative justification for discarding the capacitive component of this load impedance can be found on page 46 in Appendix A. Ultimately, the load which was used was a resistance of 52.7 Ω (i.e., $Z_L(s) = Z_L = 52.7\ \Omega$).

Figure 5 shows the power harvesting ratio curve calculated using (11) and the experimentally measured values of the power harvesting ratio on the same plot. The experimental values were obtained by subjecting the harvester to excitation 1 mm in amplitude at distinct, individual frequencies in the 3-12 Hz range. Each excitation frequency was run for 60 cycles, during which the instantaneous voltage that developed across the 52.7 Ω load resistance was measured and recorded; this voltage was used to calculate the average power the harvester delivered to the load (i.e., power dissipated across the load resistance) according to:

$$\overline{\mathbb{P}}_{exp}(\omega) = \frac{\left(\overline{v_L}(\omega)\right)^2}{R_L} \tag{12}$$

where $\overline{\mathbb{P}}_{exp}(\omega)$ is the experimentally measured average power generated at frequency ω, $\overline{v_L}(\omega)$ is the value of the instantaneous load voltage averaged over 60 cycles at ω, and R_L is the load resistance of 52.7 Ω. In order to make it directly comparable to PHR, the average power generated at each frequency of excitation was normalized with respect to the excitation's acceleration amplitude squared. This amplitude was determined by taking the discrete Fourier transform (DFT) of the excitation's measured displacement to determine the experimental average amplitude of the displacement (instead of assuming it was exactly 1 mm as was commanded to the excitation voice coil) and its frequency. The amplitude and frequency of the displacement were then used to calculate the amplitude of acceleration by assuming purely sinusoidal motion.

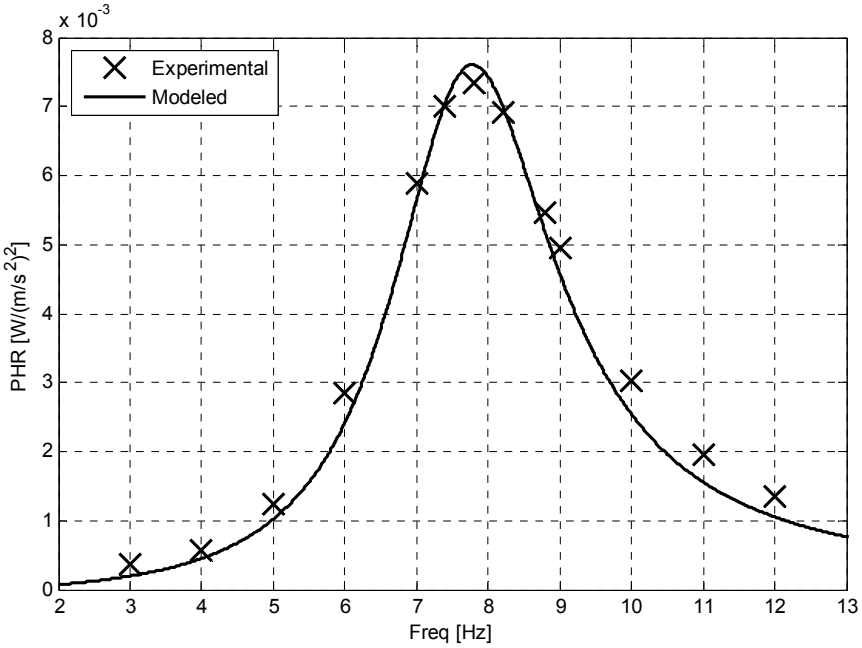

Figure 5: Modeled and experimental power harvesting ratio for single-frequency excitation for $Z_L = 52.7\ \Omega$

As additional support for PHR being able to accurately estimate average power generation, consider (13) derived by Stephen (equation (55) in [35]) which solves for the average power delivered to a conventionally tuned electrical load (i.e., purely resistive load chosen according to MPTT as dictated by (36) on p. 46) by a harvester operating at its mechanical natural frequency.

$$\overline{\mathbb{P}}(\omega_n) = \frac{K_f^2 m^2 \omega_n^4 Y^2}{8b\left(bR + K_f^2\right)} \tag{13}$$

The variables used by Stephen were replaced in (13) by those representing the same physical quantities according to the present manuscript's convention. The only variable that has not been defined is Y, which represents the amplitude of the excitation's displacement.

If (13) is normalized with respect to the excitation's acceleration amplitude squared (i.e., divided by $Y^2\omega_n^4$) to make the expression equivalent to PHR defined by (11), and the values from Table 1 are substituted in, the resulting quantity is 7.6 mW/(m/s^2)^2. Equation (11) yields the identical value at $s = j\omega_n$, while the experimentally measured value at the natural frequency is 7.4 mW/(m/s^2)^2, which translates to -3 % experimental error.

2. Validating PHR for Excitation Comprised of Multiple Frequency Components

This section presents the more advanced validation of PHR; the goal of the presented testing was to assess whether PHR is capable of predicting harvester power generation given different excitations comprised of multiple frequency components and different electrical loads.

As an example demonstrating how PHR is used for more complex excitation that that which was shown in the previous section, consider excitation having four frequency components: ω_n, $1.5\omega_n$, $2\omega_n$, and $2.5\omega_n$. The amplitudes of these components were chosen to be similar to real-world bridge span vibrations shown in [22], with components having higher frequencies being assigned lower acceleration amplitudes. Figure 6 shows the spectrum of the squared amplitude of the acceleration of the harvester's excitation (i.e., DFT with squared acceleration amplitude on the y-axis), with units indicated on the right-hand y-axis. This figured also contains the harvester's PHR curve calculated from (11), its units are placed on the left-hand y-axis. The depicted curve is identical to the PHR curve shown in Figure 5, as the harvester's electrical load was unchanged from that used in the single frequency testing described in the previous section (i.e., $Z_L = R + K_f^2/b = 52.7\ \Omega$).

Figure 7 shows the harvester's predicted average power generation as a function of frequency; it was obtained directly from the data plotted in Figure 6. Explicitly, the prediction for the average power

generated by the harvester at each frequency is calculated by multiplying the squared acceleration amplitude data by the corresponding PHR value at each frequency according to (14):

$$\overline{\mathbb{P}}(\omega_i) = a^2(\omega_i)\cdot \mathrm{PHR}(\omega_i), \tag{14}$$

where ω_i is a particular frequency expressed in the DFT data, and $\overline{\mathbb{P}}(\omega_i)$, $a^2(\omega_i)$, and $\mathrm{PHR}(\omega_i)$ are the average generated power, the squared magnitude of the excitation's acceleration, and the power harvesting ratio value at that frequency, respectively. Equation (14) essentially shows how the equation defining PHR shown in (11) is practically implemented.

In order to arrive at the prediction for the total average power generated by the harvester for a given excitation $\overline{\mathbb{P}}_{tot}$, (14) is calculated at each frequency in the acceleration amplitude spectrum of the excitation, and the resulting values are summed together as shown in (15):

$$\overline{\mathbb{P}}_{tot} = \sum_{i=1}^{N} \overline{\mathbb{P}}(\omega_i), \tag{15}$$

where N is the number of frequencies represented in the DFT of the excitation.

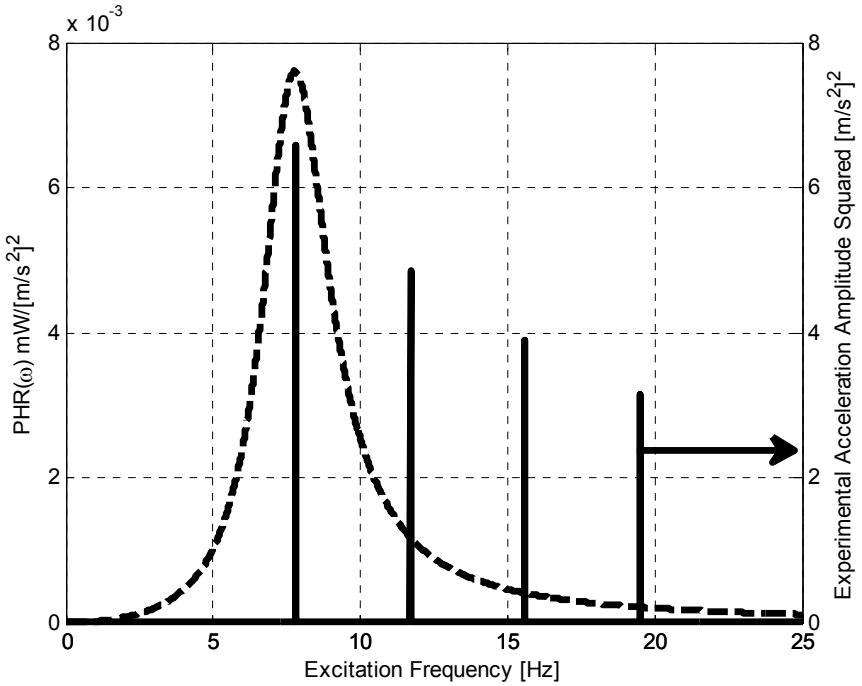

Figure 6: Spectrum of the squared amplitude of the acceleration of the harvester's excitation and calculated power harvesting ratio (for $Z_L = 52.7\ \Omega$). Arrow used to indicate corresponding axis.

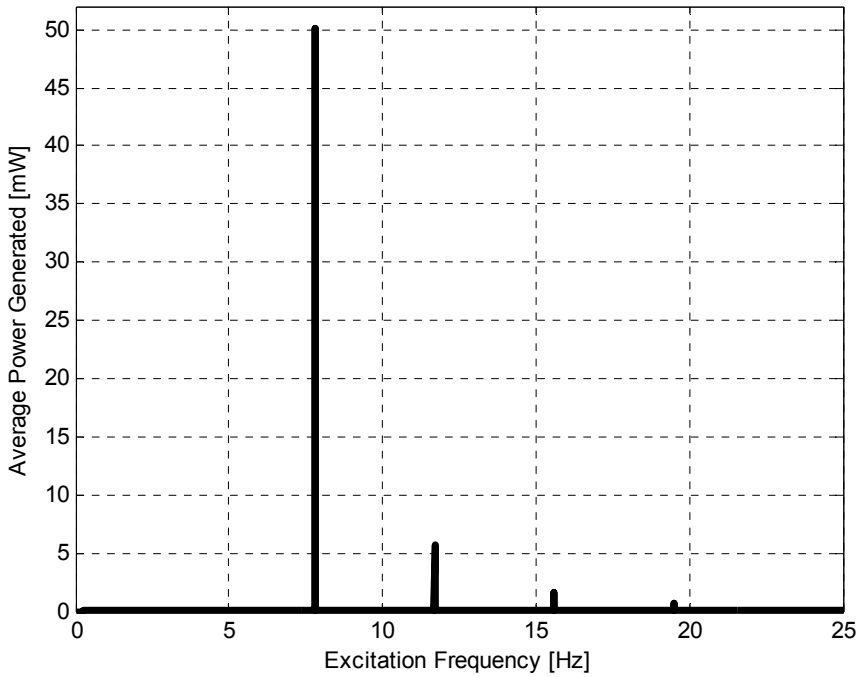

Figure 7: Predicted average power generation as a function of frequency

Figure 7 illustrates a unique advantage of using PHR as a tool for predicting a harvester's power generation. The power harvesting ratio takes into account power generated from all frequency components comprising the excitation, thereby trying maximizing the accuracy of the estimate of the harvester's total power generation. Arguably more important, however, is that Figure 7 provides a quick and easy way to quantify the contribution of each individual frequency component to this overall power generation; this quality makes it a useful and intuitive tool to use in cases where the harvester is generating power from multifrequency excitation.

Convenience of use alone cannot justify the use of PHR; to assess PHR's accuracy, the components shown in Figure 7 were summed and the resulting quantity was compared to the experimentally determined average power generation. The results for this test, as well as results of other tests which varied the multifrequency component excitation and employed different electrical loads are shown in Table 2. Note that in the table the model average power generated indicates the power generation predicted by PHR.

Table 2: Modeled and experimental harvester power generation values for multifrequency input excitations and various load impedances

Test #	Primary Excit. Frequencies [Hz]	Corresponding Accel. Amplitudes [m/s^2]	Load Resistance [Ω]	Load Capacitance [μF]	Model Avg. Pow. Gen. [mW]	Experimental Avg. Pow. Gen. [mW]	Modeling Error [%]
1	7.8, 11.7, 15.6, 19.5	2.57, 2.20, 1.97, 1.77	52.7	0	58.9	58.1	1.4
2	7.8, 11.7, 15.6, 19.5	2.57, 2.20, 1.97, 1.77	52.7	0	58.8	58.0	1.4
3	7.8, 11.7, 15.6, 19.5	2.57, 2.19, 1.96, 1.76	100	0	50.4	51.3	-1.8
4	7.8, 11.7, 15.6, 19.5	2.57, 2.19, 1.96, 1.76	100	0	50.6	51.6	-1.9
5	7.8, 11.7, 15.6, 19.5	2.57, 2.22, 1.96, 1.76	19.7	0	53.7	51.6	4.1
6	7.8, 11.7, 15.6, 19.5	2.57, 2.22, 1.98, 1.77	19.7	0	54.0	51.9	4.0
7	6.5, 7.8, 9.3	1.76, 2.55, 1.83	52.7	0	74.7	73.8	1.2
8	6.5, 7.8, 9.3	1.76, 2.56, 1.84	52.7	0	75.0	74.2	1.1
9	6.5, 7.8, 9.3	1.77, 2.55, 1.83	100	0	62.8	63.0	-0.4
10	6.5, 7.8, 9.3	1.76, 2.55, 1.82	100	0	62.6	62.8	-0.4
11	6.5, 7.8, 9.3	1.76, 2.56, 1.86	20.3	0	68.5	63.2	8.4
12	6.5, 7.8, 9.3	1.76, 2.56, 1.86	20.3	0	68.5	63.3	8.3
13	6.5, 7.8, 9.3	1.77, 2.51, 1.83	20.3	280	26.6	24.4	9.2
14	6.5, 7.8, 9.3	1.77, 2.51, 1.83	20.3	280	26.6	24.5	8.7
15	6.5, 7.8, 9.3	1.77, 2.53, 1.83	52.7	280	45.5	41.2	10.4
16	6.5, 7.8, 9.3	1.77, 2.52, 1.82	52.7	280	45.3	41.2	10.0
17	6.5, 7.8, 9.3	1.77, 2.53, 1.82	100	280	48.9	47.1	3.8
18	6.5, 7.8, 9.3	1.77, 2.53, 1.82	100	280	48.9	47.0	4.0

The experimental average power generated in Table 2 was calculated using (12), where R_L was given the value of the load resistance of the particular experimental load used, and $\overline{v_L}$ was the average value of the measured instantaneous voltage across this load resistance calculated over each two minute test run.

Note that each of the electrical loads used in tests #13 through #18 included a capacitive element. These tests were included to assess the accuracy of PHR for cases in which the electrical loading was not purely resistive, but featured a reactive component as well. For these cases, the expected power generation was calculated simply by setting $Z_L(s)$ in (11) to:

$$Z_L(s) = R_L + \frac{1}{C_L \cdot s} \tag{16}$$

where C_L was the value of the load capacitance.

Test #1 in the table is the particular experiment associated with the data shown in Figure 6 and Figure 7; it shows very close agreement with the experimentally calculated generated power (error = 1.4 %). In fact, all of results listed in Table 2 show PHR to be relatively accurate. Two thirds of the tests indicated that

PHR can estimate average power generation within 5 % of the experimentally measured values, with another one third being within approximately 10 %. This data provided further support for the hypothesis that the power harvesting ratio could be used to accurately predict a harvester's average power generation in cases when excitation is comprised of multiple different frequency components.

3. Validation Using Real-world Bridge Vibration Data

After developing the analytical tool for harvester stability assessment and deriving and performing rudimentary validation on the PHR technique for estimating a harvester's power generation, the next logical step was to test the practicality of these tools. Explicitly, as these tools were designed to be used for improving vibration energy harvesting from bridges, they first required validation using actual bridge vibration data. Thus, the final experimental validation step is the following demonstration of the effectiveness of these tools using real vibration data collected from bridges.

First samples of such data were collected from the Bob Sheehan Memorial Bridge in Nashville, Tennessee (36°11'10.8"N 86°38'00.8"W) shown on the left in Figure 8. This bridge was formerly open to traffic, but is now part of the Stones River Greenway trail system. This bridge provided a unique opportunity to collect both the free response (via impact testing) and forced response (via vehicle excitation) data in a completely controllable fashion. The free response was collected by using three accelerometers to record the bridge's vibratory response to impacts from a modal sledge distributed over twenty-one impact points spanning the bridge (shown on the right in Figure 8). The purpose of collecting free response data was to determine the bridge's primary modes. The first nine modes, as well as rough depictions of their shapes, are shown in Figure 9.

In order to assure that the above nine frequencies do in fact constitute different bridge modes, the modal assurance criterion (MAC) [36] was used to assess their linear independence from each other.

The criterion is essentially a method for gauging linear independence between vibration modes. Figure 10 shows a plot of the MAC values for fourteen possible modes, with mode numbers 1-9 designating the nine modes shown in Figure 9. Values close to one indicate that the modes are linearly dependent. This plot indicates that the nine modes identified in Figure 9 show a high degree of linear independence. Modes represented by numbers above 9 in the figure either did not possess the same degree of linear independence (10-14) or were too small in amplitude to be significant. This method for determining the bridge's primary modes was used to confirm that the forced excitation response of the bridge contained significant frequency components coinciding with frequencies determined to be modes of the bridge.

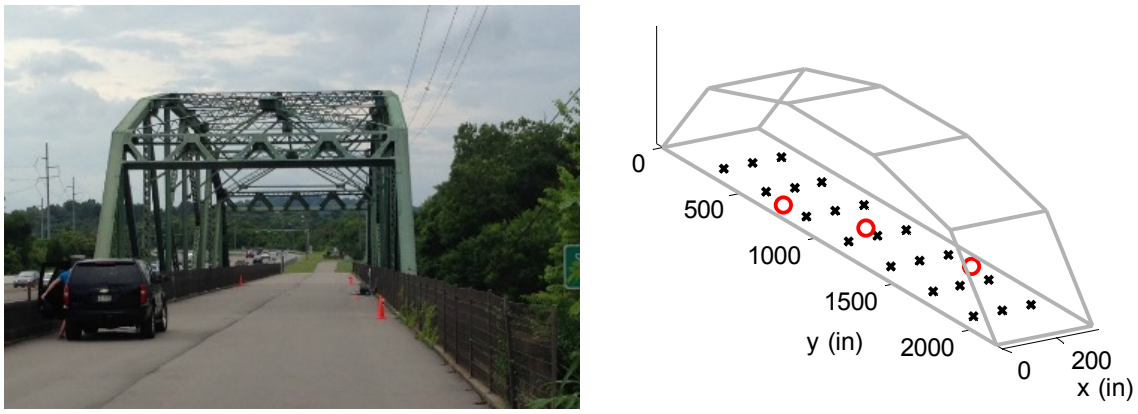

Figure 8: (A) Bridge used for experimental testing; (B) Schematic indicating impact points (**x**) and sensor locations (**o**) used during impact testing.

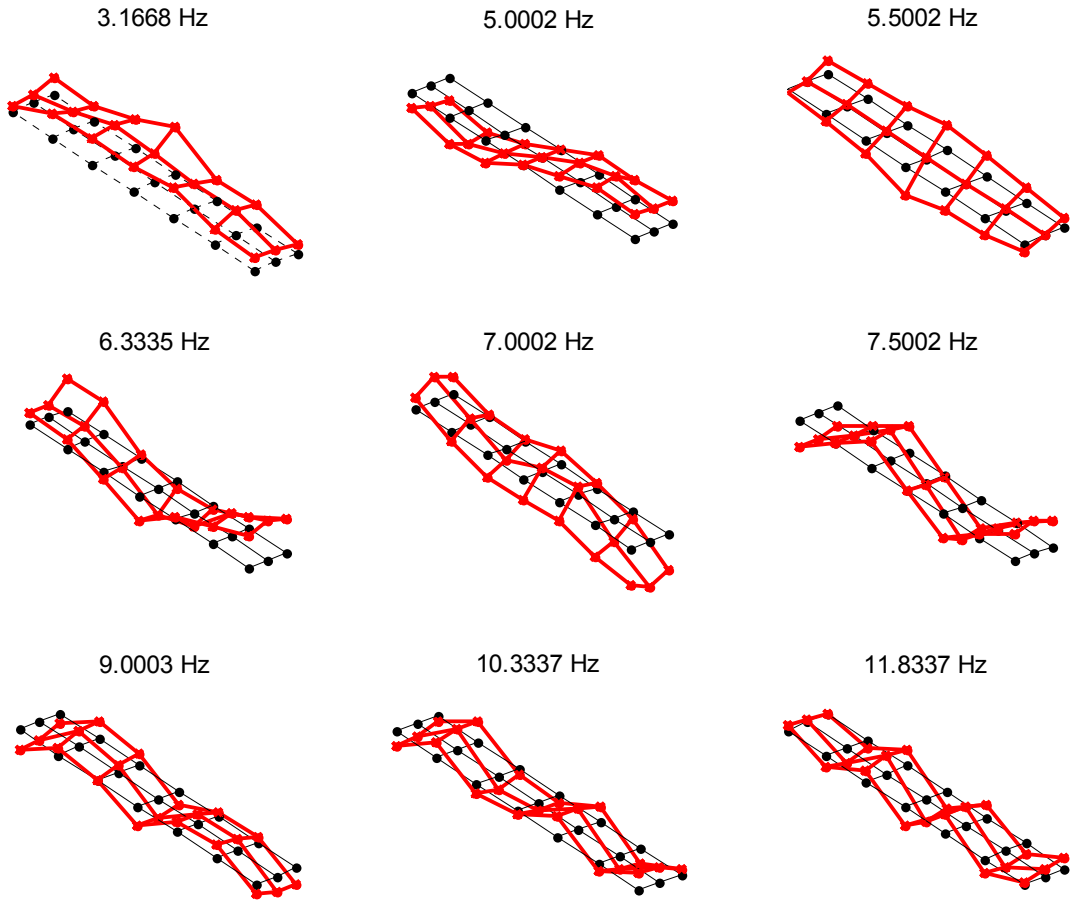

Figure 9: The first nine modes and their respective shapes of the Bob Sheehan Memorial Bridge

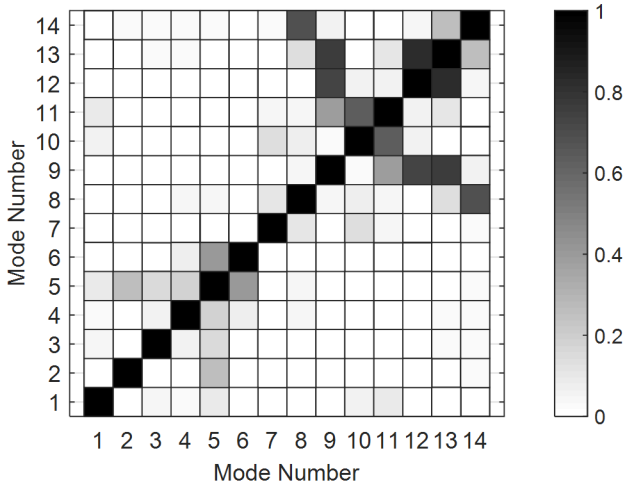

Figure 10: Modal assurance criterion values indicating the linear independence of the modes.

To obtain the bridge's forced response, a 2007 Chevrolet Tahoe (total weight including passengers ≈ 5900 lbs (2680 kg)) was driven across the bridge at a near constant speed of 20 miles per hour (32.2 kph). The response of the bridge was measured using the accelerometer located at the bridge's midpoint. Figures 11 and 12 show two collected time histories of the acceleration data that are representative of the collected data sets; the figures also show the respective DFTs of the data sets. Note that the peaks in the DFTs are either at, or very close to the determined primary modes of the bridge.

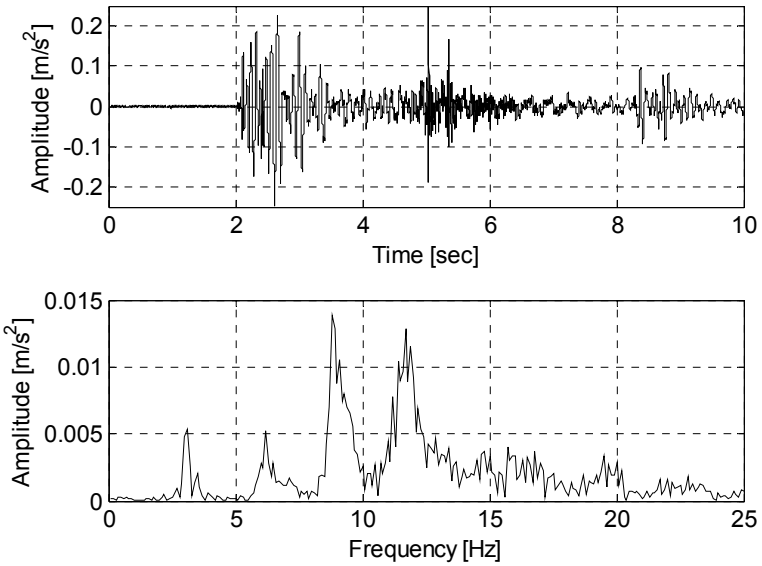

Figure 11: Bridge acceleration time series data set A (top) and its DFT (bottom)

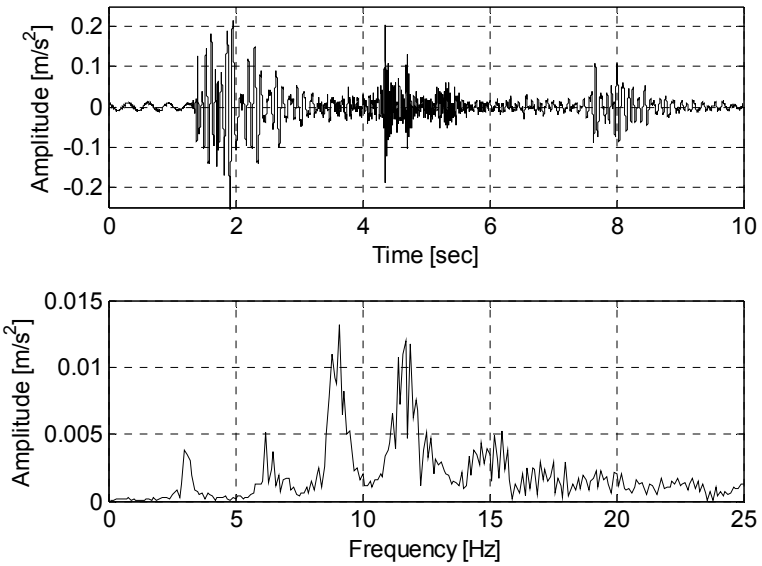

Figure 12: Bridge acceleration time series data set B (top) and its DFT (bottom)

Data sets A and B were used as excitation for the experimental harvester described at the beginning of Section III to test both, the stability assessment method based on the Nyquist Stability Criterion and the PHR power estimation technique. The testing procedure was analogous to that used for multifrequency excitation testing discussed in Section 2 on p. 14. The sole two differences were the excitation which was used and the selection of loads to be tested.

Using the procedure described in the Stability Considerations section on p. 7, when the above load is substituted as $Z_L(s)$ into (4), the resulting transfer function has three unstable open loop poles. The Nyquist plot of (4) shown on p. 69 does not encircle the critical point $(-1 + 0 \cdot j)$, thereby predicting the existence of three unstable loop poles in the harvester's equivalent closed-loop transfer function (3). This prediction of unstable behavior using the stability assessment method was confirmed when a servo amplifier was used to attempt to enforce the behavior required by (17).

Table 3 displays the loads that were tested using the physical bridge data collected off of the Bob Sheehan Memorial Bridge as excitation.

Note from the table that active loads were included at this stage of experimental validation. MPTT represent the active load prescribed by the maximum power transfer theorem. According to this theorem, the maximum amount of power is transferred from a power source to a load when that load's impedance is equal to the complex conjugate of the source impedance. Given the harvester's source impedance shown in Figure 2 on p. 7, the load which satisfies MPTT is given by (17)

$$Z_{MPTT}(s) = Z_S^*(s) = -\frac{K_f^2 s}{ms^2 - bs + k} - Ls + R. \tag{17}$$

Using the procedure described in the Stability Considerations section on p. 7, when the above load is substituted as $Z_L(s)$ into (4), the resulting transfer function has three unstable open loop poles. The Nyquist plot of (4) shown on p. 69 does not encircle the critical point $(-1 + 0 \cdot j)$, thereby predicting the existence of three unstable loop poles in the harvester's equivalent closed-loop transfer function (3). This prediction of unstable behavior using the stability assessment method was confirmed when a servo amplifier was used to attempt to enforce the behavior required by (17).

Table 3: Electrical Loads Used During Experimentation

Load Type	Load
Passive, resistive	52.7 Ω
Passive, resistive	23.6 Ω
Passive, resistive and capacitive	52.7 Ω and 240 μF
Passive, resistive and capacitive	23.6 Ω and 240 μF
Active	MPTT
Active	ACTIVE

The theoretical and experimental load voltage responses for when the harvester was being excited by the experimental version of bridge acceleration time series data set A (from Figure 11) is shown in Figure 13. A detailed step-by-step explanation of how the stability assessment was carried out to predict that $Z_{MPTT}(s)$ would cause the harvester dynamics to become unstable, while $Z_{ACTIVE}(s)$, shown in (18)

$$Z_{ACTIVE}(s) = \frac{s(s+60)^2}{20(ms^2 + bs + k)}. \tag{18}$$

would not do so can be found in Section 6.1 on pp. 68-71.

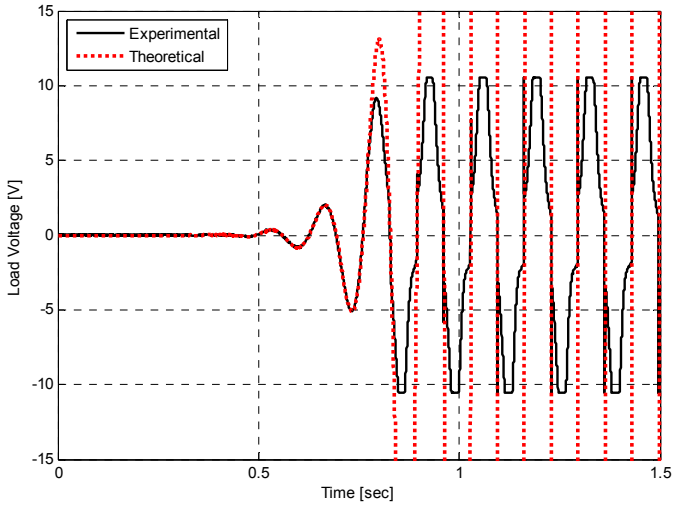

Figure 13: Load voltage response to excitation when $Z_L(s)$ is chosen according to MPTT

In addition to validating the stability assessment tool, the time series data sets shown in Figures 11 and 12 were also used to test the accuracy of PHR in estimating power generation for excitation representative of realistic bridge vibrations

Figure 14 depicts the PHR-predicted average power generation values plotted against their resultant error quantities for all of the experimental runs the excitation of which was based on the acceleration time series data set A from Figure 11. Figure 15 plots the corresponding results for experimental runs that used excitation based on the acceleration time series data set B from Figure 12

A more thorough explanation of these results and the experimental conditions/procedure for obtaining them can be found in Section 7 on p. 74. The key observation that should be made from Figures 14 and 15 presently is that the magnitude of the displayed error values is small. According these figures, the maximum difference between the PHR-predicted average power generation and that which was experimentally obtained while using realistic bridge data never exceeded 6 % for any of the tested loads, including $Z_{ACTIVE}(s)$.

The small error values achieved from testing all loads and using physical bridge data lent more credibility to the practical usefulness of the PHR method. However, despite the fact that the data used for experimental excitation was obtained from an actual bridge, it was considered an imperfect representation of the type of vibratory behavior a bridge would exhibit during typical use. The controlled nature of the excitation via the use of a single vehicle traveling at a predetermined speed was great from an experimental repeatability standpoint, but could hardly be claimed as the most usual type of excitation bridges are usually exposed to.

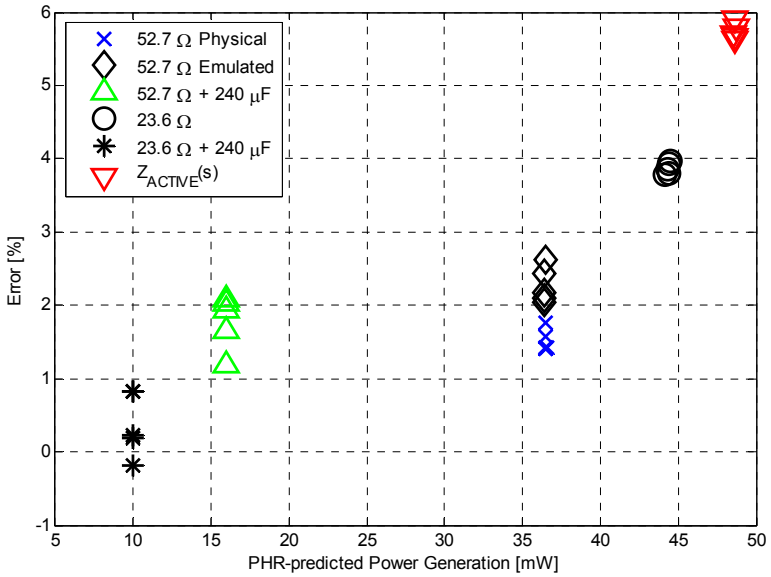

Figure 14: Average power generation predicted by PHR and its percentage difference from experimentally measured power generation for excitation based on data set A

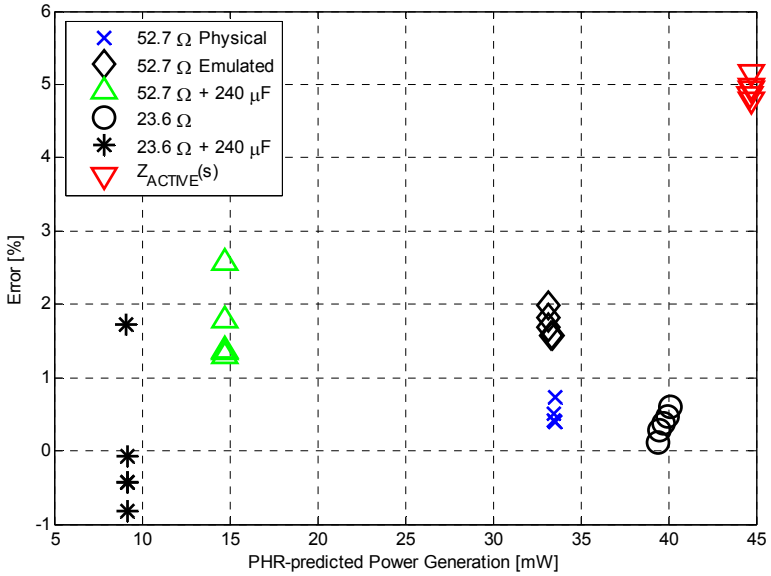

Figure 15: Average power generation predicted by PHR and its percentage difference from experimentally measured power generation for excitation based on data set B

For this reason additional forced response data was collected from another bridge – the I-40/I-65 Broadway overpass, Nashville, Tennessee (36°09'20.9" N 86°47'21.4" W). Typical traffic conditions served as the excitation source inducing bridge vibrations during this data collection. A sample of the collected time series acceleration data is shown in Figure 16 along with its respective DFT.

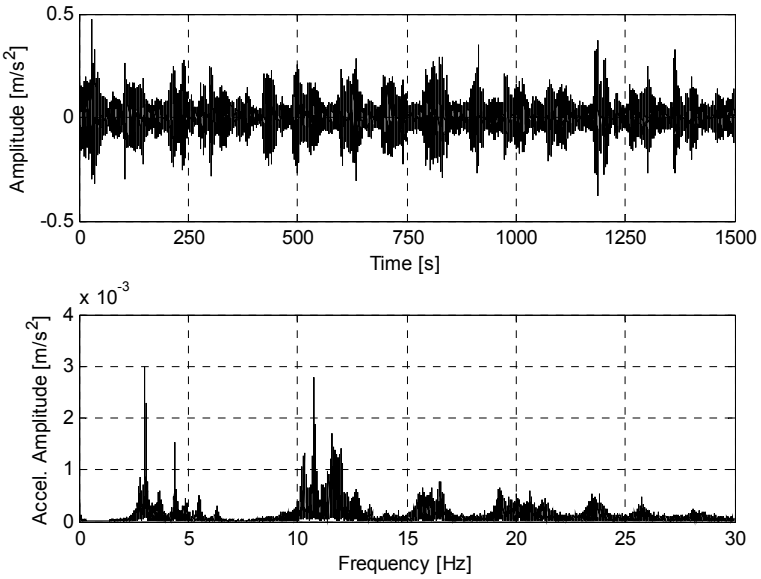

Figure 16: 25 minutes of typical traffic-induced time series acceleration data (top) and its respective DFT (bottom)

Several datasets of varying time lengths were collected to account for traffic light cycles. Some datasets were taken during constant traffic flow, while others provided more "average traffic flow" DFTs as in addition to including consistent excitation, they also included lengths of time during which the traffic light severely limited vehicle movement along the overpass. All of the collected dataset were used to create excitation representative of typical bridge vibrations for the experimental harvester. The harvester's experimentally measured average power delivery, as well as the power delivery predicted using the PHR estimation method, are displayed in Table 4. The specific details of the testing, including descriptions of the excitation and the employed electrical load, can be found in Section 0-1 on p.80.

Once again, the magnitudes of the errors between the PHR-predicted and experimentally measured average power generation values are quite small, never exceeding 5 %.

Given the amount and breadth of the experimental validation, the PHR method for average power generation was deemed to be an accurate analytical tool. This conclusion led to an important question: if PHR is capable of predicting power output based on expected excitation, harvester dynamics, and electric load, can it be used as a design tool for creating a more efficient energy harvester?

Table 4: Average power generation predicted by PHR and experimentally measured average power generation

Dataset #	Duration [min]	Excitation Scaling Factor	Experimentally Measured [mW]	PHR-predicted [mW]	Error [%]
1	1	20	2.52	2.49	-1.19
			2.51	2.50	-0.40
			2.56	2.51	-1.95
2	1	20	3.24	3.32	2.47
			3.15	3.29	4.44
			3.14	3.29	4.78
3	5	25	4.66	4.62	-0.86
			4.74	4.66	-1.69
			4.74	4.68	-1.27
4	5	20	2.04	2.03	-0.49
			2.06	2.03	-1.46
			2.06	2.03	-1.46
5	5	15	1.35	1.34	-0.67
			1.362	1.360	-0.15
			1.346	1.347	0.07
6	5	25	3.87	3.88	0.26
			3.89	3.88	-0.23
			3.90	3.88	-0.49
7	5	25	3.43	3.47	1.17
			3.44	3.46	0.61
			3.43	3.46	0.85
3-7	25	15	1.41	1.35	-4.05
			1.38	1.32	-4.62
			1.38	1.32	-4.70

IV. PHR AND MAXIMIZING POWER GENERATION

In order to provide a useful and generalizable answer to this question, three harvester architectures were analyzed using the PHR method. These architectures are depicted in Figure 51, they are: (a) the conventional vibration energy harvester, (b) the harvester array, and (c) the coupled harvester.

The conventional harvester and harvester array are two harvesting configuration that have been widely studied in literature [18, 19]. Conversely, the coupled harvester, although somewhat similar in design to some existing devices such as the dual-mass system proposed by Tang and Zuo [29], represents an original configuration to the best of the author's knowledge.

Using the same modeling approach as that which was described for the conventional harvester in Section II-1 on p. 5, Thévenin equivalent circuit representation for the harvester array and coupled harvester architectures were derived and are shown along with that of the conventional in Figure 18. Using these representation, PHR equations for the harvester array and coupled harvester were derived using the same procedure as that which was used for the conventional harvester in Section II-3.1 on p. 9.

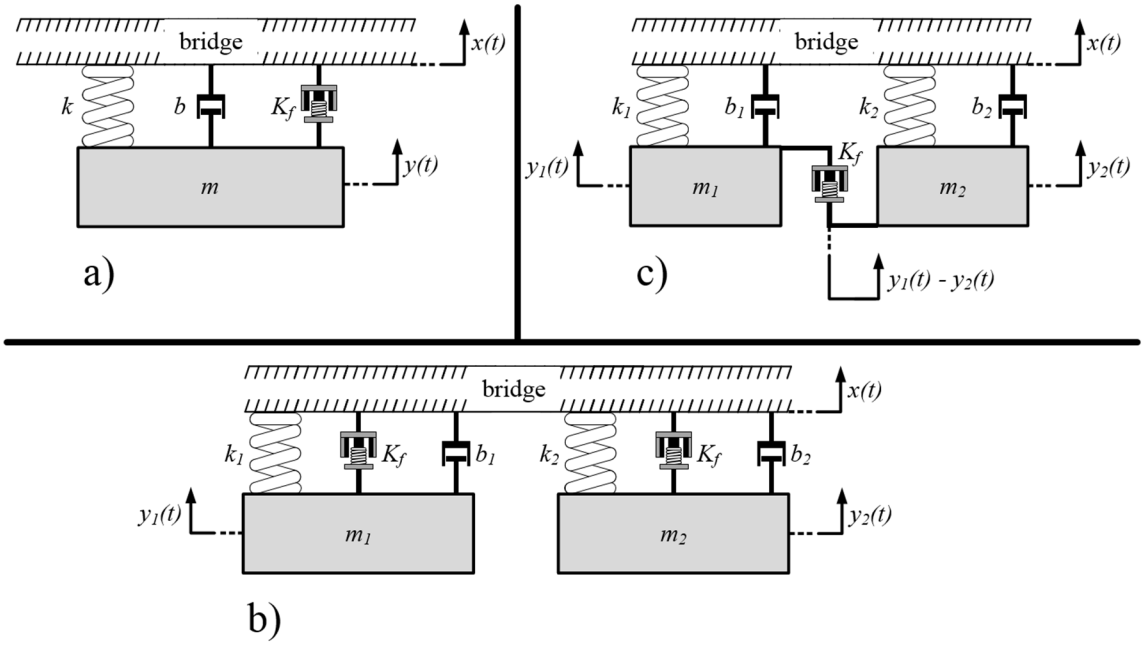

Figure 17: Three electromagnetic vibration energy harvester architectures – a) conventional harvester, b) harvester array and c) coupled harvester

By using numerical optimization algorithms, the specifics and assumptions of which can be found in Section 0-2.1 on p. 86, it was shown that a conventional harvester was capable of generating a significantly greater amount of average power than either the harvester array or the coupled harvester for the excitation shown in Figure 16 in the previous section The PHR curves of the three architectures, DFT of the excitation's acceleration amplitude squared, and resulting total average power generation values for each architecture (see legend) are shown in Figure 19. The reason for the superior performance of the conventional harvester stems from the dependence of a harvester's maximum achievable power on the square of the magnitude of its proof mass. This dependence is characteristic of any harvester that incorporates a mass-spring-damper type system to amplify the motion of a proof mass from which power is generated.

The effects of distributing proof mass and excitation frequency shifts on power generation, the proof that the coupled harvester can generate almost as much power as a harvester array for the considered excitation, and a quantitative demonstration for why the coupled harvester should be chosen over the conventional harvester when excitation amplitudes are highly variable are all discussed in detail in Section 0, 2.2-2.3 on pp. 90-102.

In addition to the findings listed in the previous paragraph, PHR-based analysis led to the following overarching conclusions regarding vibration energy harvester generation.

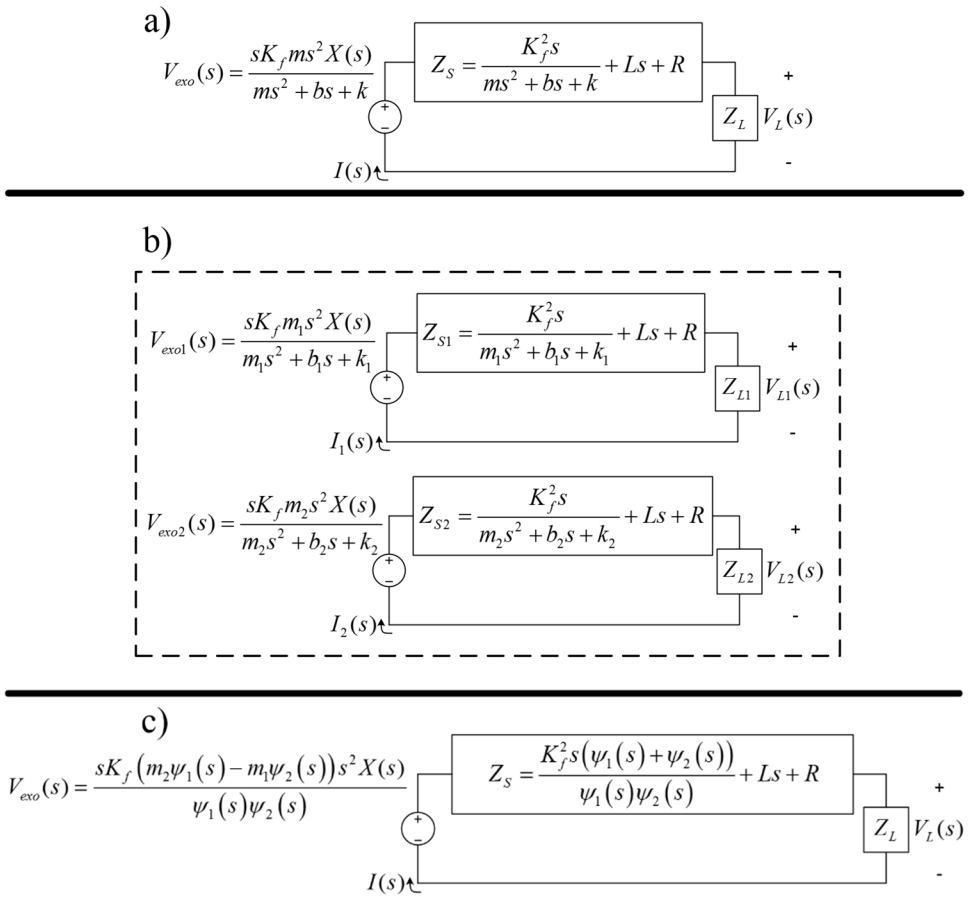

Figure 18: Thévenin equivalent circuit representations of a) conventional harvester, b) harvester array (note: comprised of two Thévenin equivalent circuits) and c) coupled harvester. Note: $\psi_1(s) = m_1 s^2 + b_1 s + k_1$ and $\psi_2(s) = m_2 s^2 + b_2 s + k_2$.

If the excitation source can be defined by a DFT the frequency content of which is largely static in both frequency and amplitude, a conventional harvester is the best harvesting architecture choice. By not distributing the proof mass and setting the mechanical natural frequency of the device to the largest frequency component observed in the excitation's DFT, maximum average power generation will be assured. Should several comparable peaks exist in the DFT, or should significant neighboring frequency content make one of the peaks that may not possess the largest magnitude seem highly lucrative, the best choice for setting the natural frequency of the device can be found using an optimization algorithm based on PHR as described in Section 0-2.12.1.2 on p. 87. For more details on optimizing power generation for excitation with a largely static DFT, see Section 0-3.1 on p. 102.

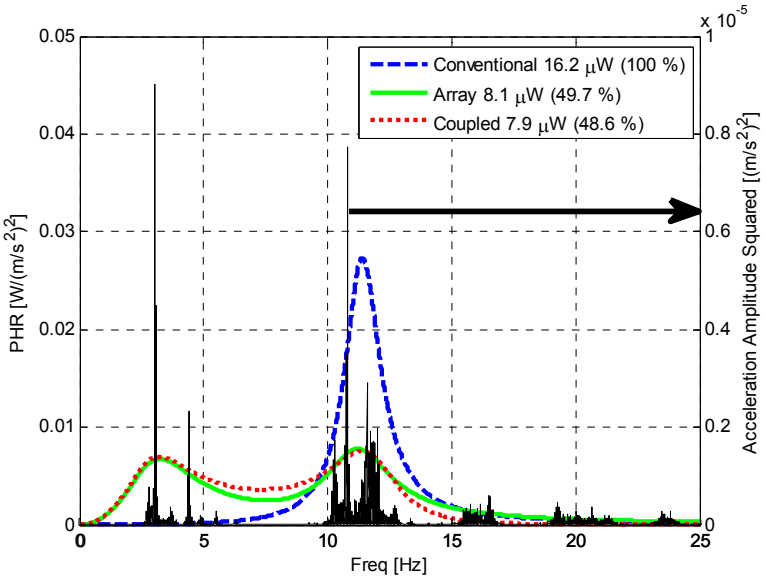

Figure 19: Average PHR-tuned power generation behavior of three vibration energy harvester architectures: conventional, two harvester array, and coupled harvester and DFT of the squared acceleration amplitude of the expected excitation

If the excitation source has a DFT which does not stay relatively constant and the components comprising the excitation have substantially varying amplitudes and frequencies, absolute rules for maximizing average power generation do not exist. In such cases, the best course of action is to obtain as much information about the excitation's DFT variation as possible and use this information, in conjunction with an accurate model of the harvester, an accurate model of the electrical load, and the PHR method to decide on the best choice of architecture and on how the parameters should be tuned. Answers to questions such as by how much the frequencies or amplitudes of the constituent components can vary, how fast do changes in the DFT occur, and which, if any, of the components are more constant than others can all be used by the PHR estimation technique to improve average power generation. More details on maximizing power generation for excitation with a varying DFT can be found in Section 0-3.2 on p. 103.

V. CONCLUSION AND TECHNICAL CONTRIBUTIONS OF PRESENTED WORK

1. Summary

The dissertational work described within this document was conducted in order to further the understanding of vibration energy harvesting. Specifically, it was desired to gain insight into how to efficiently harvest energy from excitation sources that vibrate at several frequencies simultaneously or the frequency content of which is variable with time.

To achieve this goal, two new analytical tools were created for analyzing linear vibration energy harvesters. The recent interest expressed in literature for increasing a vibration harvester's power using active electrical loading motivated the creation of the first tool – a technique for assessing the effect of the electrical active load on the harvester's overall dynamic stability. This tool works by analyzing a closed-loop system constructed using the Laplace domain representations of the relevant harvester dynamics and the proposed electrical load. This characterization of overall system dynamics as a closed-loop system allows the use of the well-established Nyquist Stability Criterion to assess whether the incorporation of the electrical load will result in overall stable or unstable system behavior.

The second tool which was developed is a new power generation metric termed "power harvesting ratio" or PHR. While also making use of the Laplace transform, this technique is based on incorporating the harvester, its excitation, and its electrical load into a Thévenin equivalent circuit. This representation then allows the use of the basic formula for the average AC power dissipated within a complex load impedance to determine the average power delivered to the harvester load. This method for estimating power generation has several key benefits. It facilitates the analysis of the effect of electrical load choice on power generation by looking at an "exogenous" voltage source affected only by the harvester's excitation and internal dynamics, but not the electrical load; this is in contrast to the traditional back EMF voltage source that is inherent to electromechanical power generation, the behavior of which is influenced by load choice. Additionally, the developed PHR technique uses the discrete Fourier transform of the expected excitation to easily arrive, not only at an accurate estimate of a harvester's total power generation from said excitation, but also at a frequency-power distribution which clearly shows each frequency component's contribution to this total power value.

These two tools are experimentally validated on a custom-made electromagnetic vibration energy harvester. The stability assessment tool is used to show why it is impossible to enforce a control law based on the maximum power transfer theorem. It is also used to accurately determine that a proposed trial active electrical load would result in stable overall harvester dynamics The PHR technique for estimating power generation is tested using multiple electrical loads; both passive (involving both, resistive and reactive components) and active. Multiple excitation types are used for testing, including vibration data recorded from a physical bridge being excited by typical traffic conditions. The PHR-predicted average power generation values are often within 5 % of experimentally measured results. In fact, the accuracy of the PHR method led to its use as an analysis and optimization tool during the final stages of the research presented within this manuscript. In doing so, along with the stability assessment tool, the PHR power estimation technique provided some valuable insight into multifrequency and variable frequency power generation that was sought at the start of this dissertational work.

2. *Technical Contributions of Dissertational Work*

2.1. APPENDIX A: Analytical Tools for Investigating Stability and Power Generation of Electromagnetic Vibration Energy Harvesters (accepted journal manuscript)

- Development of the Thévenin equivalent circuit representation of the vibration energy harvester using Laplace domain elements
- Development of the linear control-based closed-loop representation of the overall harvester dynamics and the subsequent development of the proposed stability assessment based on the Nyquist Stability Criterion
- Derivation of the Power Harvesting Ratio (PHR)
- Introduction of the experimental harvester setup
    - Validation of PHR using idealistic excitation comprised of pure sinusoids

2.2. APPENDIX B: Assessing Stability and Predicting Power Generation of Electromagnetic Vibration Energy Harvesters Using Physical Bridge Vibration Data (submitted journal manuscript)

- Collection of physical bridge data: free and forced response
    - Use of the modal assurance criterion (MAC) and free response data to identify bridge modes
    - Identification of modes in forced response data
- Validation of the stability assessment tool
    - Use of Nyquist Stability Criterion to show how MPTT-dictated load causes unstable harvester dynamics
    - Experimental validation of above claim
- Confirmation of PHR accuracy using collected forced response bridge data as experimental harvester excitation
- Use of a stable active load for power generation
    - Experimental demonstration of an active load achieving greater average power generation than an optimized purely resistive passive load

2.3. APPENDIX C: Analysis and Optimization of Electromagnetic Vibration Energy Harvesters Using the Power Harvesting Ratio Performance Metric (journal manuscript in preparation)

- Definitive validation of PHR accuracy on collected bridge vibration data produced by typical traffic conditions

- Analysis of three vibration energy harvesting architectures using PHR
    - Power generation analysis of the three architectures using three variable tuning embodiments
    - Use of numerical optimization algorithms based on PHR to maximize power generation
- PHR-based conclusions on tuning and architecture selection when excitation has a static DFT
- Analysis of the effect that frequency shifts and amplitude reductions have on total power generation of different harvesting architectures
- PHR-based recommendations for tuning approach when excitation has a DFT the components of which change in frequency and/or amplitude

APPENDIX A: ACCEPTED JOURNAL PAPER

Analytical Tools for Investigating Stability and Power Generation of Electromagnetic Vibration Energy Harvesters

Alexander V. Pedchenko, E. Bryn Pitt, and Eric J. Barth

Vanderbilt University
Nashville, TN

Accepted for publication in IEEE/ASME Transactions on Mechatronics
Citation information: DOI 10.1109/TMECH.2015.2469638

1. *Abstract*

This manuscript presents a general linear methodology for analyzing how choice of electrical load affects stability and average power generation of an electromagnetic vibration energy harvester. Using bond graph techniques, the entire electromechanical harvesting system is modeled as a dynamically equivalent electrical circuit and ultimately recast as a feedback control system. This modeling approach enables the use of well-established linear control tools to assess the overall stability of the energy harvesting system. These tools are used to show (1) why the load which would result in maximum power transfer from the harvester to the load, as established by the maximum power transfer theorem (MPTT), can only be achieved at a single frequency, and (2) how to ensure the system will always remain stable if the harvester is used in conjunction with an active load. Moreover, the presented modeling approach enables development of the power harvesting ratio—an analytical method for quantifying the harvester's power generation when multifrequency excitation is involved. A custom harvester was constructed for experimental evaluation of the power harvesting ratio when varying (1) the electrical load attached across the harvester leads and (2) the multifrequency vibrations used to excite the harvester.

2. *Introduction*

Powering sensor systems for actively monitoring the structural health of bridges has recently become an application area of particular interest for vibration energy harvesting systems [5, 6, 20, 34, 37]. The need for continuous bridge health-monitoring is longstanding [4, 38], and several sensor-based methods currently exist, including monitoring acoustic emissions for crack propagation in the bridge's concrete [20]and examining acceleration [5, 8, 33] or structural strain [5, 6, 34] data for indications of structural degradation. All of these monitoring methods require electrical power for sensor operation and data transmission; however, conventional means of powering these sensor systems—such as wiring to existing power lines or using replaceable/rechargeable batteries—are cost-prohibitive [8] or require regular maintenance. Using a self-contained, off-grid power source also enables greater flexibility in designing and implementing sensor networks without considering cabling [9]. Given that bridges are mechanically excited during normal use, electromechanical vibration energy harvesters are well-suited to bridge applications. Furthermore, powering sensor systems with kinetic energy from bridge vibrations has the advantage of energy always being available during periods of monitoring interest, unlike other alternative power generation methods such as solar and wind. The need to improve self-contained methods for powering bridge health-monitoring systems is the practical motivation for this paper.

The three most prevalent forms of electromechanical power generation are electrostatic, piezoelectric, and electromagnetic [10-12]. Electrostatic generation requires the incorporation of an external voltage

source, making it a suboptimal choice for autonomous install-and-forget power [19]. Piezoelectric generators tend to have limited lifetimes, as their performance degrades with the persistent direct straining of the piezoelectric material [10], and these materials tend to have rather poor mechanical properties [19]. Due to these drawbacks of electrostatic and piezoelectric power generation, and due to its relatively greater robustness and controllability [20], electromagnetic vibration energy harvesting is the best candidate for the considered application and is the focus of the research presented in this paper.

Most conventional electromagnetic vibration energy harvesters are similar in behavior to a linear mass-spring-damper [9, 19]. Inherently, such devices are able to harvest significant power only when their excitation frequency is at, or very close to, the device's mechanical natural frequency [10, 15, 19, 21]. This limitation is problematic for the application in question for several reasons: (1) different bridges vibrate at different frequencies [22]; (2) frequencies present in the vibration of a particular bridge will vary depending on traffic conditions [6]; and (3) a bridge will oscillate at several different frequencies simultaneously at any given mounting point for the harvester [22].

A significant amount of research has focused on addressing these issues associated with the single operating frequency of vibration energy harvesters. Most of the approaches existing in the literature can typically be grouped into one of two categories: (1) widening the power harvesting bandwidth of the generator by using an array of multiple harvesters with different natural frequencies; or (2) tuning the natural frequency of the generator to match the dominant frequency of the excitation [19]. Sari et al [23] and Ferrari et al [24] describe how an array comprised of multiple conventional cantilever beam generators having slightly different natural frequencies will result in a frequency bandwidth, as opposed to a single frequency, within which substantial energy capture occurs. Zhu et al [9] and Challa et al [16] experimentally investigate different approaches to alter the stiffness (and thereby the natural frequency) of a cantilever beam-type generator by using a linear motor to adjust the distance between a grounded magnet and another magnet on the cantilever. Peters et al [14] show that piezoelectric actuators could also be employed to alter a generator's effective stiffness for frequency tuning. These methods provide increased power generation at the cost of increased design complexity. The generator arrays require assembly of multiple non-interfering generators, while the tuning techniques typically require additional actuation to alter the harvester's equivalent mechanical stiffness. Alternative tuning methods aimed at avoiding the need for additional actuation were explored by Cammarano et al [15] and Bowden et al [26]. The proposed techniques still attempt to match the harvester's natural frequency to the dominant frequency of the excitation source, but the tuning is accomplished solely via an adjustable electrical load. Other approaches to addressing the single operating frequency problem of vibration generators are listed in references [19] and [18], which provide a thorough review of the literature. Regardless of the approach taken, however,

new tools for predicting performance are needed. The literature currently contains a gap for such tools, especially with regard to multifrequency excitation and active loads.

The contribution of this paper is a new analytical approach for evaluating the effect of a general electrical load on the performance of electromagnetic vibration energy harvesters. This approach is particularly useful for (1) assessing the effect of an active electrical load on the overall dynamic stability of a harvester; and (2) predicting harvester performance in response to multifrequency input excitation. The foundation of this approach is a control-design model for the harvester/electrical load system, detailed in Section II. Using this model, the harvester dynamics are depicted as a feedback control system in Section III. This depiction results in the formulation of simple requirements for the electrical load to ensure the overall harvester stability. Section IV contains the derivation of the "power harvesting ratio," a new analytical tool for predicting the average power generation of a harvester (given an electrical load) in response to single- and multifrequency input excitations. Section V contains the experimental validation of the power harvesting ratio for several electrical loads and several multifrequency input excitations. The tools and techniques presented in this paper have particular utility for future research involving active or adjustable electrical loads in electromagnetic vibration energy harvesters, as well as research related to multifrequency vibration energy harvesting more generally.

3. Modeling

Figure 20 shows a typical lumped-parameter schematic model of an electromagnetic vibration energy harvester ("harvester"), consisting of a proof mass m connected to a source of excitation (e.g. a bridge) through a linear spring (stiffness: k) and damper (damping: b). A linear motor with electromechanical transduction (back EMF) constant K_f is placed between the input excitation and the proof mass, in parallel with the mass and spring. Relative velocity between the proof mass and the input excitation generates back EMF (voltage) in the motor coil (electrical resistance: R, electrical inductance: L) which is coupled to an electrical load (represented as a generalized electrical impedance Z_L) attached across the leads of the motor. The overall dynamics of the harvester can be described by a system of two equations representing the coupled mechanical and electrical dynamics:

$$m\ddot{x} = m(\ddot{x} - \ddot{y}) + b(\dot{x} - \dot{y}) + k(x - y) + K_f i = m\ddot{p} + b\dot{p} + kp + K_f i \tag{19}$$

$$K_f \dot{p} = L\frac{di}{dt} + Ri + v_L, \tag{20}$$

where x is the displacement of the input excitation, y is the displacement of the proof mass, $p \stackrel{\text{def}}{=} x - y$ is the relative displacement between the input excitation and the proof mass, i is the coil current, and v_L is the voltage across the electrical load. Since power is ultimately harvested in the electrical domain, however, an

analysis of the effect of the electrical load on power generation requires that the harvester's dynamics be cast entirely into the electrical domain [30].

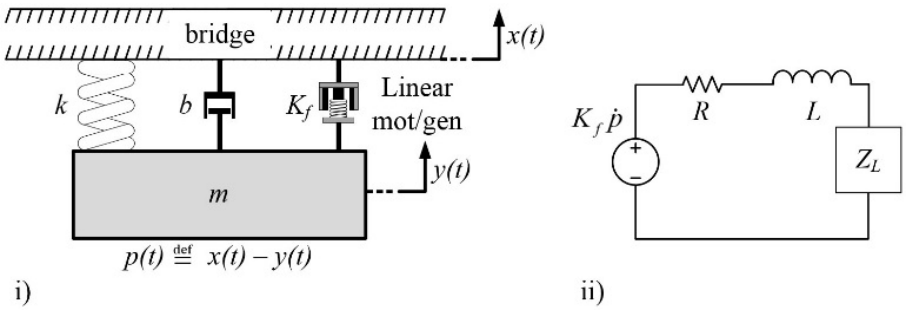

Figure 20: Lumped parameter representation of a vibration energy harvester: i) mechanical components; ii) electrical components

A representation of the harvester in a single energetic domain is easily realized through a bond graph model of the system, shown in Figure 21. The bond graph representation explicitly shows the flow of power through the harvester, making it particularly well suited to the analysis of harvester power generation. The input excitation is modeled as an ideal mechanical flow (velocity) source, which assumes that the dynamics of the harvester do not appreciably influence the input excitation. This assumption is valid as long as the mass of the harvester is substantially less than that of the source of the input excitation, as would be the case for a harvester attached to a bridge. The linear motor is modeled as an ideal electromechanical gyrator, which is consistent with the lumped-parameter model of a motor. In the bond graph, all mechanical dynamics of the harvester appear to the left of the gyrator, and all electrical dynamics appear to the right of the gyrator.

Proceeding from Figure 21, a purely electrical-domain representation of the harvester is created by reflecting the mechanical dynamics across the gyrator, into the electrical domain, as shown in Figure 22.

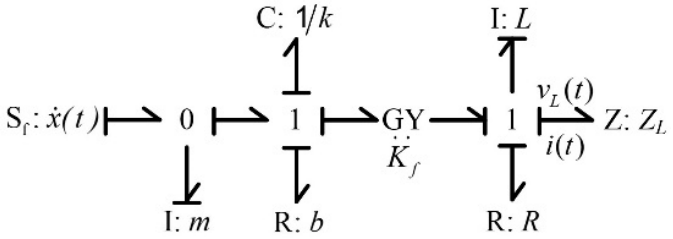

Figure 21: Bond graph representation of vibration energy harvester

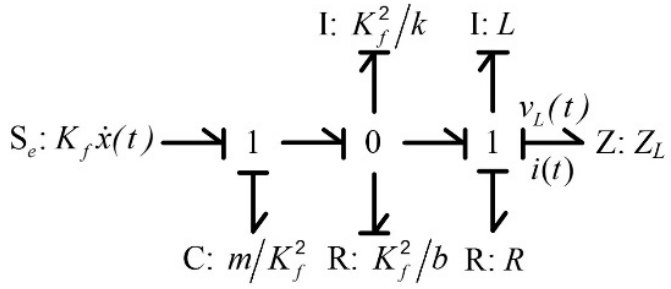

Figure 22: Bond graph representation of vibration energy harvester, cast entirely into the electrical domain

From the perspective of the electrical domain, the mechanical flow source from Figure 21 appears as an electrical effort (voltage) source in Figure 22. Furthermore, the behavior of the mechanical energy storage elements is inverted in the electrical domain view: a mechanical inertia (mass) appears as an electrical capacitor; a mechanical capacitor (spring) appears as an electrical inertia (inductor). The energetic behavior of dissipative elements, however, is unchanged.

Based on the single-domain representation in Figure 22, Figure 23 shows an electrical circuit with equivalent dynamics to the harvester, which allows the harvester to be studied using standard circuit analysis techniques. As previously suggested by [39], this equivalent circuit approach enables analysis of harvester power generation by means of the Thévenin equivalent circuit. Since the system is linear, it is convenient for analysis to proceed in the frequency domain, where the dynamics of electrical components can be described in terms of complex impedances. Whereas previous research has employed the Fourier transform [[40]] in modeling and lamented the complexity of the resulting power expressions, this paper employs the Laplace transform in order to facilitate a novel analysis of system stability and power generation, as discussed below. Furthermore, though not explicitly discussed in this paper, use of the Laplace transform allows for analysis of the transient response, which is not possible using the Fourier transform.

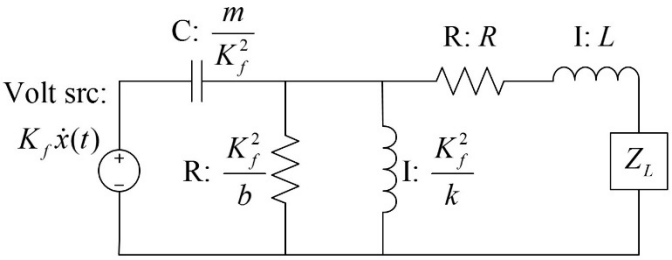

Figure 23: Electric circuit representation of vibration energy harvester

Using standard Laplace notation, where s denotes the Laplace variable, the impedance of an inductor L is given by $Z_I \stackrel{\text{def}}{=} sL$, and the impedance of a capacitor C is given by $Z_c \stackrel{\text{def}}{=} 1/(sC)$. The impedance of a

resistor R is purely real: $Z_R \triangleq^{\text{def}} R$. The circuit in Figure 23 can therefore be equivalently represented as the Thévenin circuit in Figure 24, which matches the findings of [39].

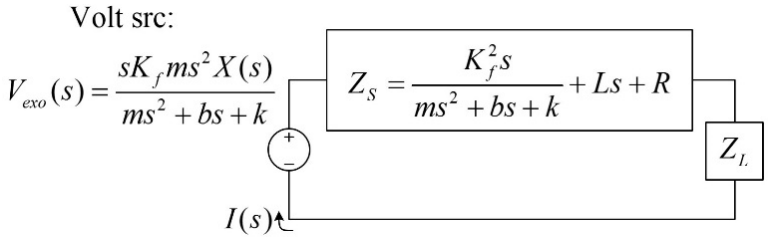

Figure 24: Thévenin equivalent circuit representation of the vibration energy harvester

In this final representation of the harvester, the mechanical input excitation is translated into an exogenous voltage source,

$$V_{exo}(s) = \left(\frac{mK_f s}{ms^2 + bs + k}\right) s^2 X(s), \tag{21}$$

where $X(s)$ is the Laplace transform of $x(t)$. The presence of a second-order mechanical filter in $V_{exo}(s)$ makes explicit the effect of the mass-spring-damper to amplify the input excitation over a narrow frequency band. Other combined mechanical and electrical dynamics of the harvester are represented in Figure 24 by a single source impedance:

$$Z_S(s) = \frac{K_f^2 s}{ms^2 + bs + k} + Ls + R. \tag{22}$$

A key benefit of this representation of the harvester is the separation of all internal dynamics of the harvester from the dynamics of the external electrical load. Assuming that the load impedance comprises only linear elements such that

$$V_L(s) = Z_L(s) I(s), \tag{23}$$

where $V_L(s)$ and $I(s)$ are the Laplace transforms of $v_L(t)$ and $i(t)$, respectively, the overall harvester dynamics can be written as a transfer function:

$$\frac{I(s)}{V_{exo}(s)} = \frac{1}{Z_S(s) + Z_L(s)}. \tag{24}$$

A transfer function between the exogenous voltage and the load voltage follows directly from (23) and (24):

$$\frac{V_L(s)}{V_{exo}(s)} = \frac{Z_L(s)}{Z_L(s) + Z_s(s)}. \tag{25}$$

As an alternative to the preceding bond graph analysis, harvester dynamics in the form of (21), (22), (24), and (25) can be derived by combining the Laplace transforms of (19) and (20), eliminating $P(s)$, and substituting (23).

4. Harvester Stability

Expressing the dynamics of the harvester as a transfer function enables an analysis of the harvester using standard techniques of linear control theory. An immediate benefit of this approach is the ability to directly assess the effect of the electrical load impedance (whether active or passive) on the overall stability and stability robustness of the harvester. The transfer function (24), representing the harvester dynamics, can be recast as the feedback system in Figure 25.

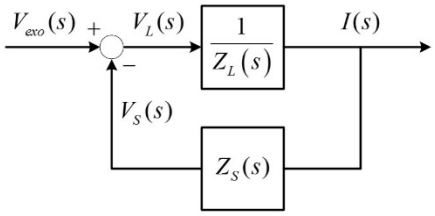

Figure 25: Feedback system with closed-loop dynamics equivalent to dynamics of the harvester

Viewed in this light, the "closed-loop" stability of the harvester can be analyzed in terms of the properties of the open-loop transfer function

$$G_{OL}(s) = \frac{Z_s(s)}{Z_L(s)}. \tag{26}$$

It should be noted from (22) that the source impedance, $Z_s(s)$, represents a passive system, which implies that $Z_s(s)$ does not contribute any unstable poles to $G_{OL}(s)$. Therefore, unstable "open-loop" poles of $G_{OL}(s)$ are simply the nonminimum-phase zeros of $Z_L(s)$. This fact can be used in conjunction with the Nyquist Stability Criterion to give several conditions on the choice of load impedance to ensure the stability of the harvester, depending on the number of nonminimum-phase zeros in $Z_L(s)$.

4.1. Case I: $Z_L(s)$ has no nonminimum-phase zeros

In this case, a necessary and sufficient condition for the stability of a harvester is

$$-180° \leq \measuredangle G_{OL}(s) \leq 180° \tag{27}$$

for all frequencies $s = j\omega$. Since $Z_s(s)$ is passive, (27) will be satisfied for any passive load impedance, meaning that a passive load impedance will always result in stable harvester dynamics. Additionally, (27) provides the design criterion to ensure stable harvester dynamics when designing a more general (i.e. active) load impedance. The encirclement criterion also enables the calculation of stability margins, which can be of particular concern when using active electronics to emulate a passive load impedance.

4.2. Case II: $Z_L(s)$ has nonminimum-phase zeros

In this case, $Z_L(s)$ will contribute unstable open-loop poles to $G_{OL}(s)$. In order to achieve stable harvester dynamics, the Nyquist Stability Criterion stipulates that the Nyquist plot of $G_{OL}(s)$ must have a number of counterclockwise encirclements of the critical point equal to the number of nonminimum-phase zeros in $Z_L(s)$ (the number of unstable open-loop poles). This requirement to ensure the stability of the harvester does not translate into a strict condition on the phase and gain of $Z_L(s)$; however, it should be noted that a load impedance with nonminimum-phase zeros whose phase satisfies

$$-90° \leq \measuredangle Z_L(s) \leq 90° \tag{28}$$

for all frequencies $s = j\omega$ does not result in any encirclements, and therefore always results in unstable harvester dynamics.

4.3. Stability Case Study: Maximum Power Transfer Theorem

Finally, as an example of the importance of assessing the effect of the load impedance on harvester stability, consider the load impedance dictated by the maximum power transfer theorem when implemented at all frequencies simultaneously. Stated concisely, the maximum power transfer theorem states that maximum power will be transferred to the load impedance when the load impedance is equal to the complex conjugate of the source impedance. In previous research (e.g., Bowden et al [26]), such loads have been implemented at a single frequency using active electronics to emulate a load impedance that matches the gain and phase of the load impedance prescribed by the maximum power transfer theorem only at the intended frequency. However, based on the source impedance (22), the maximum power transfer theorem implemented at all frequencies dictates the following load impedance:

$$Z_L(s) = Z_s^*(s) = \frac{-K_f^2 s}{ms^2 - bs + k} - Ls + R. \tag{29}$$

Assuming all system parameters are positive, this particular load impedance has three nonminimum-phase zeros; however, the phase of the system satisfies (28), which implies that implementing the maximum power transfer theorem at all frequencies will always result in unstable harvester dynamics. This fact can be verified by directly substituting (22) and (29) into (25), to find that the harvester transfer function,

$$\frac{V_L(s)}{V_{exo}(s)} = \frac{(R - Ls)(m^2 s^4 + (2mk - b^2)s^2 + k^2) - K_f^2 s(ms^2 + bs + k)}{2Rm^2 s^4 + \left(4Rmk - 2Rb^2 - 2K_f^2 b\right)s^2 + 2Rk^2} \tag{30}$$

is clearly unstable according to the Routh-Hurwitz stability criterion.

This result implies that the maximum power transfer function cannot be implemented over a frequency band. Although this result may not be a surprising conclusion for the case of the maximum power transfer theorem, the example illustrates the benefit of a control-centric modeling approach for assessing the harvester stability for any general linear load impedance.

5. Power Harvesting Ratio: A Power Generation Metric

The proposed modeling approach allows the development of a technique to estimate a particular harvester's power generation with an electrical load of known impedance and excited by a displacement with a known amplitude spectrum. This section presents a detailed derivation of this technique, which has been termed the "power harvesting ratio."

The following analysis of average power generation assumes steady-state oscillations, as is common in frequency domain analysis, and stable harvester dynamics as discussed in Section 4. This assumption implies that the circuit depicted in Figure 24 is an alternating current (AC) circuit. A general expression for average power absorbed by an impedance in an AC circuit is:

$$\overline{\mathbb{P}} = \frac{1}{2}|V||I|\cos(\varphi), \tag{31}$$

where $\overline{\mathbb{P}}$ is the average power absorbed by the load impedance, $|V|$ is the amplitude of the sinusoidal voltage across this impedance, $|I|$ is the amplitude of the current running through this impedance and φ is the phase between V and I. Using this expression, the average frequency-dependent power absorbed by the harvester's load impedance in the circuit shown in Figure 24 is defined by

$$\overline{\mathbb{P}}(\omega) = \frac{1}{2}|V_L(s)||I(s)|\cos\left(\measuredangle Z_L(s)\right)\Big|_{s=j\omega} \tag{32}$$

Using (24) and (25) evaluated at $s = j\omega$ and (32), the relationship between this average power quantity and the exogenous voltage source $V_{exo}(s)$ is obtained as:

$$\frac{\overline{\mathbb{P}}(\omega)}{|V_{exo}(s)|^2}\Big|_{s=j\omega} = \frac{1}{2}\left|\frac{V_L(s)}{V_{exo}(s)}\right|\left|\frac{I(s)}{V_{exo}(s)}\right|\cos(\measuredangle Z_L(s))\Big|_{s=j\omega} \tag{33}$$

Equation (33) then allows the use of (21) to arrive at the expression defining how the harvester's excitation affects the average power delivered to the load impedance. The intermediate step in obtaining this expression and the expression itself are shown in (34) and (35) respectively:

$$\frac{\overline{\mathbb{P}}(\omega)}{\left|\frac{K_f ms}{ms^2+bs+k}s^2X(s)\right|^2}\Bigg|_{s=j\omega} = \frac{1}{2}\left|\frac{Z_L(s)}{Z_S(s)+Z_L(s)}\right|\left|\frac{1}{Z_S(s)+Z_L(s)}\right|\cos(\measuredangle Z_L(s))\Big|_{s=j\omega}, \tag{34}$$

$$\mathrm{H}(\omega) \stackrel{\text{def}}{=} \frac{\overline{\mathbb{P}}(\omega)}{|s^2X(s)|^2}\Big|_{s=j\omega} = \frac{1}{2}\left|\frac{Z_L(s)}{|Z_S(s)+Z_L(s)|^2}\right|\left|\frac{K_f ms}{ms^2+bs+k}\right|^2\cos\left(\measuredangle Z_L(s)\right)\Big|_{s=j\omega} \tag{35}$$

Equation (35) defines the mathematical relationship between the acceleration of the excitation squared and the average power generated at a particular frequency. This relationship is designated the "power harvesting ratio" and will be henceforth denoted by $\mathrm{H}(\omega)$.

Defining the power harvesting ratio in the form shown in (35) is not arbitrary. $\mathrm{H}(\omega)$ is chosen to be normalized with respect to excitation in order to be able to easily quantify the amount of power harvested from each frequency component by simply multiplying $\mathrm{H}(\omega)$ by the frequency spectrum of the excitation's acceleration amplitude squared. The reason to use acceleration of the excitation as opposed to displacement is so that the ability of the harvester to generate power at different frequencies is properly portrayed. Specifically, if the excitation's acceleration is kept constant, $m\ddot{x}(t)$, the quantity which can be construed as the exogenous physical input in (19), stays constant as well. In this case, when the harvester generates more power at a certain frequency, the result necessarily implies that the harvester operates more efficiently at that frequency. However, if displacement is kept constant, $m\ddot{x}(t)$ grows with frequency. This would result in the harvester generating a considerable amount of power at very high frequencies not because of efficient operation, but because of the much larger magnitude of the input (i.e., much more available power).

To reiterate, defining $\mathrm{H}(\omega)$ in the form shown in (35) has two benefits. Firstly, simply plotting (35) versus frequency is a convenient way to quantify the harvester's efficiency when generating power subject

to different excitation frequencies. Secondly, and more importantly, the power harvesting ratio method allows a calculation of the contribution to total average power generation of each individual frequency component in multifrequency excitation. The following section describes the details of the experimental validation of $H(\omega)$.

6. Experimental Setup and Results

6.1. Description of the Experimental Setup

To assess the accuracy of predicting the average power generation of a vibrational electromagnetic energy harvester using $H(\omega)$, the prototype depicted in Figure 26 was designed and built as an experimental platform.

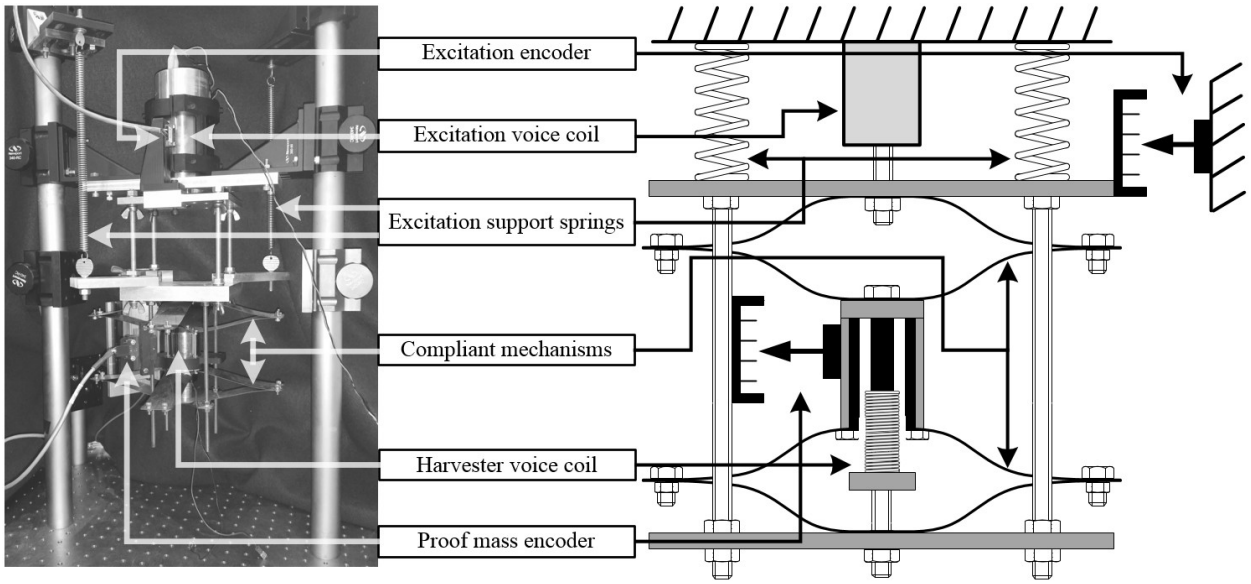

Figure 26: Photograph and schematic of the experimental electromagnetic vibration energy harvester

The linear motor's (BEI linear voice coil LA17-28-000A) housing is suspended by the compliant mechanisms, which move only along the intended axis without coming into contact with the motor's coil. The coil itself is rigidly attached to the excitation source. This accomplishes the alignment of the harvester's proof mass without the use of bearing surfaces, which tend to increase parasitic losses. In this configuration, the housing of the linear voice coil serves as a proof mass, the relative motion of which results in power generation.

In their design, the compliant mechanisms were approximated as beams that are cantilevered at one end and constrained to translate in the vertical direction at the other; this allowed their equivalent stiffness to be estimated. The width, length, and thickness of the compliant mechanisms were chosen to achieve a stiffness

such that the harvester would have a natural frequency of 7.8 Hz, which is close to the middle of the frequency range of interest. This range of interest was chosen by noting that bridges' dominant modes of oscillation are typically in the range of 3-12 Hz [5, 6, 33, 34].

A larger voice coil (BEI linear voice coil LAH28-52-000A) was used to produce excitation of the harvester. It was powered using a Kepco BOP 36-6 servo amplifier. The displacement produced by this linear voice coil and the displacement of the harvester's proof mass were measured using two optical encoders (U.S. Digital optical encoder modules EM1 used in conjunction with 500 counts/inch linear strips and x4 quadrature to produce 2000 count/inch resolution). The input excitation encoder was used for closed-loop control of the excitation voice coil. Good alignment for this encoder was enforced by coupling the harvester and the excitation voice coil using a linear bearing which cannot be seen in the photograph of Figure 26 as it is behind the harvester. Two extension springs were used to help support the weight of the harvester, reducing the static load on the excitation voice coil, and thereby allowing it to produce higher dynamic excitation forces. The voltage across the harvester's load was measured with a DAQ card and the current flowing through the harvester leads was measured using an inductive current probe (Agilent 1146A). Mathworks Matlab and Simulink Real-time R2014a were used in conjunction with National Instruments PCI-6259 DAQ card for control of the experimental setup and data acquisition.

Intrinsic harvester parameters (i.e., those not dependent on the choice of electrical load) needed to use (17) to predict the average amount of generated power are listed in Table 5. The harvester's linear voice coil's motor constant, K_f, and inductance, L, were taken directly from its data sheet. The motor's resistance, R, was measured. Parameter estimation run on experiments with no electrical load was used to determine the proof mass, m, and equivalent stiffness, k, as well as the mechanical damping parameter, b.

Table 5: Experimental Harvester Parameters

Parameter	Value
m	0.697 kg
b	6.925 N/(m/s)
k	1665 N/m
K_f	17.8 N/A or V/(m/s)
L	0.0031 H
R	7 Ω

6.2. Experimental Testing and Results

This section presents an experimental validation of the proposed power harvesting ratio approach. A single-frequency excitation is presented first, followed by several multifrequency excitations with different electrical loads. All cases demonstrate how $H(\omega)$ from (17) is used to estimate the harvester's power

generation from the load impedance and the measured frequency spectrum of the excitation characterizing the input. For multifrequency excitations, $H(\omega)$ yields an estimate of both the average power harvested at each frequency as well as the overall average power.

6.2.1. Single-frequency Excitation

Substituting the parameters from Table 5 into the power harvesting ratio (35) allows a calculation of the power generated per unit of squared acceleration given the frequency (or frequencies) of excitation and the choice of electrical load. The goal of this validation testing was to assess (35) is capable of predicting harvester power generation given that the excitation is comprised of only a single frequency. For these experiments, the electrical load was chosen based on the MPTT implemented at the natural frequency of the harvester using passive components. Bowden et al [26] provide a convenient way to solve for this load with (36) and (37) (the forms of the equations are kept, but the variables have been changed to match the variable definitions used in this manuscript):

$$R_{MPTT}(\omega) = R + \frac{K_f^2 b\omega^2}{(k - m\omega^2)^2 + (b\omega)^2} \tag{36}$$

$$X_{MPTT}(\omega) = \frac{K_f^2 (m\omega^2 - k)\omega}{(k - m\omega^2)^2 + (b\omega)^2} - \omega L. \tag{37}$$

$R_{MPTT}(\omega)$ determines the resistive portion and $X_{MPTT}(\omega)$ determines the reactive portion of the harvester load needed to achieve maximum power generation, assuming the harvester is excited at a frequency ω. Substituting $\omega = \omega_n = \sqrt{k/m} = 48.9$ rad/sec into (36) and (37) yields:

$$R_{MPTT}(\omega_n) = R + \frac{K_f^2}{b} = 52.7\ \Omega \tag{38}$$

$$X_{MPTT}(\omega_n) = -L\omega_n = -0.152\ \Omega \tag{39}$$

Thus, the load impedance necessary to satisfy MPTT at the harvester's mechanical natural frequency would include a 52.7 Ω resistance and a 0.135 F capacitance ($-1/(0.135 \times \omega_n) = -0.152$). However, given the insignificant contribution of the capacitance to the total load impedance (and in turn, power generation) in the excitation frequency range of interest (3-12 Hz), it was decided to exclude it from the load. Thus, the electrical load used to assess the accuracy of (35) in predicting harvester power generation at single, discrete frequencies was $Z_L = R + K_f^2/b = 52.7\ \Omega$.

Figure 27 shows the power harvesting ratio calculated from (35) and experimentally measured values of the power harvesting ratio. The latter were obtained by subjecting the harvester to excitation 1 mm in amplitude at distinct, individual frequencies in the 3-12 Hz range. The resulting voltage across the 52.7 Ω load resistance was measured and used to calculate the average "generated power" (i.e., power dissipated across the load resistance) according to:

$$\overline{\mathbb{P}}_{exp} = \frac{\overline{v_L}^2}{R_L}, \tag{40}$$

where $\overline{\mathbb{P}}_{exp}$ is the experimentally measured average power generation, $\overline{v_L}$ is the average load voltage measured, and R_L is the load resistance of 52.7 Ω.

The average power at each frequency of excitation was normalized with respect to the excitation's acceleration amplitude squared. This amplitude was determined by taking the discrete Fourier transform (DFT) of the excitation's measured displacement to determine the experimental average amplitude of the displacement (instead of assuming it was exactly 1 mm as was commanded to the excitation voice coil) and its frequency. The amplitude and frequency of the displacement were then used to calculate the amplitude of acceleration by assuming purely sinusoidal motion.

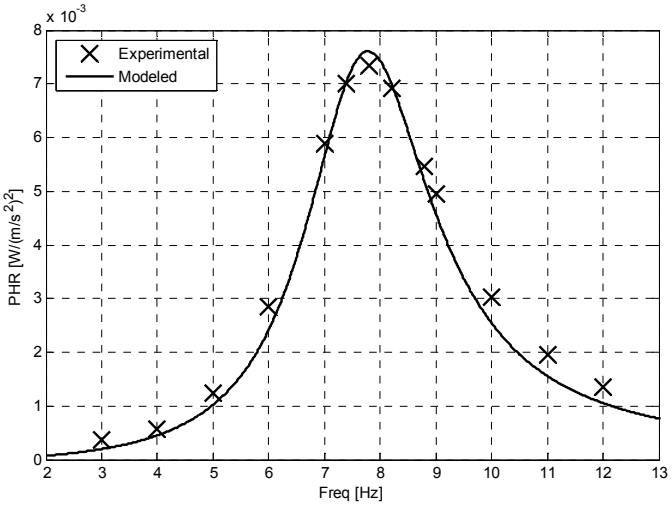

Figure 27: Modeled and experimental power harvesting ratio for single-frequency excitation for $Z_L = R + K_f^2/b = 52.7\ \Omega$

As further support for the validity of the power harvesting ratio approach, consider (41) derived by Stephen (equation (55) in [35]) which solves for the average power delivered to the electrical load by a conventionally tuned harvester at the harvester's mechanical natural frequency (i.e., a purely resistive load is chosen according to (38)):

$$\bar{P}(\omega_n) = \frac{K_f^2 m^2 \omega_n^4 Y^2}{8b\left(bR + K_f^2\right)} \tag{41}$$

The variables used by Stephen in [35] have been replaced in (41) by those representing the same quantities within this manuscript for the sake of consistency. The sole variable requiring introduction is Y, which is the amplitude of the excitation's displacement. If (41) is normalized with respect to the amplitude of acceleration squared (i.e., divided by $Y^2\omega_n^4$) to obtain an expression equivalent to $H(\omega)$, and the appropriate quantities from Table 5 are substituted, the resulting quantity is 7.6 mW/(m/s^2)^2. This value exactly matches $H(\omega_n)$ calculated from (35). The experimentally measured value at ω_n in Figure 27 was 7.4 mW/(m/s^2)^2 (3 % error).

6.2.2. Multifrequency Excitation

Ensuring that (35) can predict harvester power generation for a given frequency given a certain load choice with a good degree of accuracy is an important basic check. However, the main purpose of the power harvesting ratio approach is to provide a relatively simple and fast method for analyzing power generation for cases where excitation is comprised of several significant frequency components (e.g., bridge vibrations).

To assess how well H(ω) accomplishes this, the harvester was subjected to excitation having four frequency components: ω_n, $1.5\omega_n$, $2\omega_n$, and $2.5\omega_n$. The amplitude components were chosen to mimic real-world bridge span vibrations in which components having higher frequencies tend to have lower acceleration amplitudes [22]. Figure 28 shows the spectrum of the squared amplitude of the acceleration of the harvester's excitation, with units indicated on the left-hand y-axis. Figure 28 also shows the power harvesting ratio calculated from (35), with units indicated on the right-hand y-axis. The harvester's electrical load was unchanged from that used for the single frequency testing ($Z_L = R + K_f^2/b = 52.7\ \Omega$).

Figure 29 shows the harvester's predicted average power generation as a function of frequency using the data from Figure 28. In order to predict the average power generated by the harvester at each frequency, the squared acceleration amplitude data shown in Figure 28 is multiplied by the corresponding H(ω) value at each frequency according to (42):

$$\overline{\mathbb{P}}(\omega_i) = a^2(\omega_i)\cdot \mathrm{H}(\omega_i), \tag{42}$$

where ω_i is a particular frequency expressed in the DFT data, and $\overline{\mathbb{P}}(\omega_i)$, $a^2(\omega_i)$, and $\mathrm{H}(\omega_i)$ are the average generated power, the squared magnitude of the excitation's acceleration, and the power harvesting

ratio value at that frequency, respectively. Note that (42) is not a new equation, per se, but instead explicitly shows how (35) is practically implemented to calculate harvester power generation. Finally, the predicted total average power generation $\overline{\mathbb{P}}_{tot}$ can be calculated by summing the predicted average power generated at each frequency over all frequencies in the acceleration amplitude spectrum:

$$\overline{\mathbb{P}}_{tot} = \sum_{i=1}^{N} \overline{\mathbb{P}}(\omega_i). \tag{43}$$

Figure 29 shows that the majority of the harvester's power generation occurs at the device's mechanical natural frequency, as expected. However, Figure 29 also allows a quantification of the non-insignificant portion of the total power that is generated at other frequencies (approximately 14 %). Figure 29 illustrates the unique advantage of using $\mathrm{H}(\omega)$ for power generation analysis. The power harvesting ratio not only provides an accurate estimate of the harvester's power generation because it encompasses all of the frequency content present in the excitation, but additionally, it clearly depicts the contribution of each individual frequency to this overall power generation.

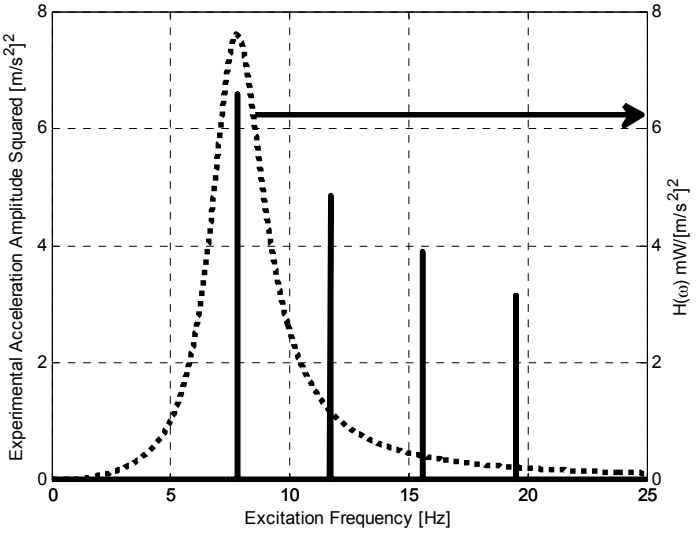

Figure 28: Spectrum of the squared amplitude of the acceleration of the harvester's excitation and calculated power harvesting ratio (for $Z_L = R + K_f^2/b = 52.7\ \Omega$)

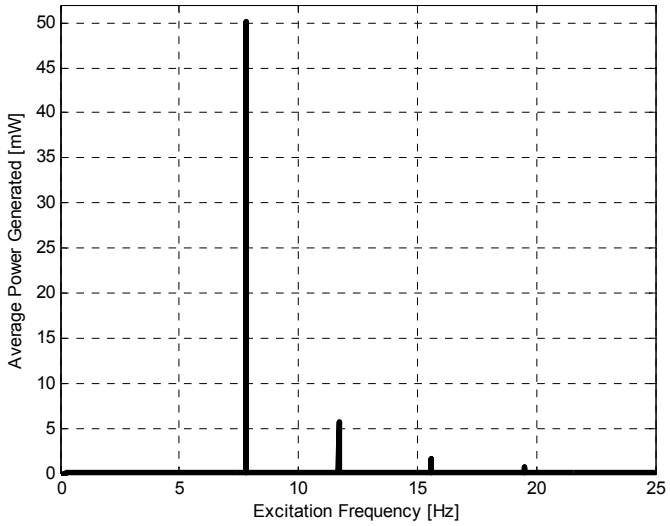

Figure 29: Average power generated by the harvester as a function of frequency

To further experimentally validate the accuracy of the power harvesting ratio method in predicting net power generation, a number of additional experiments were performed using the harvester setup. These experiments involved varying both the electrical load of the harvester, and the excitation frequency and amplitude components from which the harvester generated power. Excitation conditions and power generation of these additional tests are displayed in Table 6. As can be seen from the table, two different harvester excitations were used, one with three and another with four frequency components (both having the largest acceleration amplitude frequency component at ω_n, since energy harvesters are tuned to have their natural mechanical frequency match the dominant frequency component of the excitation source). The electrical load was varied via the use of different load resistance values as well as incorporation of a load capacitance large enough to have an effect at the excitation frequencies used.

As can be seen from the table error values, using $\mathrm{H}(\omega)$ is an accurate method for predicting power generation from a given harvester provided that the electrical impedance of the harvester's load and the frequency content of the excitation are known.

Table 6: Modeled and Experimental Harvester Power Generation Values for Different Multifrequency Input Excitations and Various Load Impedances

Test #	Primary Excit. Frequencies [Hz]	Corresponding Accel. Amplitudes [m/s^2]	Load Resistance [Ω]	Load Capacitance [μF]	Model Avg. Pow. Gen. [mW]	Experimental Avg. Pow. Gen. [mW]	Modeling Error [%]
1	7.8, 11.7, 15.6, 19.5	2.57, 2.20, 1.97, 1.77	52.7	0	58.9	58.1	1.4
2	7.8, 11.7, 15.6, 19.5	2.57, 2.20, 1.97, 1.77	52.7	0	58.8	58.0	1.4
3	7.8, 11.7, 15.6, 19.5	2.57, 2.19, 1.96, 1.76	100	0	50.4	51.3	-1.8
4	7.8, 11.7, 15.6, 19.5	2.57, 2.19, 1.96, 1.76	100	0	50.6	51.6	-1.9
5	7.8, 11.7, 15.6, 19.5	2.57, 2.22, 1.96, 1.76	19.7	0	53.7	51.6	4.1
6	7.8, 11.7, 15.6, 19.5	2.57, 2.22, 1.98, 1.77	19.7	0	54.0	51.9	4.0
7	6.5, 7.8, 9.3	1.76, 2.55, 1.83	52.7	0	74.7	73.8	1.2
8	6.5, 7.8, 9.3	1.76, 2.56, 1.84	52.7	0	75.0	74.2	1.1
9	6.5, 7.8, 9.3	1.77, 2.55, 1.83	100	0	62.8	63.0	-0.4
10	6.5, 7.8, 9.3	1.76, 2.55, 1.82	100	0	62.6	62.8	-0.4
11	6.5, 7.8, 9.3	1.76, 2.56, 1.86	20.3	0	68.5	63.2	8.4
12	6.5, 7.8, 9.3	1.76, 2.56, 1.86	20.3	0	68.5	63.3	8.3
13	6.5, 7.8, 9.3	1.77, 2.51, 1.83	20.3	280	26.6	24.4	9.2
14	6.5, 7.8, 9.3	1.77, 2.51, 1.83	20.3	280	26.6	24.5	8.7
15	6.5, 7.8, 9.3	1.77, 2.53, 1.83	52.7	280	45.5	41.2	10.4
16	6.5, 7.8, 9.3	1.77, 2.52, 1.82	52.7	280	45.3	41.2	10.0
17	6.5, 7.8, 9.3	1.77, 2.53, 1.82	100	280	48.9	47.1	3.8
18	6.5, 7.8, 9.3	1.77, 2.53, 1.82	100	280	48.9	47.0	4.0

7. Conclusions

This paper presents new linear techniques for analyzing electromagnetic vibration energy harvesters when active loading is employed and/or when multifrequency excitation is present.

Assuming linear dynamics for the harvester and electrical load, a control-based representation of an electromagnetic vibration energy harvester was used to formulate simple requirements for the electrical load to ensure overall harvester stability. These requirements are particularly useful for designing and analyzing active electrical loads, where harvester stability is a concern.

Another key contribution of this paper is the development of the power harvesting ratio—a new tool for estimating a harvester's average power generation. This tool enables quick and accurate prediction of the power generation of a harvester undergoing periodic, steady-state excitation, even when that excitation is comprised of multiple frequency components (e.g., vibrations characteristic of bridge spans). In fact, the power harvesting ratio is particularly well-suited for the task of analyzing multifrequency excitation as it explicitly quantifies the contribution of power generation at each frequency to the overall average power

generation. Experimental data confirmed that the power harvesting ratio yields an accurate prediction of generated power for a given electrical load impedance and a known steady-state excitation.

8. Acknowledgements

The authors would like to thank the National Science Foundation (Grant #1035627) for providing financial support that made the presented research possible. The authors would also like to thank Mark E. Hofacker for his work on the design and assembly of the experimental harvester setup, as well as his contribution to the theory and subsequent development of the power harvesting ratio.

APPENDIX B: SUBMITTED JOURNAL PAPER

Assessing Stability and Predicting Power Generation of Electromagnetic Vibration Energy Harvesters Using Physical Bridge Vibration Data

Alexander V. Pedchenko, Janette J. Meyer, and Eric J. Barth

Vanderbilt University
Nashville, TN

Submitted for publication to IEEE/ASME Transactions on Mechatronics
on Novemer 19th, 2015

1. Abstract

This paper presents the use of the power harvesting ratio (PHR) approach for evaluating the power harvesting capabilities of an electromagnetic vibration energy harvester. This was done for different electrical loads and measured bridge vibration data displaying multiple frequency components. Bridge vibration data was collected and characterized. The modes of the bridge were determined using a model sledge hammer, and the response of the bridge to a single vehicle was measured. Analysis of the data revealed that several of the modes contributed toward a response with multiple non-negligible frequency components. Measured bridge time-series data was then replayed on an experimental setup with an electromagnetic vibration energy harvester. Six electrical loads were implemented on the experimental platform: four passive loads and two active loads. The PHR approach was used to predict the average power from each load. Experimentally measured average power was within 6% of the predicted average power. The PHR approach was also used to successfully predict harvester instability for the active load dictated by the maximum power transfer theorem, and validated experimentally. This paper demonstrates the utility of the PHR approach in evaluating harvester stability and performance for multifrequency excitations and sophisticated electrical loads including active loads.

2. Introduction

According to the most recent data collected by the National Bridge Inventory, in 2013 approximately 25% of U.S. bridges were classified as “structurally deficient” or “functionally obsolete” [1]. Most bridges are inspected only once every 24 months with the caveat that “structures with advanced deterioration or other conditions warranting close monitoring may be inspected more frequently” [3]. The poor state of many of the nation’s bridges coupled with the need to inspect those in particularly bad condition more often results in a large demand for frequent structural monitoring that cannot be fulfilled in a timely manner. One way to address this demand is through implementation of autonomous structural monitoring.

There have been multiple sensing options proposed for structural health monitoring. Strain gauge placement at key locations [5], pattern recognition of bridge acceleration data [6], and acoustic emissions monitoring [7] are just some of the suggested techniques to detect structural deterioration. These sensing methods share one advantageous characteristic – they can be implemented to function remotely.

Ultimately, remote condition monitoring requires that the sensors acquire pertinent data concerning the state of the bridge, record it, and transmit it to a location where the data can be analyzed and processed. All of these processes require electrical power, which ideally, in order to make the sensor network truly autonomous, would come from a source requiring no maintenance. Hard-wiring power and data transfer cables to such a network is difficult and expensive [8]. Additionally, it is preferable for this power source

to be “install and forget,” which makes batteries a subpar solution due to the need for periodic replacement or recharging. One suitable solution is the implementation of an energy harvesting device capable of scavenging power from its surroundings.

Although there may be multiple domains from which energy can be harvested, some, like solar and wind energy, possess some drawbacks for this particular application. Explicitly, a bridge can be exposed to a series of overcast or windless days, resulting in insubstantial power generation from these types of power sources. Conversely, since regular bridge use is accompanied by some degree of mechanical vibrations, electrical power generation via electromechanical vibration energy harvesting does not feature this drawback. This type of energy harvesting would ensure that when the bridge is being used, at least some amount of power is being generated by the power supply for the sensor.

There has been a significant amount of research aimed at improving the power output of vibration energy harvesters. The need for this research stems from the fact that conventional vibration energy harvesters are capable of performing well (producing significant power) only at a single frequency [15, 19, 21]. Several techniques have been proposed to address this shortcoming and enable vibration energy harvesting across a wide frequency bandwidth.

For example, research conducted in [23] and [24] demonstrates the effectiveness of generator arrays. These generator arrays are devices in which multiple conventional cantilever beam generators with marginally different natural frequencies are used in a parallel configuration. The natural frequencies of the incorporated generators thereby comprise a frequency bandwidth within which energy capture can occur. Another approach to addressing the single effective operation frequency problem is to enable the harvester’s natural frequency to be tunable. This technique was studied by Zhu et al., [9], Challa et al., [16], and Constantinou et al., [41]; though differing in specifics of implementation, all three research groups proposed tuning methods which relied on a controllable separation between grounded and harvester-mounted magnets to alter the stiffness, and thereby, the natural frequency of their respective harvesters. Peters et al., [14] showed that the stiffness/natural frequency tuning technique can also be accomplished by using piezoelectric actuators. Some research has also been carried out in tuning methods that obviate the need for physical actuation. Cammarano et al., [15] and Bowden et al., [26] propose tuning the harvester’s natural frequency by adjusting the electrical load.

Generator arrays and natural frequency tuning are two major subgroups of solutions for expanding harvesters’ operational bandwidths. However, the literature also features other unique solutions that are not classified by these two methods. For example, Tang and Li’s two-stage vibratory structure employs multimode vibration coupling to achieve a wide frequency band [42].

Despite a large number of emerging techniques being proposed for developing multifrequency energy harvesting, there is a lack of general analytical tools that can be used to drive their development and assess their feasibility and efficacy. Two such tools have been introduced in [43].

The first of the two tools aids in assessing the stability of harvester dynamics given a particular choice of electrical load. Section 6.1 will demonstrate the importance of including this assessment whenever there is consideration of using an active electrical load for the harvester.

The second tool was developed to address the need for a better metric for harvester power generation. Beeby et al., argued that current power metrics are not "ideal" as they "…ignore important factors such as bandwidth," stating that "insufficient data exists in literature to enable this (bandwidth considerations) to be included" [28]. This literature gap was the driving factor for the development of a power metric named the "power harvesting ratio" (PHR) in [43]. This power harvesting ratio assists in the quantification of the amount of power delivered by a harvester to a particular electrical load at any specified frequency component of the excitation. The plot resulting from employing PHR enables prompt identification of frequency components which provide significant contributions to generated power in multifrequency excitation.

The purpose of the present manuscript is to demonstrate the practical applicability and usefulness of these tools via experimental validation using real-world bridge data. As will be shown in Section 4, bridge vibrations can be comprised of multiple substantial frequency components. In such cases, it becomes important to identify and quantify potentially significant power contributions when evaluating a candidate load. The manuscript will show that this identification and quantification process is more easily accomplished using the proposed power harvesting ratio than conventional power-estimating methods, which usually consider only a single, presumably dominant frequency.

The rest of this manuscript is organized as follows: Section 3provides a review of the two analytical tools introduced in [43]. Section 4 describes the process of acquiring and analyzing real-world bridge data; the section also presents the two excitation time series data sets used in the experimentation. Section 5 describes the experimental platform used for validation. This section includes descriptions of a custom-made electromagnetic vibration energy harvester and the electrical loads used for power generation analysis. Section 6 describes the methodology; it describes how to apply the analytical tools described in Section 3 to the dynamics of the experimental harvester, the excitation data, and the employed electrical loads to draw conclusions about harvester stability and average power generation. Section 7 describes and presents the results of the experimentation carried out to validate and assess the accuracy of the claims and techniques presented in Section 6. Section 8 summarizes the findings of the research described in this manuscript. Lastly, Section 9 comprises a short list of individuals and organizations that the authors would like to thank for their valuable assistance.

3. *Review of Stability Assessment and the Power Harvesting Ratio*

This section presents a brief review of the development of the tools used for assessing harvester stability and predicting power generation. A more detailed, step-by-step description of their conception can be found in [43]. It should be noted that the tools were developed based on a model of an electromagnetic vibration energy harvester (referred to simply as "harvester" from this point of the manuscript forward). However, these tools can be applied to any other type of vibration energy harvester (e.g., piezoelectric, electrostatic, etc.,), as long as the model of this device's dynamics is linear.

3.1. Modeling

Figure 30 depicts a typical lumped-parameter schematic model of a harvester. The model consists of a proof mass m connected to an excitation source (e.g. a vibrating bridge) through a linear spring with stiffness k and a linear damper with damping coefficient b.

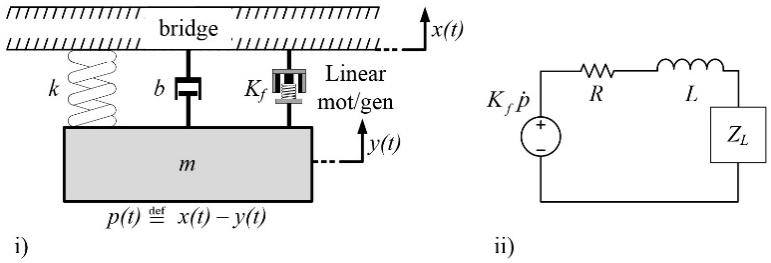

Figure 30: Lumped parameter representation of a vibration energy harvester: i) mechanical components; ii) electrical components

A linear motor with a back EMF constant K_f is placed between the excitation source and the proof mass, in parallel with the damper and spring. In this configuration, the vibrations of the excitation source cause a relative velocity to develop between the proof mass and the excitation source, thereby generating a back EMF (voltage) in the motor coil. This coil has an electrical resistance R and an electrical inductance L. The coil's leads are connected to an electrical load having a generalized electrical impedance Z_L. The dynamics resulting from the interaction of these mechanical and electrical elements are wholly described by the following system of two equations:

$$m\ddot{x} = m(\ddot{x} - \ddot{y}) + b(\dot{x} - \dot{y}) + k(x - y) + K_f i = m\ddot{p} + b\dot{p} + kp + K_f i \tag{44}$$

$$K_f \dot{p} = L\frac{di}{dt} + Ri + v_L, \tag{45}$$

where x is the displacement of the input excitation, y is the displacement of the proof mass, $p \triangleq^{\text{def}} x - y$ is the relative displacement between the input excitation and the proof mass, i is the current running through the motor's coil, and v_L is the voltage across the electrical load.

Modeling approaches similar to the lumped-parameter approach represented by Figure 30 and described by (44) and (45) are commonly used to model harvester dynamics the in literature [15], [26], [39]. In [43], the form of this modeling approach was altered in order to facilitate (a) the stability analysis of the harvester, which is of particular interest when an active load is employed, and (b) power generation estimation.

The harvester's dynamics were cast wholly into the electrical domain. This was done to simplify the analysis of the harvester's load selection on its power generation – in electromagnetic vibration energy harvesting power is ultimately delivered to the electrical domain, and in multi-domain systems load matching must be carried out in the domain to which power is being delivered [30]. In the electrical domain, the harvester dynamics were represented by the Thévenin equivalent circuit shown in Figure 31, in which Z_L is assumed to be a linear complex impedance of some electrical load.

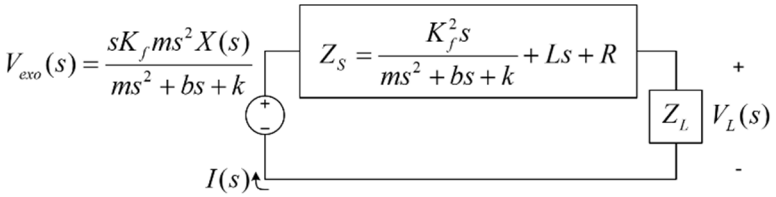

Figure 31: Thévenin equivalent circuit representation of the vibration energy harvester

The Figure 31 Thévenin equivalent circuit serves to facilitate load choice/matching, while simultaneously making the system's input exogenous. Explicitly, in (45) $K_f \dot{p}$ can be construed as the "input voltage source" to the electrical domain. This quantity depends on the back EMF constant and the relative velocity between the input excitation and the proof mass. In this form, since $\dot{p}$ is not independent of the choice of electrical load, assessing the effect of load choice on power generation is difficult; the choice of Z_L affects both the load voltage as well as the input voltage. In contrast, the model form shown in Figure 31 presents the input voltage as being dependent on several internal harvester dynamics properties, but independent of the choice of electrical load – hence, its designation as "exogenous".

Additionally, note that the Thévenin equivalent circuit representing the overall harvester dynamics depicted in Figure 31 are expressed in the s-domain. The circuit is represented in the frequency domain since vibration energy harvesting is cyclic in nature and complex impedances are often used in electrical power analysis. The Laplace transform was chosen in favor of the Fourier transform (which is more popular in literature) because it allows a novel stability analysis and simplifies power generation estimation as described in the following two sub-sections.

3.2. Stability Analysis

Note that the s-domain Thévenin equivalent circuit shown in Figure 31 is dynamically equivalent to the linear, closed-loop feedback system shown in Figure 32. This representation allows conclusions to be drawn about the dynamic behavior of the harvester by using well-established techniques from linear control theory on the system shown in Figure 32. One important aspect to consider is the harvester's stability, especially if the electrical load is active.

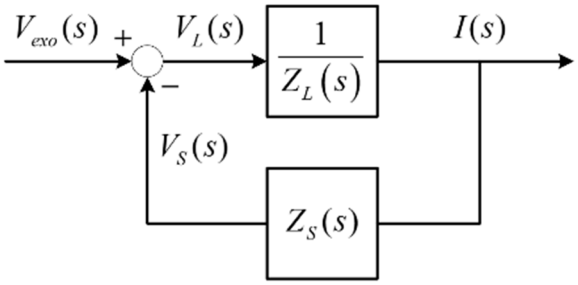

Figure 32: Lumped parameter representation of a vibration energy harvester: i) mechanical components; ii) electrical components

The harvester's stability can be determined by plotting the Nyquist contour of the open-loop transfer function $G_{OL}(s)$ shown in (46) and employing the Nyquist Stability Criterion, shown in (47).

$$G_{OL}(s) = \frac{Z_s(s)}{Z_L(s)} \tag{46}$$

$$P_{CL} = P_{OL} + N_{CW}. \tag{47}$$

The Nyquist Stability Criterion states that the system shown in Figure 32 will have exactly P_{CL} unstable, closed-loop poles, which is equal to the number of the system's unstable, open-loop poles P_{OL}, plus the number of times the Nyquist contour of the open-loop transfer function encircles the critical point $-1 + 0j$ in the clockwise direction N_{CW} (note that a counterclockwise encirclement contributes -1 to N_{CW}). The use and importance of this well-established linear control theory technique will be demonstrated in Section 6.1.

3.3. Power Harvesting Ratio

The PHR developed in [43] was created for the purpose of estimating the power generation (both, the total power, as well as each frequency component's contribution to this total) of a given harvester when it

is excited by multifrequency component excitation. This tool is an equation derived by applying the general expression for average power absorbed by an impedance in an AC circuit given by (48):

$$\overline{\mathbb{P}} = \frac{1}{2}|V||I|\cos(\varphi) \tag{48}$$

to the harvester's Thévenin equivalent circuit in Figure 31. In (48), $\overline{\mathbb{P}}$ is the average power absorbed by the load impedance, $|V|$ is the amplitude of the sinusoidal voltage across this impedance, $|I|$ is the amplitude of the current running through this impedance and φ is the phase between this voltage and this current. The PHR equation, resulting from applying (48) to the circuit in Figure 31 (the in-depth derivation can be found in [18]), is given by:

$$\mathrm{PHR}(\omega) \stackrel{\text{def}}{=} \left.\frac{\overline{\mathbb{P}}(\omega)}{|s^2X(s)|^2}\right|_{s=j\omega} = \frac{1}{2}\left|\frac{Z_L(s)}{|Z_S(s)+Z_L(s)|^2}\right|\left|\frac{K_f ms}{ms^2+bs+k}\right|^2 \cos\left(\measuredangle Z_L(s)\right)\Big|_{s=j\omega} \tag{49}$$

Equation (49) defines the normalized average power generated by the harvester at a frequency ω; the normalization is done with respect to the squared amplitude of the input acceleration's component at that frequency $|s^2X(s)|^2$.

The normalization found in PHR results in the controls-based interpretation of Figure (4) which is useful for determining harvester stability and stability robustness. This normalization also allows the use of (49) in conjunction with a discrete Fourier transform (DFT) of an excitation signal to obtain the harvester's average power generation behavior. Once the DFT of the signal is obtained (ensuring that its units are acceleration squared), it can be simply multiplied by the PHR at the corresponding frequencies to obtain the harvester's total average power generation for that particular excitation. In this manner, the contribution of each individual frequency component to the power generation can be seen. Explicit instructions for how this operation is carried out are presented in Section 6.2.

The form of normalization is important for the correct assessment of harvester efficiency. Since the physical input into the harvester can be construed as $m\ddot{x}(t)$, as can be seen from (44), normalizing PHR with respect to the acceleration amplitude squared yields the quantity of power generated divided by the same quantity of physical input at all frequencies. Thus, in the normalized form shown in (49), the largest PHR value necessarily indicates that the harvester system generates power most efficiently at that particular frequency. If this was not the case and PHR was normalized with any other derivative of x instead of acceleration, the physical input would not stay constant with respect to frequency. For example, if displacement was used, very high frequencies would result in much larger $m\ddot{x}(t)$ inputs into the system.

This could potentially result in a false interpretation that the harvester generates large amounts of power at very high frequencies.

The proposed method for stability analysis and the PHR power estimation technique were both introduced in [43] along with experimental validation using sinusoidal excitation. The purpose of the remainder of the manuscript is to demonstrate how these tools are applied to actual physical bridge data exhibiting multiple frequencies, a harvester employing different electrical loads, and to assess their accuracy when this is done.

4. Excitation Measurement and Characterization

In previous work, an idealized input spectrum was used as input to the energy harvester. One of the major goals of this work is to show that the PHR method for power estimation is effective when the input excitation is more realistic. The response of a bridge, described below, to a single vehicle excitation was acquired. To understand the frequency content of the bridge's response, modal impact testing was conducted and the natural frequencies and mode shapes of the bridge were identified. The relative contribution of each mode to the bridge's response to the vehicle excitation was identified in order to demonstrate the need for energy harvesting at multiple frequencies. The measured response of the bridge was then used as input excitation for the experimental energy harvester described in Section 5.1. This input helped evaluate the accuracy of PHR in estimating power generation for realistic bridge vibrations and to confirm theoretical predictions about harvester stability.

The bridge selected for testing was the Bob Sheehan Memorial Bridge in Nashville, Tennessee. It's a two-lane, steel truss bridge spanning the Stones River in Nashville, TN. This bridge was formerly open to traffic, but is now part of the Stones River Greenway trail system. This bridge provided a unique opportunity to collect both the free response (via impact testing) and forced response (via vehicle excitation) data. Permission from the local authorities was obtained to conduct all tests. A photograph of the bridge is shown in Figure 33 (A).

Modal impact testing was conducted to identify the natural frequencies and mode shapes of the bridge. Figure 33 (B) shows the grid of twenty-one impact points used during the testing and the locations of the three accelerometers (two PCB 393A03, and one Colibrys SF1500S.A) used to measure the response of the bridge. A PCB 086D50 modal sledge hammer was used to excite the bridge, and data was acquired using a National Instruments 9234 data acquisition card and custom software.

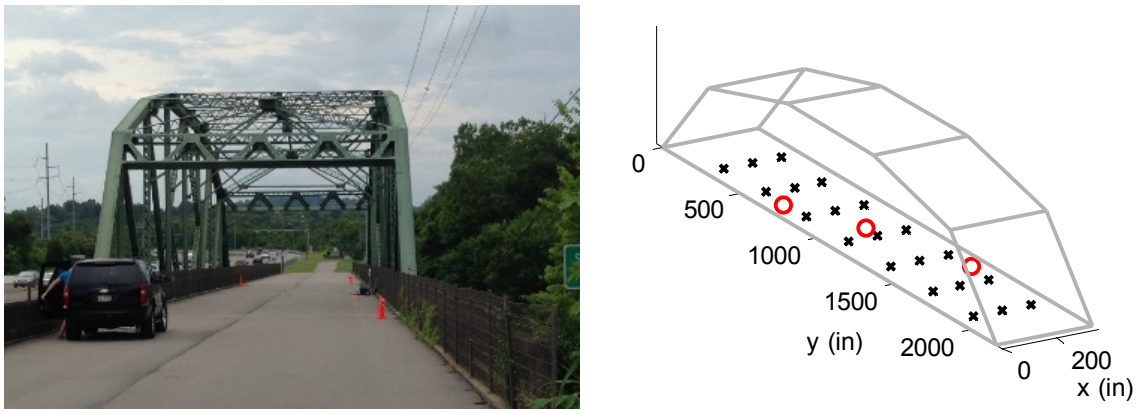

Figure 33: (A) Bridge used for experimental testing; (B) Schematic indicating impact points (**x**) and sensor locations (**o**) used during impact testing.

The response of the bridge was measured for five impacts per point and the average frequency response functions for each sensor-impact location combination were calculated. The complex mode indicator function (CMIF) [44] was used to synthesize data from all three sensors to estimate the natural frequencies of the bridge. The relative amplitudes of the imaginary part of the frequency response functions (FRFs) at each estimated natural frequency were plotted to visualize the mode shapes. Finally, the modal assurance criterion (MAC) [36] was used to assess the linear independence of the identified modes. Figure 34 shows the first 9 mode shapes determined from impact testing.

Several peaks below 3 Hz were present in the CMIF plot, but MAC calculations indicated that the corresponding modes were not linearly independent. Therefore, the mode at 3.17 Hz was selected as representative and the others were omitted. Figure 35 shows a plot of the MAC values between the nine modes shown in Figure 34. Values close to one indicate that the modes are independent. This plot indicates that the nine modes identified in Figure 5 show a high degree of linear independence.

The response of the bridge to a single vehicle excitation was acquired for use in the analysis of the energy harvester. A 2007 Chevrolet Tahoe (total weight including passengers ≈ 5900 lbs (2680 kg)) was driven across the bridge at a near constant speed of 20 miles per hour (32.2 kph). The response of the bridge was measured at the accelerometer located at the bridge's midpoint Figure 36 and Figure 37 show two time histories that are representative of the data sets collected; the figures also show the DFT of each data set. Several peaks are present in both data sets. For example, both data sets show strong contributions in the response from modes near 9 Hz and 11.8 Hz. In addition, peaks near 3.1 Hz and 6.3 Hz correlate well with modes identified from impact testing. These results demonstrate the opportunity to harvest energy from the bridge at multiple frequencies. In Section 6.2, the PHR analysis tool will be used to quantify the amount of power generated at each of these frequencies given the harvester's dynamics and a specified electrical load.

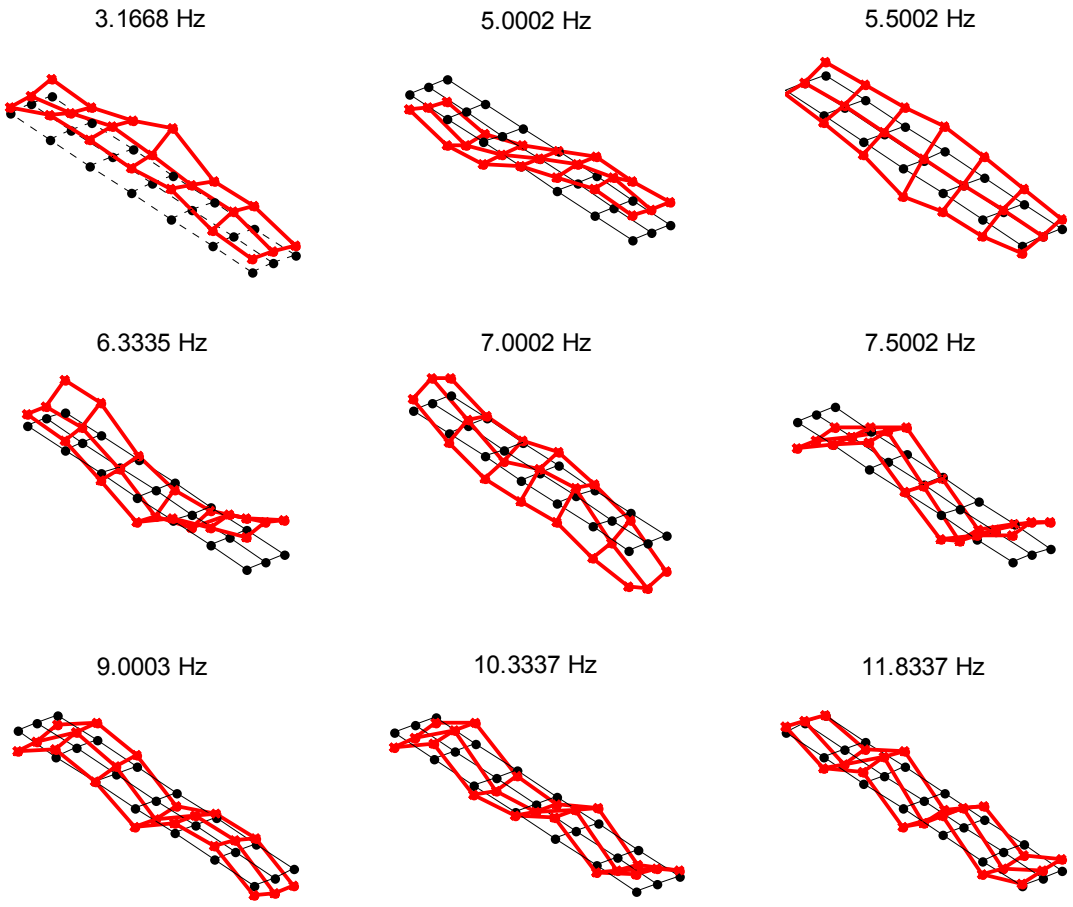

Figure 34: The first 9 modes and their respective shapes of the Bob Sheehan Memorial Bridge

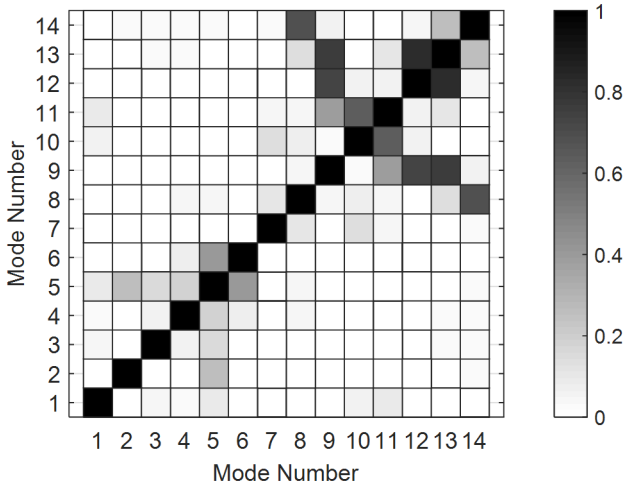

Figure 35: Modal assurance criterion (MAC) values indicating the linear independence of the nine modes shown in Figure 34 (Mode Number 1-9).

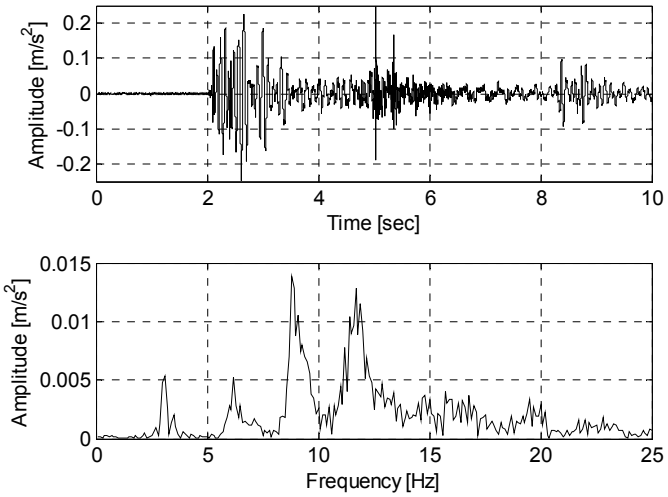

Figure 36: Bridge acceleration time series data set A (top) and its DFT (bottom)

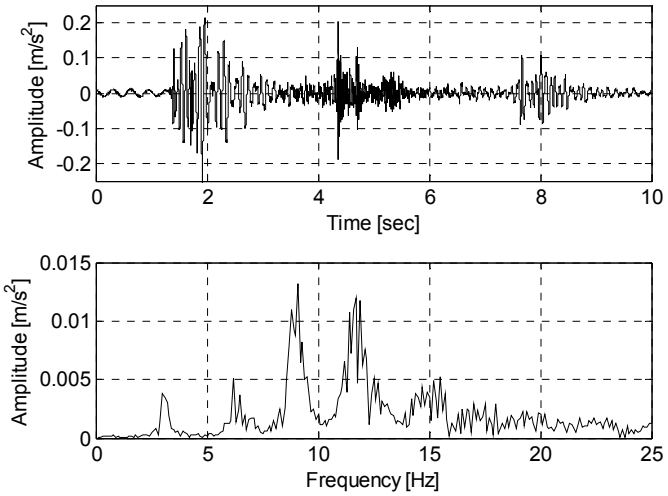

Figure 37: Bridge acceleration time series data set B (top) and its DFT (bottom)

5. *Experimental Setup*

5.1. Description of Harvester

To demonstrate how the stability and PHR tools discussed in Section 3 are implemented for different electrical loads, the bridge acceleration data introduced in the previous section was replayed on the experimental setup shown in Figure 38.

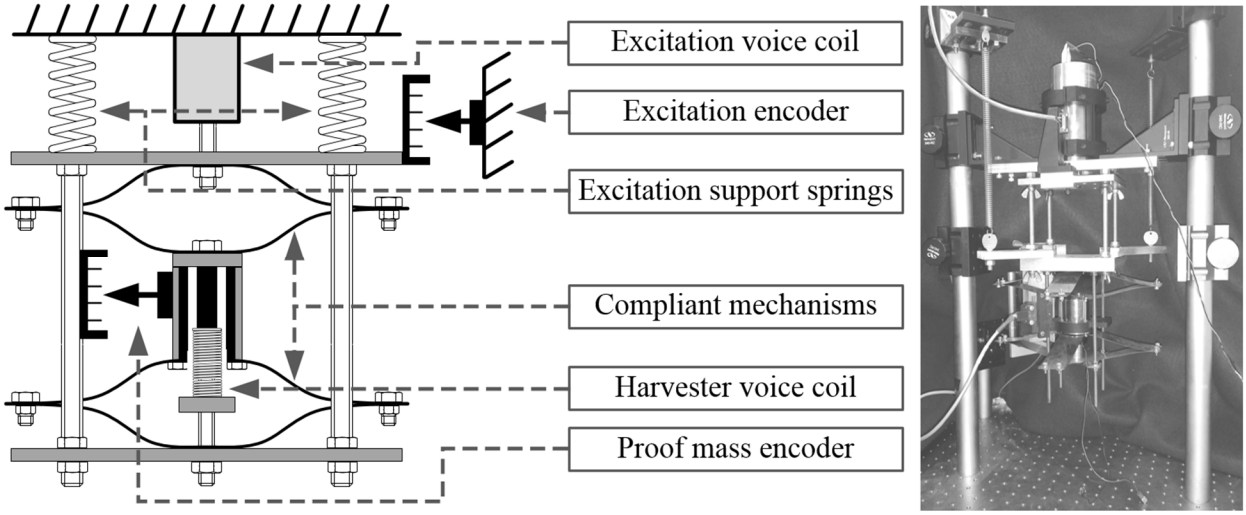

Figure 38: Schematic and photograph of the experimental electromagnetic vibration energy harvester

The setup can be viewed as two stages. Referring to Figure 38, the first stage is comprised of the excitation voice coil, excitation encoder, and the excitation support springs. The voice coil's function is to emulate bridge vibrations, exciting the 2nd stage – the harvester – which generates electrical power from this mechanical excitation. The grounded excitation springs support the harvester, thereby reducing the static load on the excitation voice coil; this allows the coil to more easily shake the 2nd stage. The encoder is used in closed-loop control to ensure the intended excitation signal is being reproduced accurately by the voice coil.

The 2nd stage consists of the compliant mechanisms, harvester voice coil, and proof mass encoder. The compliant mechanisms serve as a restorative spring element that enables relative oscillatory motion between the harvester voice coil's housing and its core. The housing contains permanent magnets and the core holds the voice coil's windings; the relative motion between these components induces current and enables generation of power. The compliant mechanisms were chosen in favor of conventional extension springs as they also serve to enforce good axial alignment between the core and the housing, which increases the harvester's efficiency by minimizing power generation losses due to parasitic friction. The proof mass encoder measures the relative motion between the harvester voice coil's housing and core. This measurement was used to help calculate the harvester's $m, b,$ and k coefficients for system modeling and control.

There are several setup components not shown in the schematic and photograph of Figure 38 that were used during experimentation. Two servo amplifiers were used to power the excitation and harvester voice coils. The latter was powered only when an active electrical load was to be employed. The current running through the harvester's windings was measured with an inductive current probe. The voltage across the

windings' leads and the voltages from the encoder signals were measured with a data acquisition card. This card was used in conjunction with Matlab Simulink Real-time R2014a for all data acquisition and to provide control signals to the servo amplifiers powering the voice coils.

The experimental setup's pertinent components are listed in Table 7; the key parameters governing those harvester dynamics that are independent of the electrical load choice are listed in Table 8.

Table 7: Experimental Setup Components

Component	Specifics
Excitation voice coil	BEI LAH28-52-000A
Harvester voice coil	BEI LA17-28-000A
Excitation and proof mass encoders	U.S. Dig. EM1, 2000 cts/in strips
Excitation support springs	Jones Spring Co. 1 lbs/in ext. rate
Compliant mechanisms	Laser-cut 1095 spring steel
Inductive current probe	Agilent 1146A
Servo amplifiers	Kepco BOP 36-6
Data acquisition card	NI PCI-6259

Table 8: Experimental Harvester Parameters

Parameter	Value
m	0.697 kg
b	6.925 N/(m/s)
k	1665 N/m
K_f	17.8 N/A or V/(m/s)
L	0.0031 H
R	7 Ω

5.2. Description of the Electrical Loads

Four passive and two active electrical loads were used to demonstrate the use of the tools introduced in Section 3; they are shown in Table 9.

The 52.7 Ω load was chosen based on conventional harvester tuning practices. It is the electrical load which results in the greatest amount of power being delivered to the load by the harvester when the latter is excited at its natural frequency. This purely resistive load R_L is calculated according to

$$R_L = R + K_f^2/b \tag{50}$$

using the parameter values from Table 8. The derivation of (50) and the reason for why it does not contain a capacitive element as would be expected are presented on page 7 of [43].

Table 9: Electrical Loads Used During Experimentation

Load Type	Load
Passive, resistive	52.7 Ω
Passive, resistive	23.6 Ω
Passive, resistive and capacitive	52.7 Ω and 240 μF
Passive, resistive and capacitive	23.6 Ω and 240 μF
Active	MPTT
Active	ACTIVE

The 23.6 Ω load was chosen by restricting $Z_L(s)$ in (49) to be purely resistive, assuming the input excitation is bridge acceleration time series data set A shown in Figure 36, and numerically determining the purely resistive load which results in the most generated power for this particular excitation.

The 240 μF capacitor that was added to both of these resistive loads was not meant to increase power generation. It was included to evaluate the accuracy of PHR when the employed electrical load has a frequency dependent component (i.e., is not purely resistive). Its value was chosen to be large enough to result in pronouncedly different behavior of the harvester's dynamics and power generation as compared to when the resistive loads were used by themselves.

One of the two tested active loads is the load prescribed by the maximum power transfer theorem (MPTT). According to this theorem, the maximum amount of power is transferred from a power source to a load when that load's impedance is equal to the complex conjugate of the source impedance. Given the harvester's source impedance shown in Figure 31, the load which satisfies MPTT is given by

$$Z_{MPTT}(s) = Z_S^*(s) = -\frac{K_f^2 s}{ms^2 - bs + k} - Ls + R \tag{51}$$

The second active load used was chosen based on two requirements: that it be active and that it result in stable harvester behavior. Denoted as "ACTIVE" in Table 9, its form is

$$Z_{ACTIVE}(s) = \frac{s(s + z_1)^2}{\alpha(ms^2 + bs + k)}. \tag{52}$$

The location of the double zero and the factor scaling the denominator were determined by substituting (52) for $Z_L(s)$ into the PHR equation (49), and numerically solving for which values of z_1 and α yielded the greatest average power generation subject to the excitation. The excitation used in obtaining the solution was the bridge acceleration time series data set A shown in Figure 36 – the same excitation used to optimize the 23.6 Ω passive load. The values found to yield the greatest power were $z_1 = 60$ and $\alpha = 20$.

6. *Methodology*

The following section illustrates how the two analytical tools introduced in Section 3 – the method for assessing harvester stability using the Nyquist stability criterion, and the technique for estimating power generation with PHR – are used in practice.

6.1. Stability Assessment of Active Loads

Before the PHR method can be used to estimate power generation values for the loads described in the previous section, it's necessary to ensure that these loads do not result in unstable harvester behavior. As passive loads are innately incapable of inputting net positive power to the harvester, they cannot cause the harvester dynamics to be unstable. However, it's necessary to analyze the two active loads using the method described in Section 3.2 before predicting their power generation behaviors using PHR. As will be shown below, attempting to use $Z_{MPTT}(s)$ causes the harvester dynamics to become unstable, whereas $Z_{ACTIVE}(s)$ will be shown to be a serviceable active electrical load.

6.1.1. Electrical Load Prescribed by the Maximum Power Transfer Theorem

When the load dictated by MPTT shown in (51) and the sourced impedance of the harvester shown in Figure 31 are substituted into the resulting equation is

$$G_{OL}(s) = \frac{A_5 s^5 + A_4 s^4 + A_3 s^3 + A_2 s^2 + A_1 s + A_0}{B_5 s^5 + B_4 s^4 + B_3 s^3 + B_2 s^2 + B_1 s + B_0}, \tag{53}$$

where $A_5 = Lm^2$, $A_4 = m^2 R$, $A_3 = -b^2 L + \mathrm{K_f^2} m + 2kLm$, $A_2 = -b\mathrm{K_f^2} - b^2 R + 2kmR$, $A_1 = k\mathrm{K_f^2} + k^2 L$, $A_0 = k^2 R$, $B_5 = -Lm^2$, $B_4 = m^2 R$, $B_3 = b^2 L - \mathrm{K_f^2} m - 2kLm$, $B_2 = -b\mathrm{K_f^2} - b^2 R + 2kmR$, $B_1 = -k\mathrm{K_f^2} - k^2 L$, and $B_0 = k^2 R$. Substituting the harvester parameters values from Table 8 into (53) results in the open-loop transfer function having three unstable poles, i.e., $P_{OL} = 3$ in (47). Thus if the harvester is to be closed-loop stable, the Nyquist contour of (53), shown in Figure 39 three or more times in the counterclockwise direction, i.e., $N_{CW} \leq -3$.

Note that only half of the Nyquist contour is shown (it is symmetric about the real-axis) and the entire contour actually lies right on top of the unit circle drawn using dashed line style on the plot. Only half of the contour is shown and this half is displaced off of the unit circle and shifted closer to the origin solely for cosmetic purposes; this was done to facilitate visual inspection of the plot.

This Nyquist contour reveals that even if a gain was used to increase the overall magnitude of (53)(51) , the contour shown in Figure 39 would only provide at most one counterclockwise encirclement of the critical point resulting in $2 \leq P_{CL} \leq 3$.

This means that the active load dictated by MPTT shown in (51) would cause the harvester's closed-loop transfer function to possess between two and three unstable poles, necessarily implying unstable, and therefore, non-implementable harvester behavior.

In fact, the resulting unstable behavior when $Z_{MPTT}(s)$ is used as the electrical load applies to any harvester of the form described by the lumped-parameter model shown in Figure 30. The closed-loop transfer function of the harvester (i.e., the closed-loop transfer function of the system shown in Figure 32) is $G_{CL}(s) = I(s)/V_{exo}(s)$:

$$G_{CL}(s) = \frac{A_5 s^5 + A_4 s^4 + A_3 s^3 + A_2 s^2 + A_1 s + A_0}{2m^2 R s^4 + 2(-b\mathrm{Kf}^2 - b^2 R + 2kmR)s^2 + 2k^2 R}, \tag{54}$$

where $A_5 = -Lm^2$, $A_4 = m^2 R$, $A_3 = b^2 L - \mathrm{Kf}^2 m - 2kLm$, $A_2 = -b\mathrm{Kf}^2 - b^2 R + 2kmR$, $A_1 = -k\mathrm{Kf}^2 - k^2 L$, and $A_0 = k^2 R$. Noting that the values of coefficients m, b, k, R, L, and K_f have to remain strictly positive due to the inherent nature of the harvester's parameters they represent, the Routh-Hurwitz Stability Criterion can be applied to (54) to conclude that $G_{CL}(s)$ will always have unstable closed-loop poles.

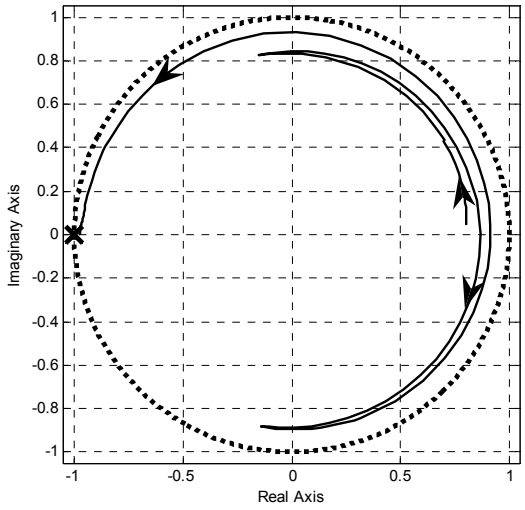

Figure 39: Nyquist plot of $G_{OL}(s)$ for $Z_L(s) = Z_{MPTT}(s)$

Put differently, it is impossible to actively implement the maximum power transfer theorem-dictated load across a frequency range for a harvester described by the traditional lumped-parameter representation

shown in Figure 30 without producing unstable harvester dynamics. Note that this means that (51) cannot be implemented for $s = j\omega$ where ω varies. It is, however, possible to pick a single particular frequency, and implement MPTT at that frequency. This can even be achieved solely through the use of correctly valued passive components.

It's important to consider the implications of the previous paragraph. Some research has claimed that achieving maximum power delivery to the load in a certain frequency bandwidth is possible [27]; however this research did not consider harvester stability. In order for the electrical load to be able to autonomously adapt to frequency changes or to harvest maximum power when multiple frequency components are present in the excitation, (51) would have to be actively enforced. Since this would result in unstable harvester behavior, practically achieving maximum power delivery to the load across all frequencies is impossible. Consequently, MPTT can only be achieved at a single excitation frequency at a time by substituting that particular frequency into (51) and using the resulting passive load. Therefore, even though a MPTT-dictated load can theoretically be realized at any chosen frequency, this is of little value when it comes to practical implementation; the load tuning could not be autonomous and it would be impossible to extract maximum possible power (determined by MPTT) from excitation comprised of multiple frequency components.

6.1.2. Trial Active Electrical Load

As mentioned in Section 5.2, the ACTIVE electrical load was chosen somewhat arbitrarily. Although the constants z_1 and α in (52) were tuned to increase power generation for the given excitation, the chief purpose of including $Z_{ACTIVE}(s)$ in the experimental testing was to verify that PHR can accurately predict power generation for active loads.

Prior to assessing whether this is the case, since $Z_{ACTIVE}(s)$ is an active load, its effect on harvester stability needed to be examined using the same procedure that was used with $Z_{MPTT}(s)$ in the previous section.

Substituting $Z_{ACTIVE}(s)$ from (52) and $Z_s(s)$ from Figure 31 into $G_{OL}(s)$ from (46) yields the following open-loop transfer function:

$$G_{OL}(s) = \frac{A_3 s^3 + A_2 s^2 + A_1 s + A_0}{s^3 + 2z_1 s^2 + z_1^2 s} \tag{55}$$

where $A_3 = \alpha Lm, A_2 = \alpha(Rm + bL), A_1 = \alpha\left(bR + kL + K_f^2\right), A_0 = \alpha kR$. Substituting $\alpha = 20, z_1 = 60$, and the harvester parameters from Table 8 into (55) yields 0 unstable open-loop poles (i.e., $P_{OL} = 0$ in (47)) and the Nyquist contour shown in Figure 40.

The rest of the Figure 40 Nyquist contour extends into the right-half plane, making $N_{CW} = 0$, and consequently $P_{CL} = 0$, in the Nyquist Stability Criterion shown in (47).

This stability assessment confirms that using a servo amplifier to emulate the active load described by $Z_{ACTIVE}(s)$ in (52) would not result in unstable harvester dynamics; this allows $Z_{ACTIVE}(s)$ to be used to assess the accuracy of the PHR power estimation method.

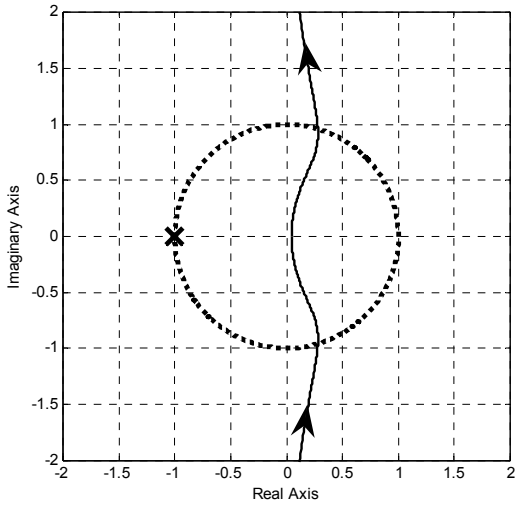

Figure 40: Nyquist plot of $G_{OL}(s)$ for $Z_L(s) = Z_{ACTIVE}(s)$

6.2. Average Power Generation Estimation Using PHR

Figures 41 and 42 show the PHR curves for the loads in Table 9 and the DFT of one of the excitation time series used for experimental validation.

The PHR curves are simply plots of (49) with the loads from Table 9 substituted in. They indicate the amount of average power the experimental harvester would deliver to the specified electrical load per unit of acceleration squared as a function of frequency. Note that the DFT plot shown in both figures features units of acceleration squared. This unit choice allows a value on the PHR curve of a given load at a particular frequency, $\text{PHR}(\omega_i)$, to be multiplied by the amplitude of acceleration squared value appearing on the DFT plot at the same frequency, $a^2(\omega_i)$, to obtain the average power delivered to the load at that particular frequency $\overline{\mathbb{P}}(\omega_i)$:

$$\overline{\mathbb{P}}(\omega_i) = \text{PHR}(\omega_i) \cdot a^2(\omega_i). \tag{56}$$

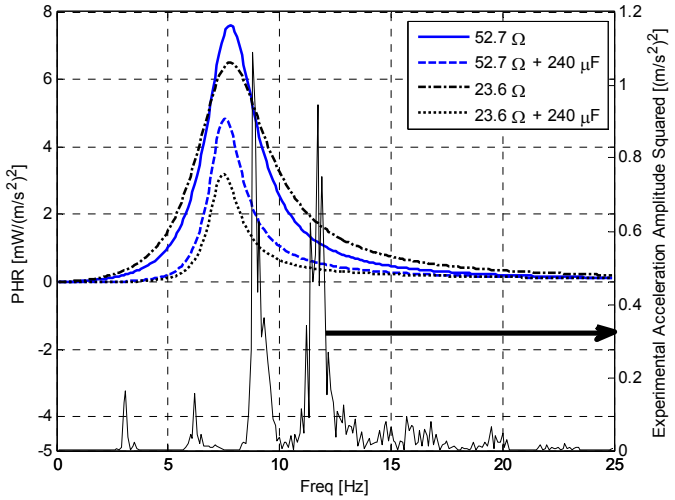

Figure 41: DFT of the squared amplitude of the acceleration of the harvester's excitation and calculated power harvesting ratios for used *passive* electrical loads

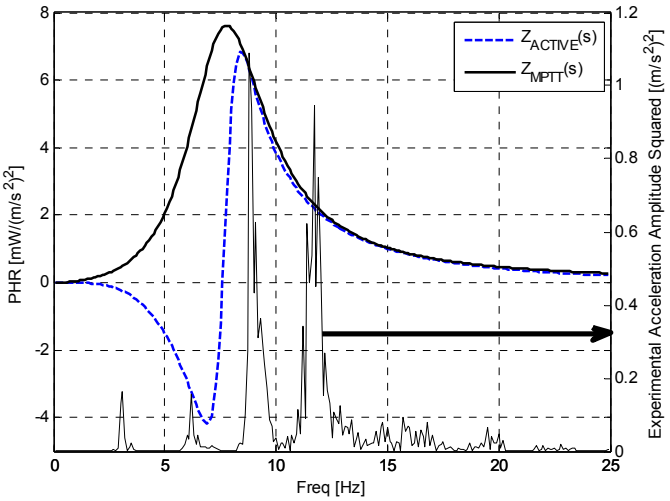

Figure 42: DFT of the squared amplitude of the acceleration of the harvester's excitation and calculated power harvesting ratios for used *active* electrical loads

Figure 43 shows the result of carrying out the (56) operation for all frequency values in the 0 to 25 Hz frequency range using the PHR curve of $Z(s)_{ACTIVE}$ and the DFT plot, both of which are shown in Figure 42. Note that Figure 43 implies that using $Z(s)_{ACTIVE}$ as the electrical load when the harvester is subjected to the given excitation will actually result in negative average power generation at approximately 6 Hz – meaning power is actually transferred from the load to the harvester at that frequency. However, this small power drain is outweighed by the positive power generation values appearing at about 9 and 12 Hz.

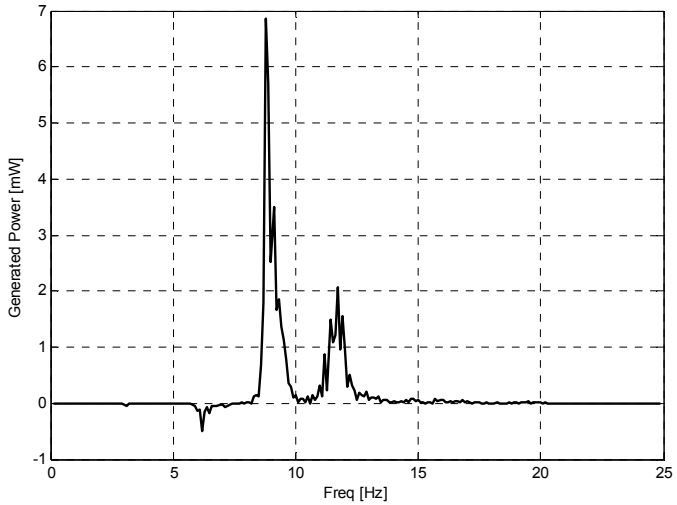

Figure 43: Average power generated by the harvester as a function of frequency for $Z_{ACTIVE}(s)$

By summing the values plotted in Figure 43, the prediction for the overall average power generation (i.e., the average power delivered by the particular harvester to the chosen electrical load at the excitation described by the given DFT) is obtained. In equation form, this summation is represented by

$$\overline{\mathbb{P}}_{\text{tot}} = \sum_{i=1}^{N} \overline{\mathbb{P}}(\omega_i), \tag{57}$$

where $\overline{\mathbb{P}}_{\text{tot}}$ is the total average power predicted to be delivered by the harvester to the electrical load by PHR from all frequency components ω_i through ω_N in the excitation.

The PHR method's strength lies in the ease of its application and the clarity of its results. The effect of using a different electrical load or having a different expected excitation can be quickly assessed by substituting the desired load's impedance into (49) to obtain a new PHR curve or calculating the DFT for the new excitation. Results akin to Figure 43 then allow the individual contribution of distinct frequency components to be easily identified.

However, the PHR method should be applied with care – it should never be used before ensuring that the electrical load for which power generation is being estimated can actually be employed. For example, Figure 43 can be obtained for $Z_{MPTT}(s)$ as well. In fact, the $Z_{MPTT}(s)$ PHR contour, purposefully included in Figure 42, shows that if $Z_{MPTT}(s)$ was implementable as the electrical load of the harvester, its power generation potential either matches or exceeds that of $Z_{ACTIVE}(s)$ at every frequency. Theoretically, this is not surprising since $Z_{MPTT}(s)$ is based on the maximum power transfer theorem. However, as was shown in Section 6.1.1, it is impossible to use $Z_{MPTT}(s)$ as the harvester's electrical load since it would result in unstable harvester dynamics. Since $Z_{MPTT}(s)$ is not implementable as the harvester's electrical load, its

superior predicted average power generation is inconsequential from a practical point of view. It does however serve to identify an upper bound in designing a load that is stable. Figure 13 essentially shows that $Z(s)_{ACTIVE}$ "has it where it counts" for this particular excitation.

7. Experimental Results

The following section presents experimental data as support for the predictions concerning the estimated power generation and stability of harvester dynamics made in the previous section.

To assess the accuracy of using (56) and (57) to estimate harvester power generation, the amplified bridge acceleration time-series data sets A and B shown in Figure 36 and Figure 37 were used as excitation for the harvester described in Section 5.1. The excitation's amplitude was scaled up by a factor of 75 in order to make the excitation reproducible and repeatable on the experimental setup. Since the data sets were amplified by the same factor at each time step, the DFT shape of the bridge's oscillatory response remained the same.

Each of the electrical loads shown in Table 9 were connected across the harvester's leads and the experimentally obtained average power delivered to each load was calculated according to (58):

$$\overline{\mathbb{P}}_{\text{tot exp}} = \frac{\sum_{i=1}^{M} V_{L_i} \cdot I_i}{M}, \tag{58}$$

where V_{L_i} and I_i are the load voltage across, and current flowing through, the harvester leads, respectively, at the time the i^{th} sample was collected by the data acquisition card, and M is the total number of such samples collected.

Each load was tested using both of the acceleration time-series data sets five times. The theoretical total average power delivery to the load was recalculated for each experimental run using the DFT calculated from the measured excitation. This was done to account for any small differences existing between the actual and desired excitation displacements.

The experimentally measured average power generation was taken as the true value, and the percent that the PHR-predicted value deviated (i.e., percent error) from the experimentally measured value was calculated using the standard formula:

$$\text{Error} = 100 \cdot \frac{\overline{\mathbb{P}}_{\text{tot}} - \overline{\mathbb{P}}_{\text{tot exp}}}{\overline{\mathbb{P}}_{\text{tot exp}}}. \tag{59}$$

Figure 44 depicts the PHR-predicted average power generation values plotted against their resultant error quantities for all of the experimental runs that used the amplified acceleration time series data set A from Figure 36 as the excitation. Figure 45 plots the corresponding results for experimental runs that used the amplified acceleration time series data set B from Figure 37.

Note that one of the loads used during experimentation – the 52.7 Ω resistance – was implemented/tested in two different ways. The data points labeled "52.7 Ω Physical" represent the experimental data set obtained from attaching a physical resistance of 52.7 Ω across the harvester leads. The points labeled "52.7 Ω Emulated" are the experimental results from attaching servo amplifier leads to the leads of the harvester, and emulating the behavior of a 52.7 Ω resistor. This was done to ensure the accuracy of using a servoamp to emulate load behavior. Use of the servoamp is necessary to implement $Z_{MPTT}(s)$ and $Z_{ACTIVE}(s)$.

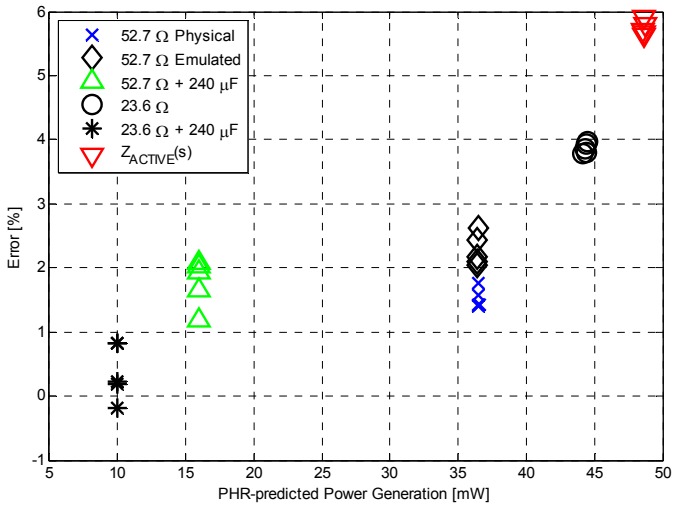

Figure 44: Average power generation predicted by PHR and its percentage difference from experimentally measured power generation for excitation based on data set A

Overall, the experimental results show that the PHR method accurately predicts average power delivered by the harvester to the load, as no experimental run exhibited an error exceeding ± 6 %. The plots also show good repeatability of experimental results. Testing using the same experimental conditions (i.e., reference excitation and chosen load) yielded results that were typically within ± 1 %; the data sets obtained using the physical and the emulated 52.7 Ω loads also exhibit this close grouping.

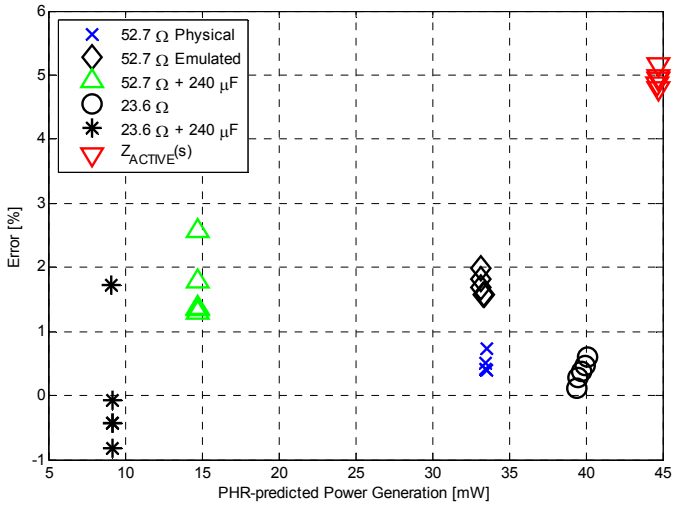

Figure 45: Average power generation predicted by PHR and its percentage difference from experimentally measured power generation for excitation based on data set B

Note that Figure 44 and Figure 45 do not feature experimental results for the $Z_{MPTT}(s)$ load. This load was pronounced theoretically not implementable in Section 6.1.1, as it was predicted to cause the harvester dynamics to become unstable during its use. In order to experimentally validate this claim, the MPTT-dictated load described by (51) was emulated using a servo amplifier. To prevent damage to the harvester, voltage was limited so that the housing suspended by the compliant mechanisms would not violently slam into the rest of the experimental setup. Figure 46 shows the theoretical and experimental load voltage responses to the harvester being excited by the experimental version of bridge acceleration time series data set A.

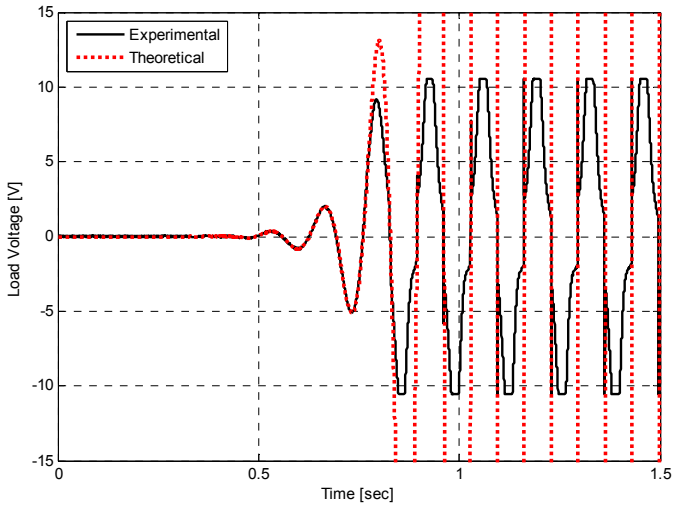

Figure 46: Load voltage response to excitation when Z_L is chosen according to MPTT

The theoretical load voltage is defined as the voltage which would theoretically develop across the harvester leads in response to the excitation if the electrical load behaved as described in (51). The experimental load voltage was measured using the data acquisition card. Note that the theoretical load voltage grows in magnitude without bound, as expected from an unstable system. The experimental load voltage matches the theoretical load voltage whenever it can/when it is not clipped by the servo amplifier voltage limits set to prevent damage to the experimental setup.

A final key observation should be made concerning the experimental results depicted in Figure 44. Recall that 23.6 Ω is the "optimized" purely resistive load; it is the resistive load that results in the largest amount of power being transferred to it by the harvester when the excitation is the acceleration time series data set A (or its amplified version used during experimentation). $Z_{ACTIVE}(s)$, conversely, is an active load which is tuned for greater power generation. The load $Z_{ACTIVE}(s)$ outperforms the 23.6 Ω load in expected average power generation. This superior performance is reflected in the experimentally measured average generated power, and is not due to the slightly larger error on $Z_{ACTIVE}(s)$ PHR-predicted values. The five experimental runs using the 23.6 Ω load resulted in an average of 42.7 mW being delivered to the load, while the five runs using $Z_{ACTIVE}(s)$ resulted in an average of 46 mW being delivered. This increase of approximately 8% in power delivered to the load shows that active electrical loads are capable of achieving better performance, with respect to average power generation, than their passive, optimized counterparts.

8. Conclusions

The principal purpose of the research presented in this work is the practical application of analytical tools introduced in [18].

A description of how to collect and analyze real world physical bridge data in order to use it as predicted harvester excitation for estimating power generation was presented. The presented technique included a way to correctly identify true, linearly independent bridge modes. It was also shown that when a bridge is excited by a vehicle traveling over it, it exhibits several significant frequency components located at these modes. The multifrequency nature of this forced bridge excitation provides strong motivation for the development of the aforementioned analytical tools.

An included methodology section detailed the procedure of assessing harvester stability based on the interplay between the harvester and electrical load dynamics. The ability of this procedure to predict instability was empirically demonstrated by attempting to implement the active electrical load prescribed by the maximum power transfer theorem on the experimental harvester.

The experimental platform was also used to assess the accuracy of the proposed power harvesting ratio technique for estimating average harvester power generation for excitations based on the collected real bridge vibration data. The experimental results indicate that PHR is capable of providing accurate and

repeatable estimates of the average power delivered to a particular electrical load. The technique yielded estimates that never exhibited more than 6% deviation from actual (i.e., experimentally measured) delivered power values; the testing included both passive and active loads.

The use of real world bridge vibration data to validate: 1) the harvester's stability assessment tool, and 2) PHR, serves to show that both of these analytical tools are applicable and practical. The accuracy and ease of use make PHR both a good power generation metric, as well as a valuable design tool for load selection and tuning. This is especially true in cases where excitation is comprised of several significant frequency components.

Finally, it was shown experimentally that a harvester is capable of delivering more power to an active load than it is capable of delivering to an optimized passive load. This suggests that formal electrical load optimization, which can be guided by the analytical tools discussed in this manuscript, may be used to enhance power generation of vibration energy harvesters subjected to multifrequency excitation.

9. Acknowledgements

The authors would like to thank the National Science Foundation (Grant #1035627) for providing financial support that made the presented research possible. The authors also extend a special thanks to Wayne Seger of the Tennessee Department of Transportaiton, Bilie Davis, Mark Macy, and Jeff Campbell of Metro Public Works, and Mark Bradfield of the Metropolitan Board of Parks and Recreation; these individuals were all kind enough to volunteer their time and assistance for the acquisition of a sizeable amount of bridge vibration data, including that which was presented in this paper. Lastly, the author would like to thank Detective Mike Hotz of the Metropolitan Nashville Police Department.

APPENDIX C: FUTURE JOURNAL PAPER

Analysis and Optimization of Electromagnetic Vibration Energy Harvesters Using the Power Harvesting Ratio Performance Metric

Alexander V. Pedchenko, Janette J. Meyer, and Eric J. Barth

Vanderbilt University
Nashville, TN

Article in preparation for publication in IEEE/ASME Transactions on Mechatronics

1. Validation of the Power Harvesting Ratio on Typical Bridge Vibration Data

In Section 0-7 on p. 74, the accuracy of the PHR technique in estimating average power generation was validated using physical bridge vibration data. This data was collected in a highly controlled fashion – the chosen bridge had no traffic other than that which was dictated by the researchers. A single vehicle traveling at a constant, known speed was used to induce the recorded bridge vibrations. Though this type of testing has the advantage of being highly repeatable and enabled the researchers to study the effects of a vehicle's speed on the bridge's vibratory response, it has the drawback of being not very representative of more typical traffic conditions on bridges. In contrast, this chapter describes the measurement and use of bridge vibration data during more frequently encountered traffic conditions.

A PCB 393A03 accelerometer interfaced with a National Instruments 9234 data acquisition card and custom software was used to record acceleration data shown as Datasets 1-7 in Figures 47 and 48. The data was collected off of the I-40/I-65 Broadway overpass in Nashville, Tennessee (36°09'20.9" N 86°47'21.4" W) at 16:20 on October 22nd, 2015.

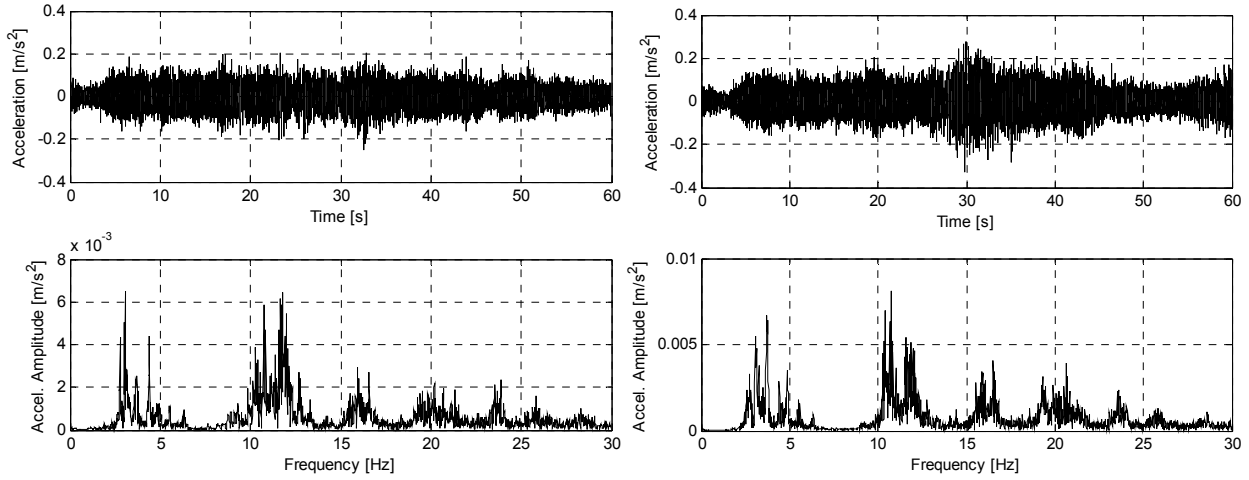

Dataset 1 Dataset 2

Figure 47: Bridge acceleration datasets taken when bridge was being excited by a high volume of moving traffic

Datasets 1 and 2, displayed above, show two one minute long acceleration time-series (and their respective discrete Fourier transforms (DFTs)) taken while the traffic light located at the end of the overpass allowed non-stop traffic flow. Datasets 3-7, shown in Figure 48, are also time series acceleration datasets with their respective DFTs. These datasets were recorded over a span of five minutes – this time interval was intentionally chosen in order to include three complete traffic light cycles along the overpass. These datasets are representative of traffic-induced vibrations occuring on the overpass during rush hour.

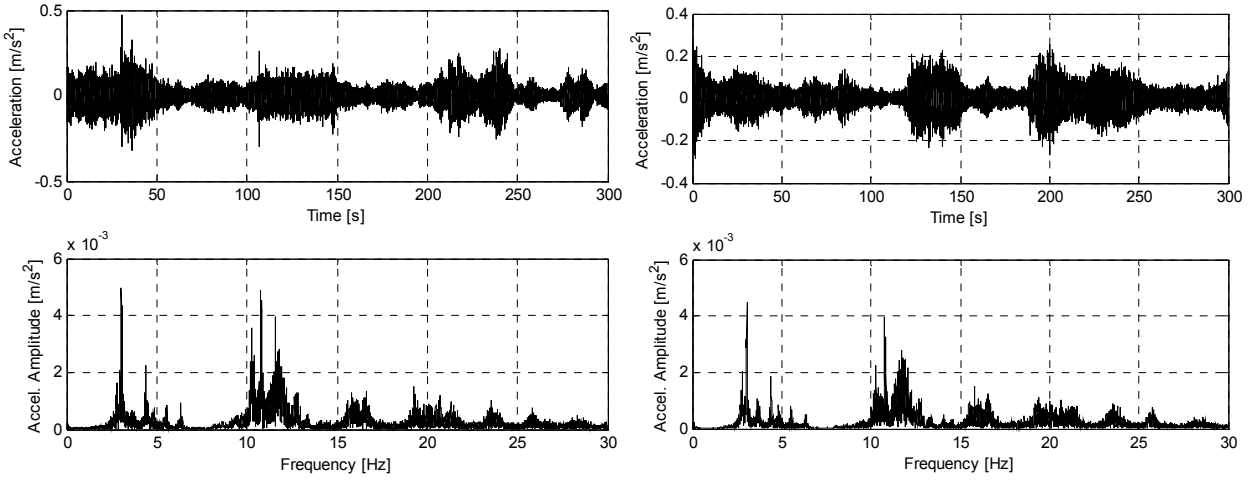

Dataset 3 Dataset 4

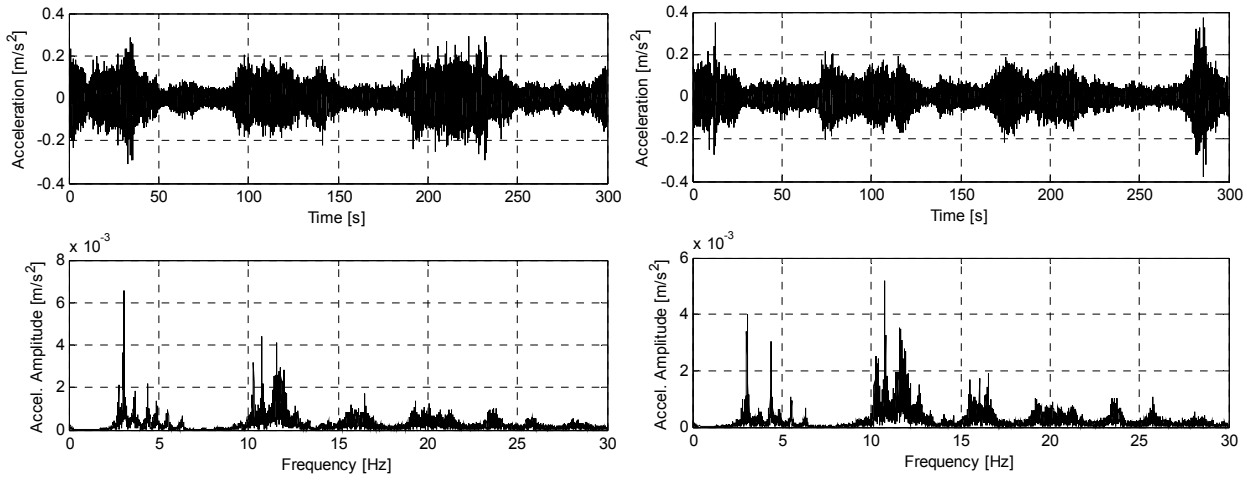

Dataset 5 Dataset 6

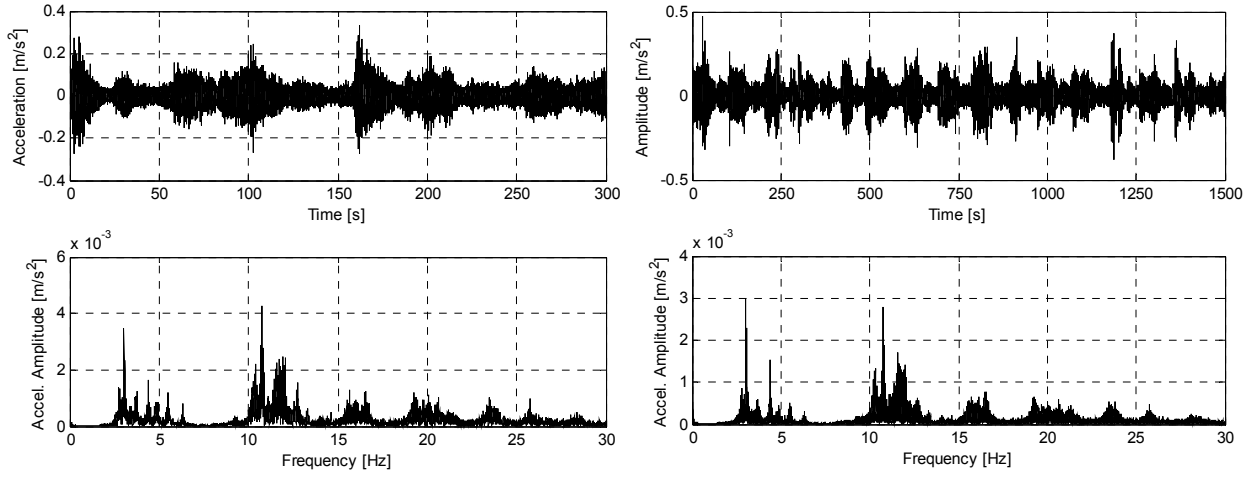

Dataset 7 Concatenated Datasets 3-7

Figure 48: Five 5 minutes bridge acceleration datasets encompassing three full traffic light signal cycles and a concatenated vector encompassing all five 5 minute datasets.

Note that the time series and DFT data in the bottom right corner of Figure 48 does not represent one of these five minute datasets, but instead is the combination of datasets three through seven. It was created by concatenating the acceleration data from the five minute datasets into a single time series acceleration vector representing twenty-five minutes of traffic on the overpass; the shown DFT was obtained from this concatenated vector.

The data was collected for two purposes: (1) to ensure that the PHR technique was able to accurately estimate average power generation when the excitation was representative of typical bridge vibrations and (2) the subsequent use of this data in conjunction with PHR to study harvester optimization (with respect to increasing average power output) using realistic excitation.

To assess the practical applicability of the PHR power estimation technique for harvesting energy off of bridge vibrations, the time series datasets plotted in Figures 47 and 48 were used to produce input excitation for the experimental vibration energy harvester depicted in Figure 49.

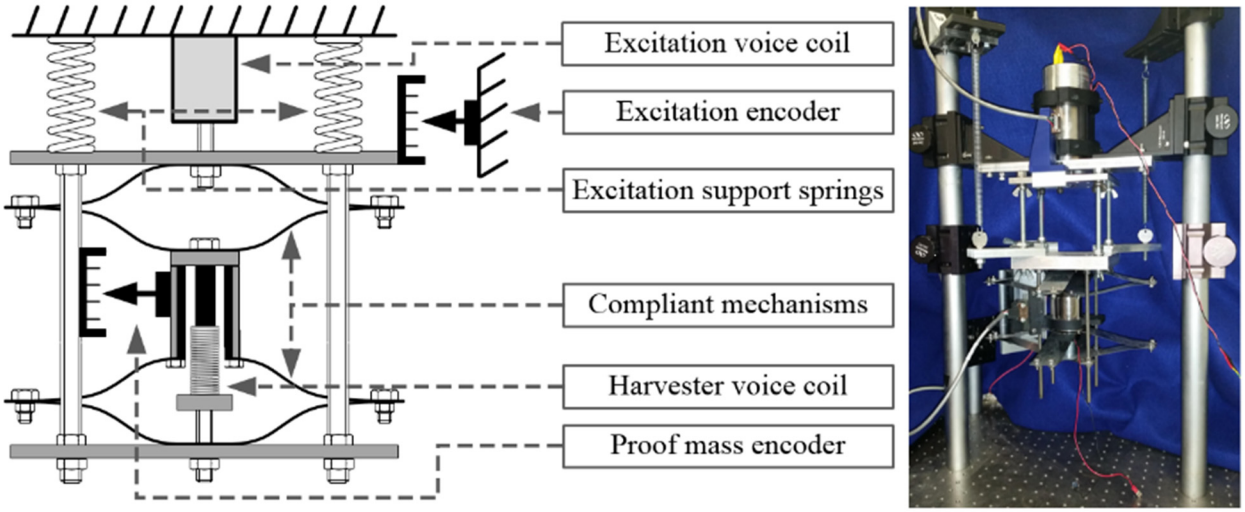

Figure 49: Schematic and photograph of custom vibration energy harvester

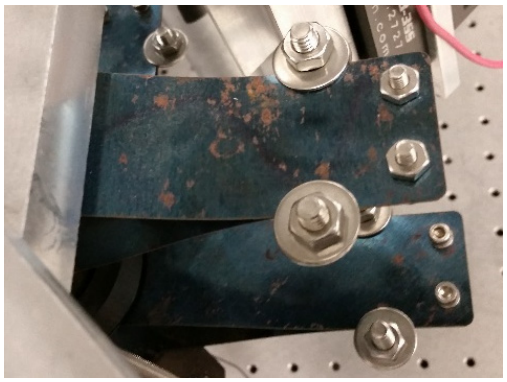

Figure 50: Photograph showing compliant mechanism with simple nut-bolt-washer clamps added to increase effective harvester stiffness

A description of this custom-made experimental harvester can be found in Section 0-5.1 on p. 64III. However, note that the harvester was slightly altered to accommodate the excitation described by Datasets 1-7. Specifically, several simple nut-bolt-washer clamps were attached to the harvester's compliant mechanisms as shown in Figure 50. These clamps were attached in order to quickly and easily increase the harvester's original natural frequency (via an increase in the equivalent stiffness produced by the compliant mechanisms) to be closer in value to a significant frequency component seen on the DFT pots of the considered datasets. By incorporating the clamps, the harvester's initial natural frequency of 7.78 Hz was raised to 10.87 Hz, bringing it much closer to the prominent 10.77 Hz component seen in the DFTs of Datasets 1-7 and, by extension, the concatenated Dataset. This was done to appreciably increase the harvester's ability to efficiently generate power from the mentioned datasets. The addition of the clamps altered the experimental harvester parameters from those listed in Table 8 on p. 66 to those shown in Table 10.

Table 10: New experimental harvester parameters

Parameter	Value
m	0.766 kg
b	7.974 N/(m/s)
k	3575.7 N/m
K_f	17.8 N/A or V/(m/s)
L	0.0031 H
R	7 Ω

Before beginning the testing, in addition to tuning the harvester, Datasets 1-7 and the concatenated dataset were amplified. This amplification was applied to enable the experimental, relatively small-scale harvester to generate greater, and therefore more easily measureable, quantities of power. Since the excitation of each data set was enlarged uniformly using a constant scaling factor throughout, this did not change the shape of the data. Thus, the resulting excitation can still be safely considered representative of typical bridge vibratory behavior. The scaling factors themselves were chosen such that the harvester's proof mass would not collide with the harvester's housing at any point during the emulation of the amplified excitation. The electrical load connected across the harvester leads to extract power was a resistance of 48.6 Ω. Its value was chosen according to PHR to maximize power extraction from the 10.77 Hz frequency component.

Each dataset was run three times and the resulting average power delivered to the load during each experimental run was calculated using

$$\overline{\mathbb{P}}_{\text{tot exp}} = \frac{\sum_{i=1}^{M} V_{L_i} \cdot I_i}{M}, \tag{60}$$

where $\overline{\mathbb{P}}_{\text{tot exp}}$ is the total average power delivered to the electrical load, V_{L_i} and I_i are the load voltage across and current flowing through the harvester leads, respectively, at the time the i^{th} sample was collected by the data acquisition card, and M is the total number of such samples collected. This experimentally measured average power was then compared to the averaged power predicted to be delivered to the load by multiplying the PHR curve by the DFT of the squared amplitude of acceleration of the recorded excitation as described in Section 6.2 on p. 71. The experimental measurements of the current, voltage, and excitation displacement were collected using the hardware described in Section 0-5.1on p. 64. Table 11 displays the results obtained from testing Datasets 1-7 individually, as well as the concatenated excitation comprised of Datasets 3-7. The table's columns identify, from left to right, the Dataset used for testing, the duration of the time series excitation data for the Dataset, the employed scaling factor, the experimentally measured average power delivered to the load, the average power predicted to be delivered to the load according to PHR and the measured excitation, and finally, the error in the PHR estimate when compared to the experimentally measured average power value.

Table 11: Average power generation predicted by PHR and experimentally measured average power generation

Dataset #	Duration [min]	Excitation Scaling Factor	Experimentally Measured [mW]	PHR-predicted [mW]	Error [%]
1	1	20	2.52	2.49	-1.19
			2.51	2.50	-0.40
			2.56	2.51	-1.95
2	1	20	3.24	3.32	2.47
			3.15	3.29	4.44
			3.14	3.29	4.78
3	5	25	4.66	4.62	-0.86
			4.74	4.66	-1.69
			4.74	4.68	-1.27
4	5	20	2.04	2.03	-0.49
			2.06	2.03	-1.46
			2.06	2.03	-1.46
5	5	15	1.35	1.34	-0.67
			1.362	1.360	-0.15
			1.346	1.347	0.07
6	5	25	3.87	3.88	0.26
			3.89	3.88	-0.23
			3.90	3.88	-0.49
7	5	25	3.43	3.47	1.17
			3.44	3.46	0.61
			3.43	3.46	0.85
3-7	25	15	1.41	1.35	-4.05
			1.38	1.32	-4.62
			1.38	1.32	-4.70

As can be seen from Table 11, the PHR technique was always accurate to within 5 % when predicting the experimental harvester's average power generation when the device was exposed to typical bridge vibrations. The high degree of accuracy of this experimentation, coupled with previous results which corroborated PHR's ability to yield precise power generation estimates for variable electrical loads and excitations (e.g., Figure 27 on p. 47, Table 6 on p. 51, and Figures 44 and 45 on pages 75 and 76, respectively), lends confidence to the notion that the PHR technique can reliably predict power generation behavior. This notion is used in the remainder of the present manuscript to make some key observations with respect to harvester architecture choice and tuning and their effect on maximizing average power output.

2. PHR-based Analsys of Choice of Harvester Architecture on Power Output

An important question arises directly from the validation of the power harvesting ratio as an accurate method for estimating harvester power generation. If PHR is capable of predicting power output based on

expected excitation, harvester dynamics, and electric load, can it be used as a tool to create a more efficient energy harvester?

2.1. Introduction of Considered Architectures, Architecture Embodiments, and Assumptions

In order to provide a useful and generalizable answer to this question, three harvester architectures were analyzed using the PHR method. These architectures are depicted in Figure 51, they are: (a) the conventional vibration energy harvester, (2) the harvester array, and (3) the coupled harvester.

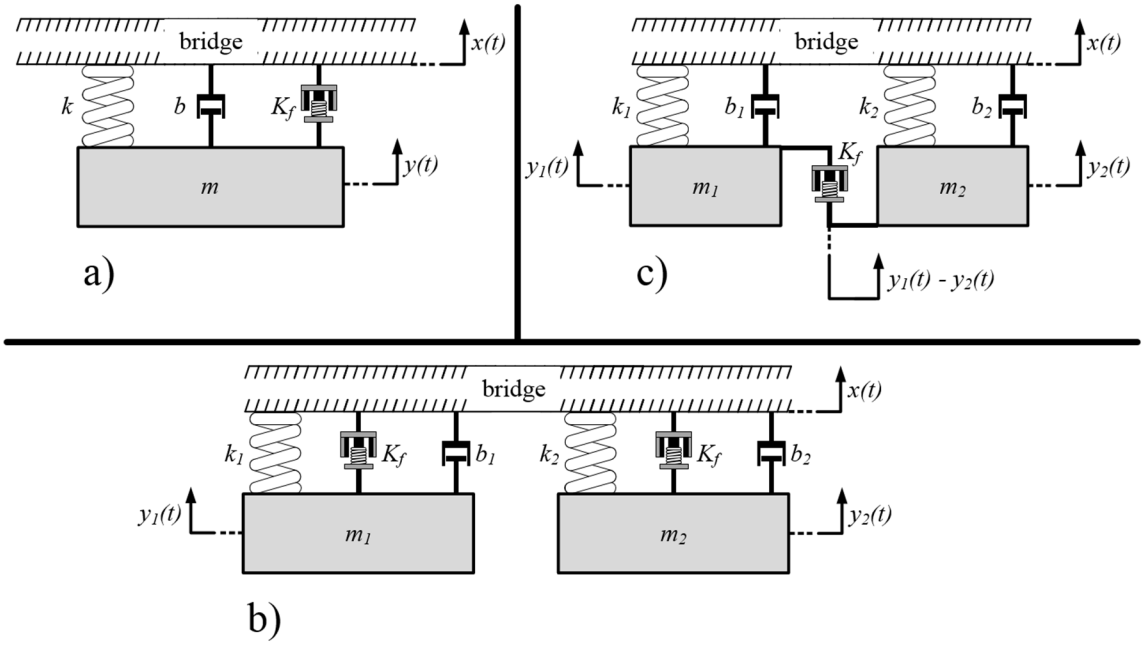

Figure 51: Three electromagnetic vibration energy harvester architectures – a) conventional harvester, b) harvester array and c) coupled harvester

The conventional harvester and harvester array are two harvesting configuration that have been widely studied in literature [18, 19]. Conversely, the coupled harvester, although somewhat similar in design to some existing devices such as the dual-mass system proposed by Tang and Zuo [29], represents an original configuration to the best of the author's knowledge.

In order to compare the efficacy of these three harvester configurations, it was assumed that all three of them were to be employed as vibration energy harvesters that are to generate power from the vibrations of the I-40/I-65 Broadway overpass mentioned in the previous section. It was assumed that the 25 minute long concatenated Dataset 3-7 shown in the lower-right corner of Figure 48 can be treated as the expected input excitation for each of these configurations.

In this analysis, three embodiments were considered for each of the architectures depicted in Figure 51. Descriptions of these embodiments are presented in Sections 2.1.1-2.1.3 with Table 12 included to supplement these descriptions and provide further clarification. Each embodiment has a different scheme for selecting the electrical load and approach to mechanical tuning.

2.1.1. Basic Embodiment

The first embodiment for each configuration was based on the notion that the devices were tuned based exclusively on the chief frequency component of the excitation (in the case of the conventional harvester) or only two most prominent frequency components (in the cases of the harvester array and the coupled harvester). Specifically, the two large peaks occurring at 3.04 Hz and 10.77 Hz of the DFT of the concatenated Dataset 3-7 were taken as the frequency components of interest. This embodiment, designated "Basic", involved tuning the conventional energy harvester's mechanical natural frequency to 10.77 Hz and the mechanical natural frequencies of the two mass-spring-damper systems comprising the harvester array and coupled harvester to 3.04 Hz and 10.77 Hz. Note that the reason that the conventional harvester's natural frequency was tuned to the slightly smaller peak occurring at 10.77 Hz instead of the larger one at 3.04 Hz is to account for the fact that the DFT of the excitation has much more frequency content around the higher frequency peak than it does around the lower frequency one. (As a matter of fact, even though PHR use is purposefully not part of this embodiment, using the technique can numerically show that placing the natural frequency at 10.77 Hz results in a greater amount of generated power.) The electrical load of the "Basic" embodiment was set according to the resistive portion of the maximum power transfer theorem, a traditional load choice for energy harvesting from excitation comprised of a single frequency. The formula dictating this load choice is (50) on p. 66.

2.1.2. PHR-tuned Embodiment

The second embodiment selected for each configuration, termed "PHR-tuned", was formulated using the Power Harvesting Ratio. A numeric optimization algorithm was created for each architecture which set parameter values such that these values resulted in a PHR curve that would predict the largest amount of average power generation when multiplied by the DFT of the excitation's acceleration amplitude squared. More simply put, the parameters of each architecture were selected to maximize the average power yield for the respective architecture as predicted by PHR.

2.1.3. MPTT Embodiment

The third embodiment, termed "MPTT", is based on the maximum power transfer theorem. Certain mechanical parameters of each architecture (specifically which ones is shown in Table 12) are set by a

similar optimization algorithm that was used for the PHR-tuned Embodiment, while the electrical load is set in accordance with MPTT to be the complex conjugate of the particular architecture's Thévenin equivalent source impedance. The source impedances for each architecture are shown in Figure 52 (note that the harvester array architecture is comprised of two Thévenin equivalent circuits, each having its own equivalent source impedance); they were found using the same procedure as was used for the conventional harvester in Section 0-3 on p. 36.

It was shown in Section 0-6.1.1 on p. 68 that trying to implement an active electrical load dictated by MPTT results in unstable harvester dynamics. The same section also explains why this observation necessarily implies that it is impossible to actively enforce a load which would result in the maximum amount of power being delivered to it from several frequencies at once, or that would autonomously adjust to the excitation frequency to enforce this same maximum power transfer behavior. Thus, the purpose of including the MPTT Embodiments for each configuration is that the PHR plots of these embodiments will represent upper bounds for the architectures' respective frequency-dependent power generation behaviors. As was mentioned in Section 0-7, a harvester with a particularly formulated active load may actually outperform the same harvester with an optimized purely passive load, but this same active load will never be able to surpass the average power generation predicted for the MPTT-dictated active load.

Table 12 supplements the above descriptions of the embodiments to help the reader understand exactly what parameters were set and which were solved for in each architecture/embodiment combination.

Several notes should be made about the parameters listed in the table. First, note those parameters which were held constant for all harvester architectures: total magnitude of the proof mass ($m = (m_1 + m_2) = 1.394$ kg), mechanical viscous damping constant associated with each mass-spring-damper ($b = b_1 = b_2 = 7.294\ \mathrm{N \cdot s/m}$), and all of the electrical parameters associated with each individual linear voice coil used for generation ($R = 7\ \Omega$, $L = 3.1$ mH and $K_f = 17.8$ N/A or $\mathrm{V \cdot s/m}$). These parameters are not those shown in Table 10, but they are physically achievable values.

The parameters m, b, R, L, and K_f were held constant across architectures to make fair comparisons. The magnitude of the total amount of proof mass was held constant to ensure that no architecture had an unfair advantage that would stem from generating power from the motion of a greater mass. The damping was held constant to reflect the assumption that each mass-spring-damper configuration could not be fabricated more efficiently than the experimental harvester by reducing the mechanical parasitic damping. Finally, it was assumed that all electromagnetic voice coils used to generate power from proof mass motion were identical. Note, that the harvester array contains two such voice coils, a fact that should be taken into account when taking implementation cost into consideration.

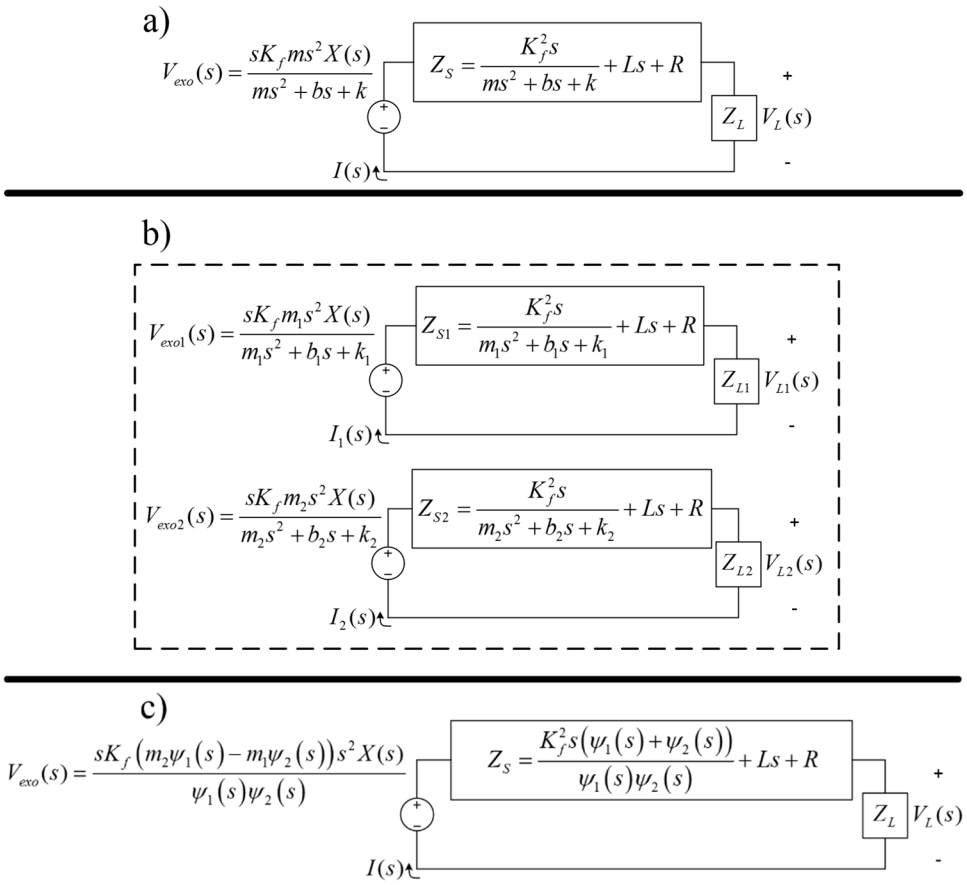

Figure 52: Thévenin equivalent circuit representations of a) conventional harvester, b) harvester array (note: comprised of two Thévenin equivalent circuits) and c) coupled harvester. Note: $\psi_1(s) = m_1 s^2 + b_1 s + k_1$ and $\psi_2(s) = m_2 s^2 + b_2 s + k_2$.

Two key constraints were placed in solving for or setting the parameter values in Table 12. They are: (1) the allotted proof mass is distributed equally between the two mass-spring-damper systems comprising the harvester array and coupled harvester and (2) the search algorithm used to solve for the spring stiffnesses of the harvester array was constrained such that the mass-spring-damper systems of this architecture would have two separate natural frequencies – one in the 2-5 Hz range, and another in the 10-13 Hz range. The justifications for placing these constraints will be disclosed after viewing the PHR curves of all the architecture/embodiment combinations.

Table 12: Architecture/Embodiment Set and Solved for Parameters

Embodiment → Architecture ↓	Basic	PHR-tuned	MPTT
Conventional Harvester	Set: $m = 1.394$ kg $b = 7.294$ N · s/m $k = 6383 \frac{\text{N}}{\text{m}}$ $R_L = 50.4\,\Omega$	Set: $m = 1.394$ kg $b = 7.294$ N · s/m **Solved for:** $\boldsymbol{k = 7152}$ **N/m** $\boldsymbol{R_L = 32.5\,\Omega}$	Set: $m = 1.394$ kg $b = 7.294$ N · s/m $Z_L = -Ls + R - \frac{K_f^2 s}{ms^2 - bs + k}$ **Solved for:** $\boldsymbol{k = 7027}$ **N/m**
Harvester Array	Set: $m_1 = 0.697$ kg $m_2 = 0.697$ kg $b_1 = 7.294$ N · s/m $b_2 = 7.294$ N · s/m $k_1 = 254$ N · s/m $k_2 = 3192$ N · s/m $R_{L1} = 50.4\,\Omega$ $R_{L2} = 50.4\,\Omega$	Set $m_1 = 0.697$ kg $m_2 = 0.697$ kg $b_1 = 7.294$ N · s/m $b_2 = 7.294$ N · s/m **Solved for:** $\boldsymbol{k_1 = 282}$ **N · s/m** $\boldsymbol{k_2 = 3452}$ **N · s/m** $\boldsymbol{R_{L1} = 29.6\,\Omega}$ $\boldsymbol{R_{L2} = 39\,\Omega}$	Set $m_1 = 0.697$ kg $m_2 = 0.697$ kg $b_1 = 7.294$ N · s/m $b_2 = 7.294$ N · s/m $Z_{L1} = -Ls + R - \frac{K_f^2 s}{m_1 s^2 - b_1 s + k_1}$ $Z_{L2} = -Ls + R - \frac{K_f^2 s}{m_2 s^2 - b_2 s + k_2}$ **Solved for:** $\boldsymbol{k_1 = 254}$ **N · s/m** $\boldsymbol{k_2 = 3192}$ **N · s/m**
Coupled Harvester	Set: $m_1 = 0.697$ kg $m_2 = 0.697$ kg $b_1 = 7.294$ N · s/m $b_2 = 7.294$ N · s/m $k_1 = 254$ N · s/m $k_2 = 3192$ N · s/m $R_L = 50.4\,\Omega$	Set: $m_1 = 0.697$ kg $m_2 = 0.697$ kg $b_1 = 7.294$ N · s/m $b_2 = 7.294$ N · s/m **Solved for:** $\boldsymbol{k_1 = 254}$ **N · s/m** $\boldsymbol{k_2 = 4029}$ **N · s/m** $\boldsymbol{R_L = 34.75\,\Omega}$	Set: $m_1 = 0.697$ kg $m_2 = 0.697$ kg $b_1 = 7.294$ N · s/m $b_2 = 7.294$ N · s/m $Z_L = -Ls + R - \frac{K_f^2 s(\delta_1(s) + \delta_2(s))}{\delta_1(s)\delta_2(s)}$ $\delta_1(s) = m_1 s^2 - b_1 s + k_1$ $\delta_2(s) = m_2 s^2 - b_2 s + k_2$ **Solve for:** $\boldsymbol{k_1 = 254}$ **N · s/m** $\boldsymbol{k_2 = 4163}$ **N · s/m**

2.2. Simulated Power Generation Results of the Architecture/Embodiment Combinations

Figure 53, Figure 54 and Figure 55 display the PHR curves of all three embodiments for the conventional harvester, harvester array, and coupled harvester architectures, respectively. The resulting PHR curves are

overlaid on top of the DFT of Dataset's 3-7 acceleration amplitude squared to illustrate from which excitation frequencies a particular architecture/embodiment combination harvests power most efficiently.

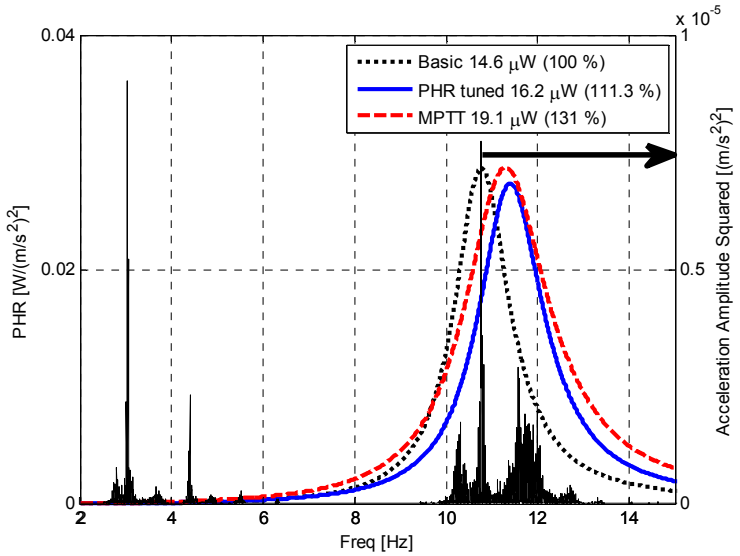

Figure 53: Conventional harvester PHR curves resulting from basic tuning, PHR-based optimization, and theoretical upper bound of average power generation defined by the MPTT-dictated load and DFT of the squared acceleration amplitude of the expected excitation

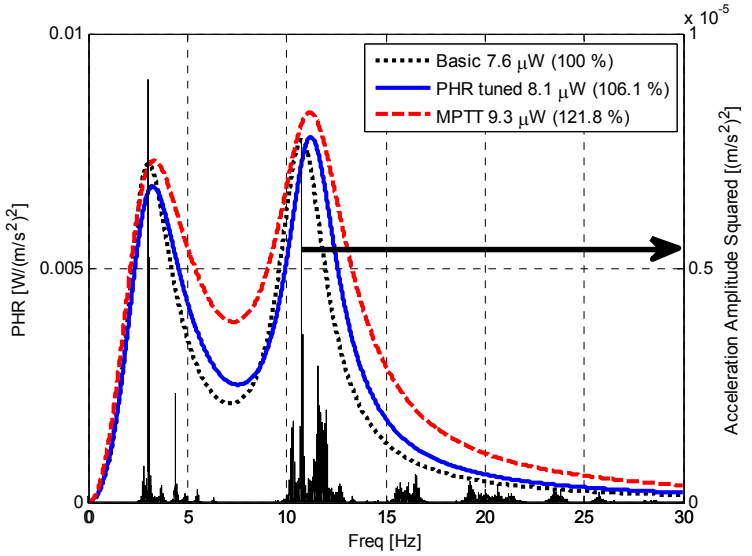

Figure 54: Harvester array PHR curves resulting from basic tuning, PHR-based optimization, and theoretical upper bound of average power generation defined by the MPTT-dictated load and DFT of the squared acceleration amplitude of the expected excitation

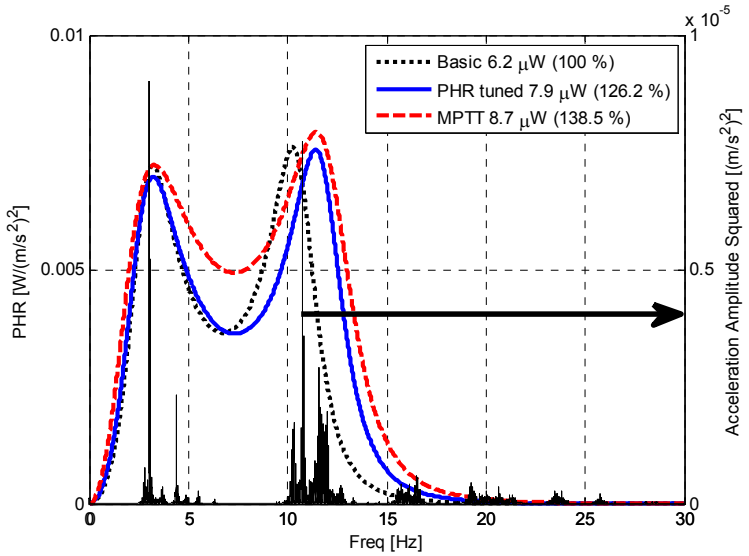

Figure 55: Coupled harvester PHR curves resulting from basic tuning, PHR-based optimization, and theoretical upper bound of average power generation defined by the MPTT-dictated load and DFT of the squared acceleration amplitude of the expected excitation

The legends placed in the top right corners of the above figures display values of the total average power predicted to be generated by each architecture/embodiment pair based on the pair's PHR curve and the excitation DFT. These values were calculated using equations (56) and (57) on pages 71 and 73, respectively. The percentages shown in parentheses are these same values normalized with respect to the power generation predicted for the Basic Embodiment. The fact that these values are much smaller than those appearing in Table 11 on p 85 is due to the used excitation being left unscaled.

The displayed results indicate that the use of numerical optimization algorithms based on PHR can increase the power generation of a vibration energy harvester by anywhere from 6 % to 26 % as compared to following the Basic Embodiment strategy of selecting harvester parameter values. Note that the coupled harvester architecture benefits the most from having its parameters tuned using PHR. Furthermore, though the coupled harvester relies only on a single voice coil for power generation, its predicted average power output is just approximately 3 % below that of the PHR-tuned harvester array

However, arguably the most important observation to be made about Figures 53-55 is that the average power generation predicted for the conventional harvester is approximately twice as large as it is for the other two architectures. To illustrate this more clearly, the PHR curves of the PHR-tuned embodiments of each architecture are placed on the same plot in Figure 56; the normalization used in the legend is now performed with respect to the power generation of the conventional harvester.

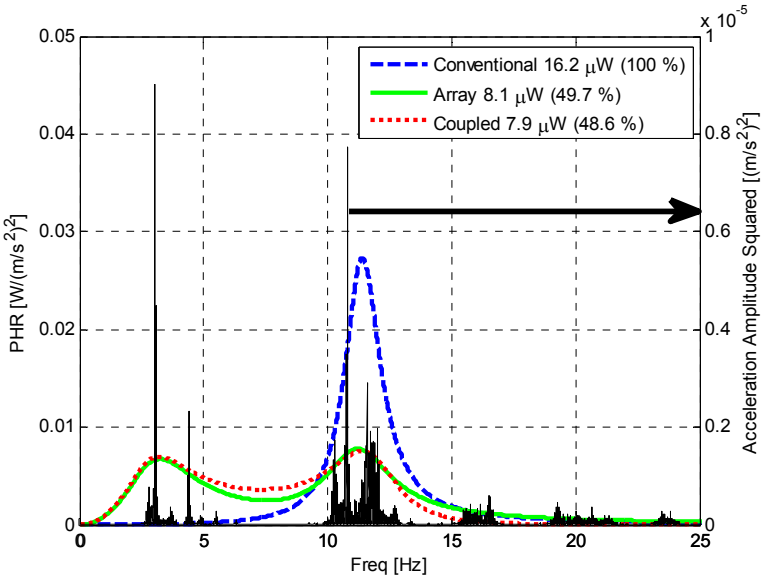

Figure 56: Average PHR-tuned power generation behavior of three vibration energy harvester architectures: conventional, harvester array, and coupled harvester and DFT of the squared acceleration amplitude of the expected excitation

Whereas the harvester array and coupled harvester are generating power efficiently around both the 3.04 Hz and 10.77 Hz peaks in the excitation's DFT (i.e., the peaks in these architectures' PHR curves are located close to these frequencies), the conventional harvester is generating power efficiently only at the higher frequency. However, the conventional harvester's PHR curve's peak is several times larger in magnitude than that of the other two architectures, consequently causing its total average power output to be much larger.

The reason for the relative disparity between the peak amplitudes achieved by the PHR curves shown in Figure 56 stems from the dependence of the considered harvester architectures' (i.e., those reliant on mass-spring-damper systems) maximum achievable power on proof mass distribution.

The exact nature of this dependence can be derived analytically by setting $s = j\omega_n$ in (49) on p. 60 and noting that the resulting expression will be proportional to m^2. This proportionality is illustrated in Figure 57.

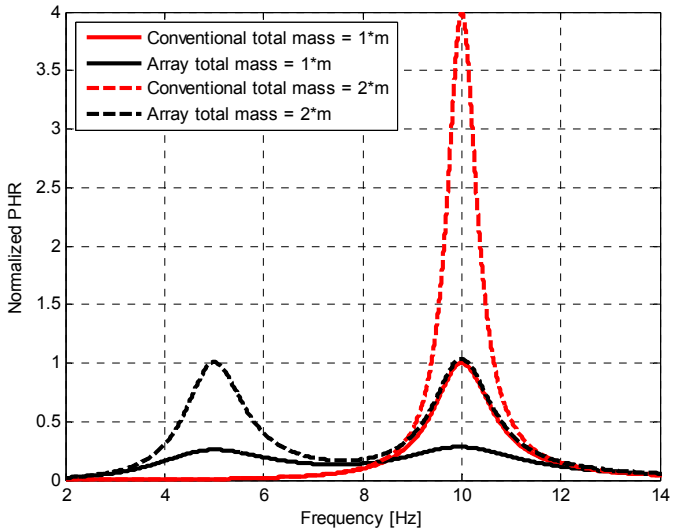

Figure 57: Effect of mass distribution on energy harvesting potential demonstrated by conventional harvester and harvester array comprised of two harvesters having equal proof masses

The PHR curves shown in the above figure describe: (1) a conventional harvester having a proof mass of magnitude $1*m$ with a mechanical natural frequency of 10 Hz, (2) a conventional harvester having the same natural frequency but with a proof mass $2 * m$ that is twice as large, (3) a harvester array with two mass-spring-damper systems which are tuned to 5 Hz and 10 Hz with each having an associated proof mass of magnitude $0.5 * m$, and (4) a harvester array whose mass-spring-damper systems are tuned to the same two frequencies, but the proof masses of which are both $1 * m$. All four systems were similarly tuned using the Basic Embodiment tuning scheme and the PHR curves are all normalized with respect to the peak amplitude achieved by the curve of the conventional harvester with a total mass of $1 * m$ (note: the curves themselves are normalized in the figure, not power quantities). As both solid line curves and both dashed line curves represent energy harvesting systems having the same amount of total proof mass, Figure 57 serves to show the effect that distributing mass produces.

As previously stated, the peak amplitude achieved by a PHR curve is proportional to the squared magnitude of proof mass. Thus, when the proof mass is split evenly between the two mass-spring-damper systems comprising the harvester array, the array's two voice coils are able to each supply their respective electrical loads with only a quarter of the peak power that is delivered by the voice coil of the conventional harvester to its electrical load. When the total amount of proof mass is doubled for each architecture, the new PHR curves behave as expected. The $2 * m$ harvester array curve now slightly exceeds the $1 * m$ conventional curve (the slight advantage stems from the small amount of power that the 3 Hz harvester that is part of the array generates at 10 Hz), while the $2 * m$ conventional harvester's PHR curve achieves four times the peak value of its $1 * m$ counterpart.

This advantage of keeping the entire proof mass together was discovered during initial runs of the optimization algorithm to determine the PHR-tuned Embodiment parameters. When the total amount of mass was set for the harvester array and the coupled harvester, but the distribution of this mass was left to be determined by the optimization algorithm, the algorithm always allocated the entire mass to one of the mass-spring-damper systems. The parameter values resulting from the optimization algorithms were such that both, the harvester array and the coupled harvester, were essentially transformed into the conventional harvester configuration. For this reason, the total amount of proof mass was set to be distributed equally between the two mass-spring-damper systems of the non-conventional harvester architectures, as was stated on p. 89.

Another noteworthy observation was made from the initial results of the optimization algorithms, specifically the algorithms applied to the harvester array. Specifically, even with the proof mass distributed equally between the two mass-spring-damper systems comprising the array, the first results of the optimization unexpectedly resulted in a PHR curve with a single peak, akin to that of the conventional harvester. The reason for this result was that the optimization algorithm was assigning the same stiffness as to both of the mass-spring-damper systems, thereby designating the same natural frequency for both harvesters constituting the array. This had the effect of producing a PHR curve for the harvester array which was essentially that of a less efficient conventional energy harvester (for the given total amount of proof mass). Once again, in order to prevent the optimization algorithm from converting the harvester array architecture into that of a conventional harvester, a constraint was placed on the range of stiffnesses of its two mass-spring-damper systems. The stiffnesses were to be selected such that the harvester array's two comprising harvesters had two different natural frequencies, one in the 2-5 Hz range and another in the 10-13 Hz range, as noted in the second constraint on p. 89. These ranges were selected based on frequency spectrum locations where significant frequency content existed in excitation's DFT.

Given the constraints that had to be placed on the optimization algorithms, several important conclusions are drawn from the simulation results. Given a vibration energy harvester which generates power by relying on a mass-spring-damper system to amplify the motion of some proof mass, it is generally best to (1) attach a single harvester with as large of a proof mass as practically possible, rather than distribute the same amount of mass between some number of mass-spring-damper systems comprising (a) harvester array(s) or (a) coupled harvester(s) and (2) tune the harvester such that its mechanical natural frequency is centered at the location where most frequency content (in terms of amplitude and density) exists in the excitation. The last suggestions may seem evident, but there have been cases in literature that suggest that should an excitation contain frequency components that are removed from the natural frequency (or frequencies) of a vibration harvester (or harvesters) that are generating power from said excitation, than that power is wasted (e.g., [40]). This claim is true in a sense. However, according to the observation concerning peak achievable

power's dependence on the square of the magnitude of proof mass, overall average power generation would benefit more from adding mass to/increasing the maximum power generation of a single harvester, the natural frequency of which is centered around the largest and most dense part of the excitation's DFT, than it would from trying to harvest energy from each non-trivial frequency component.

It is, however, very important to note that the above assertions are made under the assumption that the DFT of the expected excitation is known and static (i.e, the frequency content of the excitation, as defined by the present frequency components and the respective magnitudes of these components, never changes). Looking at the DFTs of the vibration data collected from the I-40/I-65 Broadway overpass shown in Figure 47 and Figure 48 on pgs. 80-81 would lead one to believe that the overpass's frequency content, at least at the location where the accelerometer was attached, is relatively constant. However, it should be noted that the data was collected on the same day within approximately an hour time window. Therefore, the similarity between the DFTs can only be used to conclude that the frequency content of the vibrations at the sensor's location does not change very quickly.

As was mentioned in [6] different traffic conditions may actually result in a bridge exhibiting a different vibratory response. However, difference in a bridge's vibrational behavior caused by variable traffic conditions are smaller in scope and much more transient in nature than those caused by changes in temperature. As noted in a review paper by Zhou and Yi, primary bridge modes can shift in frequency by anywhere from 0.2 % to about 20 % due to temperature changes [45]. Since the above inferences and conclusions drawn from the simulation results were based on the assumption of a known, static excitation DFT, it was desirable to discover to which degree they were still applicable when the excitation became variable.

2.3. Effect of Variable Excitation on Analysis Results

2.3.1. Effect of Frequency Shifts

As stated in the previous section, variation in temperature can alter the frequencies at which primary bridge modes occur. Usually, increases in temperature tend to decrease bridge mode frequencies, while colder temperature cause bridge modes to shift up in frequency. To examine the effect that changes in temperature would have on power generation, a new excitation DFT was created from that of the concatenated Dataset 3-7 previously used. This new DFT was made to simulate the variation in frequency over a long period of time. It was assumed that one third of the time warmer temperatures caused the bridge's frequency behavior to shift down 1 Hz, another third of the time cold temperatures caused the frequency behavior to shift up by 1 Hz, and yet another third of the time the frequency behavior stayed unchanged. This new excitation was then used to rerun the optimization algorithms used for the PHR-tuned Embodiment described in Section 2.1.2 to solve for the same parameters as indicated in Table 12 on p. 90.

The resulting PHR curves of the three architectures for this embodiment are shown along with the DFT of the new excitation's acceleration amplitude squared below in Figure 58.

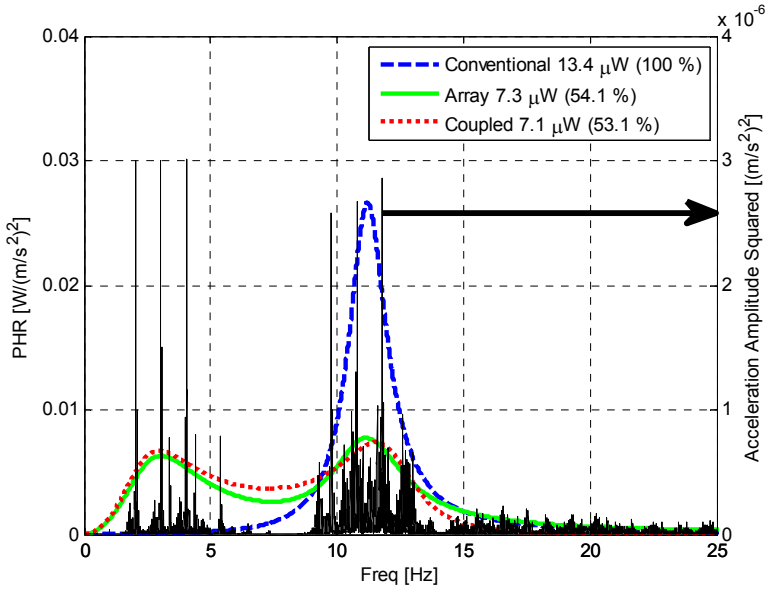

Figure 58: DFT of the squared acceleration amplitude of the new excitation and average power generation behavior of three vibration energy harvester architectures assuming shifting excitation DFT: conventional, harvester array, and coupled harvester.

Although the conventional harvester architecture still surpasses the other two in overall predicted average power generation, its relative advantage is decreased by about 5 %, as can be seen from a direct comparison to Figure 56 on p. 93. Also, note that once again the coupled harvester has a very similar PHR curve to that of the harvester array and is predicted to generate almost the same amount of power while using only one voice coil. Since the coupled harvester is thus a more efficient architecture, the harvester array is no longer considered in the following analysis.

Before furthering analyzing the effect of frequency shifts on power generation, it was decided to determine the mass increases necessary for a coupled harvester to (1) match the total average power geneartion of the convnetional harvester and (2) outperform a conventional harvester at all frequencies according to their respecitve PHR curves. The PHR curves of the PHR-tuned and MPTT Embodiments of the conventional harvester and coupled harvester with the larger proof masses are shown in Figure 59 and Figure 60.

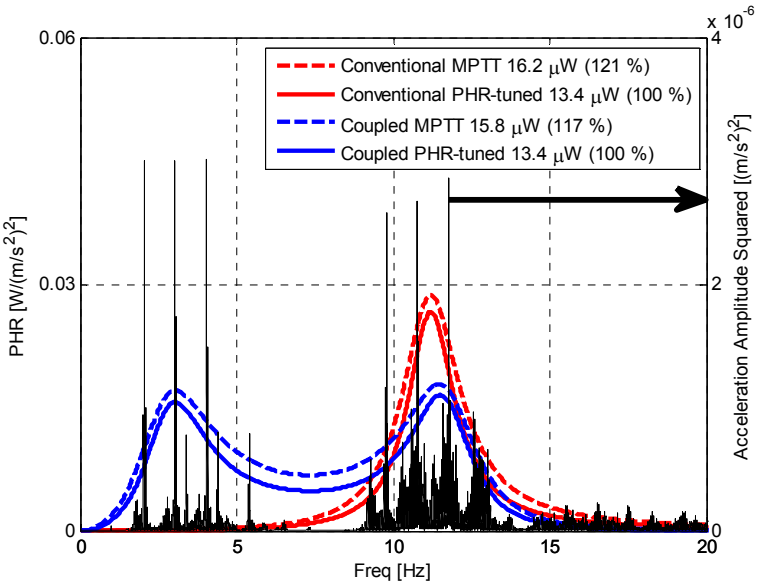

Figure 59: DFT of the squared acceleration amplitude of the new excitation and average PHR-tuned power generation behaviors of the conventional vibration energy harvester and the coupled harvester with increased proof masses (total mass 54 % larger than conventional). MPTT-dictated load curves represent theoretical upper bounds for active loading

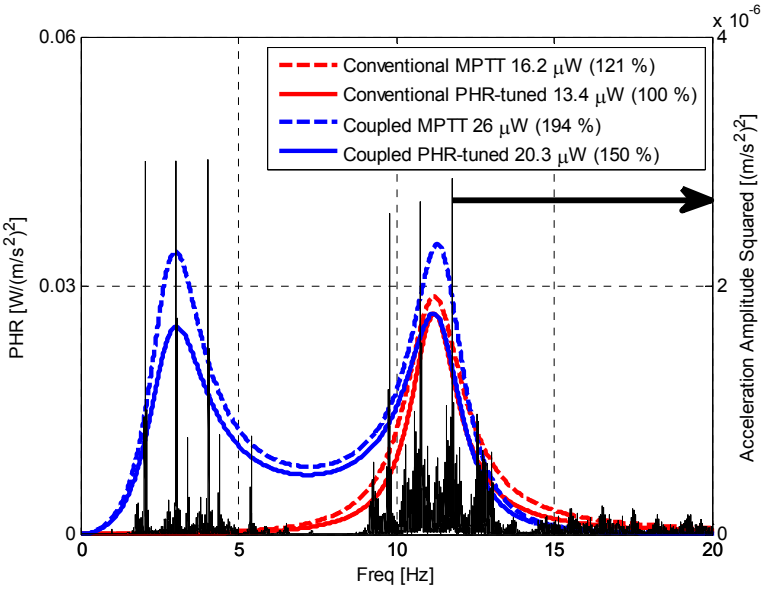

Figure 60: DFT of the squared acceleration amplitude of the new excitation and average PHR-tuned power generation behaviors of the conventional vibration energy harvester and the coupled harvester with increased proof masses (total mass 118 % larger than conventional). MPTT-dictated load curves represent theoretical upper bounds for active loading

The MPTT Embodiments were included in the preceeding figures to show the theoretical upper bounds on active tuning, as was discussed in Section 2.1.3 on p. 87.

In order to achieve the same average power generation as that of the conventional harvester, the array's total proof mass had to be made 54 % larger than the proof mass used by the conventional architecture. To outperform the conventional harvester at almost all frequencies, this increase in total proof mass had to be raised to 118 %.

It's important to note that the heavier PHR-tuned coupled harvester outperforms the PHR-tuned conventional harvester *almost* at all frequencies. As can be seen from Figure 60, the curve of the PHR-tuned coupled harvester lies on or above that of the PHR-tuned conventional harvester for all frequencies up to approximately 12.3 Hz. Since the excitation does not contain a significant amount of frequency content above 12.3 Hz, and since the mass increases required to force the coupled harvester's curve to rise above that of the conventional harvester beyond that frequency were quite high, the coupled harvester's inferior performance at frequencies above 12.3 Hz was deemed acceptable.

For the remainder of the present manuscript, the coupled harvester which achieved the conventional harvester's average power generation via a 54 % total proof mass increase will be referred to as "equivalent coupled harvester" or ECH and the coupled harvester which outperformed the conventional harvester (up to 12.3 Hz) will be referred to as "superior coupled harvester" or SCH.

Whereas Figures 59 and 60 show the average power generation over the entire time that the harvester architectures would be generating power, it is also of interest to analyze the architectures' power generation during each frequency shift period. For example, if seasonal changes cause the temperature to become colder for 1/3rd of the year, and the frequency content of the excitation's DFT is shifted up by 1 Hz, how much average power would each configuration generate during this period?

Table 13 and Figure 60 show how the average power output of each of the considered architectures would be affected during the $\pm$ 1 Hz frequency shifts – the table provides the exact numbers while the figure makes it easier to compare power outputs of different architectures during different "temperature periods".

Table 13: Average Power Generation During Frequency Shifts

	Average Power Generation (μW)		
	+ 1 Hz	No Shift	- 1 Hz
Conventional MPTT	14.53	19.06	15.05
Conventional PHR-tuned	11.85	16.12	12.32
ECH MPTT	14.53	18.06	14.75
ECH PHR-tuned	12.36	15.88	12.07
SCH MPTT	21.68	31.79	24.56
SCH PHR-tuned	16.38	24.36	20.18

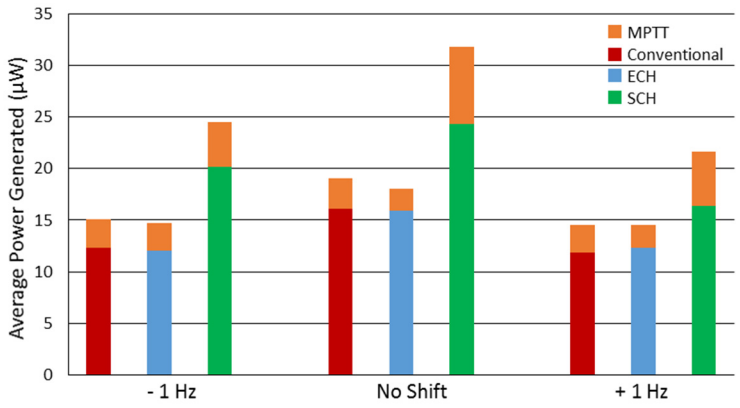

Figure 61: Average Power Generation During Frequency Shifts

Once again, the MPTT results are included as a theoretical upper bound for if an active load is employed in an attempt to further boost a particular architecture's average power generation.

From Figure 61 it's easy to see that the average power generation predicted by PHR is almost identical for the conventional harvester and the ECH for both frequency shifted cases, as well as the unaltered excitation. It may be of interest to note that even when its power generation is at its minimum, the PHR-tuned SCH still outperforms the PHR-conventional harvester during all temperature periods. This is not unexpected, as SCH was explicitly designed for that purpose.

2.3.2. Effect of Amplitude Changes

All of the previous simulation results have demonstrated that the performance of the conventional harvester is in many ways superior to that of the coupled harvester and the harvester array for the chosen excitation. This was especially true when the total amount of allotted proof mass was held constant across all architectures. Furthermore, it was shown that even when the excitation's DFT was shifted up or down in frequency by 1 Hz, the conventional harvester could still generate as much power as that produced by a coupled harvester employing 54 % more mass during these frequency shifts. Given these results, the logical question to ask becomes whether the conventional harvester architecture has any disadvantages compared to the architecture of the coupled harvester.

This question is answered by considering the other type of possible variation in the excitation's DFT – a change in amplitude of comprising frequency components. Note that the conventional harvester relies heavily on the amplitude of frequency components around which its mechanical natural frequency is centered. Recall that when using the PHR technique for estimating total average power generation of a harvester, the particular harvester's PHR curve is multiplied by the squared amplitude of the excitation's acceleration. Therefore, when the amplitude of a particular frequency component comprising the excitation is reduced by a factor x, the power generated from that frequency component is reduced by a factor of x^2.

Although this fact applies to all three of the discussed architectures, since the conventional harvester generates power in only one of the two frequency ranges used by the other two architectures, its total power output is more sensitive to amplitude reductions within this range.

To illustrate this point, the concatenated Dataset 3-7 was once again altered to produce a new excitation DFT. This time, it was assumed that all frequency components existing above 8 Hz have decreased in amplitude by 50 %. This change is assumed to have been unforeseen and, therefore, occurred after the coupled harvester and the conventional harvester have already had their parameters set such that their power generation behaviors are described by their respective PHR-tuned curves shown in Figure 59 on p. 98. The consequent average power generation predictions are shown in Figure 62.

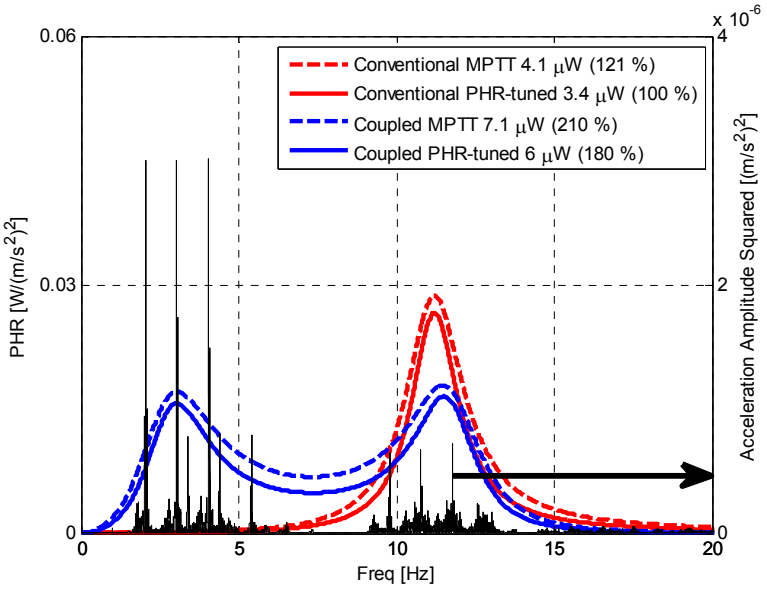

Figure 62: DFT of the squared amplitude of the acceleration of excitation with attenuated higher frequencies and average PHR-tuned power generation behaviors of the conventional vibration energy harvester and the coupled harvester with increased proof masses (total mass 54 % larger than conventional). MPTT-dictated load curves represent theoretical upper bounds for active loading

Note that whereas the coupled harvester configuration used to generate the same amount of average power as the conventional harvester with the unaltered excitation, the decrease of the amplitudes of the higher frequency components has caused the coupled harvester's average power generation to be 80 % larger than that of the conventional. Both configurations lost a large portion of their predicted power generation, but whereas the conventional harvester dropped from 13.4 μW to 3.4 μW (a loss of approximate 75 %), the coupled harvester suffered a smaller decrease, going from the same 13.4 μW to 6 μW (a loss of approximately 55 %).

Therefore, the reliance of average power generation on the square of the amplitudes of the excitation's frequency components becomes somewhat of a counterargument to the previous assertion that the proof mass should not be distributed. If the expected excitation DFT retains a constant shape, then a single proof mass should be employed, and a harvester comprised of a single mass-spring-damper system having a natural frequency centered around the largest excitation frequency component (while also accounting for frequency content density) would result in the most power being generated. However, if the amplitudes of the excitation's frequency components exhibit a fair degree of variation, by splitting the proof mass between the mass-spring-damper systems of a coupled harvester, the minimum total average amount of power generated at any point in time can be increased. This increase would stem from diminishing the generated amount of power's sensitivity to amplitude reductions.

3. Overarching Conclusions from PHR-based Analysis of Power Generation from Vibrations

Based on fairly extensive experimental validation of the accuracy of the PHR method in predicting average power generation, it was considered appropriate to use the method for the purpose of discovering how to increase power yield of vibration energy harvesting as a whole.

Based on the simulation results detailed in the previous section, inferences can be drawn about energy harvesting from excitation having a largely static/constant DFT and harvesting from an excitation the frequency components of which experience significant frequency and amplitude changes over time.

3.1. Excitation with a Static DFT

If the shape of the DFT of a vibratory excitation source remains constant, a conventional harvester should be employed in order to maximize power generation from the source's vibrations. The proof mass should not be divided and the mechanical natural frequency of the device should be set to the largest frequency component observed in the excitation's DFT. If several components have similar magnitudes, or the excitation's DFT contains a smaller peak that has a lot of frequency content surrounding it, an optimization routine using the PHR equation (49) on p. 60, equations (42) and (43) on pp. 48 and 49, respectively, and the DFT of the squared amplitude of the excitation's acceleration can be run to determine where the natural frequency should be placed. The same optimization routine can be used to yield the optimum resistive load, or, should the user be so inclined, estimate power for active load candidates. Before trying to implement a particular active load, it should be verified as usable using the Nyquist Stability method detailed in Section 0-3.2 on p. 59 to ensure it would not cause the overall harvester dynamics to become unstable. It is also recommended to use the MPTT dictated load impedance as the electrical load in the PHR estimation technique prior to looking into active loading. Although such a load cannot be implemented in the

harvesting system, the resulting predicted average power will provide a theoretical upper bound which, if considered to be too modest, may reveal that active loading is not worth pursuing.

3.2. Excitation with a Varying DFT

When the shape of the DFT of the vibratory excitation source is not constant, when the components comprising the excitation have varying amplitudes and frequencies, it becomes much more difficult to make concrete assertions on how to go about maximizing power generation. The conclusions drawn in Section 2.2 and 2.3, above, were obtained using specific harvester parameters, excitation data gathered from a particular bridge, and unique assumptions on DFT variation. If, for example, the experimental harvester's damping ratio had been significantly different, or if the overpass's significant modes were either grouped closer together or were further apart, the conclusions about architecture choices and tuning could have been drastically different. However, even though the simulation results may not be generalizable in the strictest sense and hold only for the specific studied case, the techniques and associated observations can be applied to other situations where power is being harvested from an excitation source with a variable DFT.

The PHR method for estimating power generation provides accurate results as long as the (linear) dynamics of the harvester, (linear) dynamics of the electrical load, and the DFT of the excitation are known. Even though the DFT might vary in shape, as long as those variations can be quantified, PHR can still be used to aid in harvester architecture selection, design/tuning of an existing harvester, or to simply predict lower and upper bounds of power generation.

Therefore, even though concrete rules for maximizing power generation for excitation with a varying DFT cannot be formulated as they were for the case in which the DFT of the excitation was static, the use of PHR in conjunction with a thorough understanding of how the DFT of the excitation varies can still lead to improvements in overall power generation from the vibration source.

APPENDIX D: SIMULINK DIAGRAMS AND MATLAB CODE

1. Simulink Diagrams

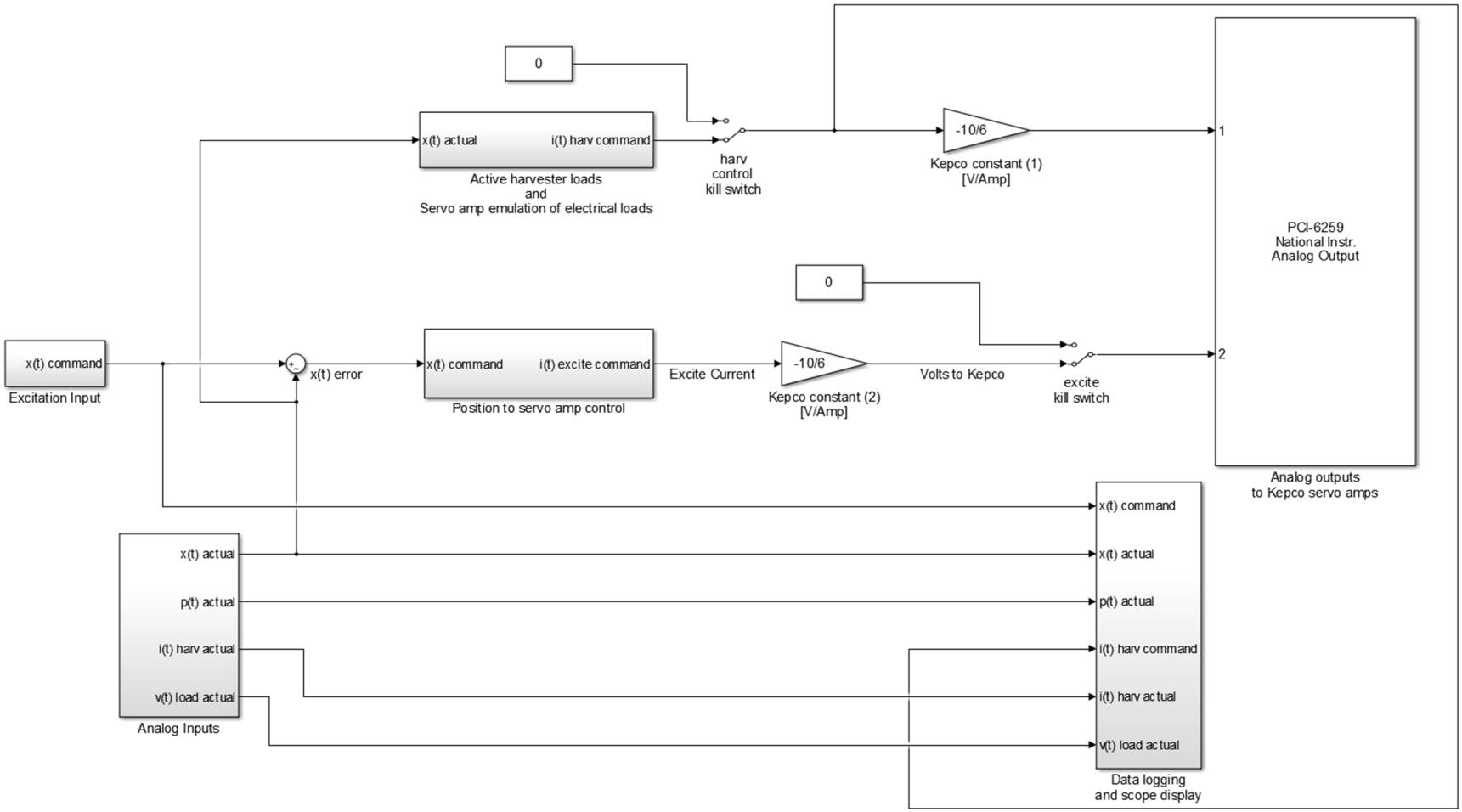

Figure 63: Experimental setup Simulink block diagram

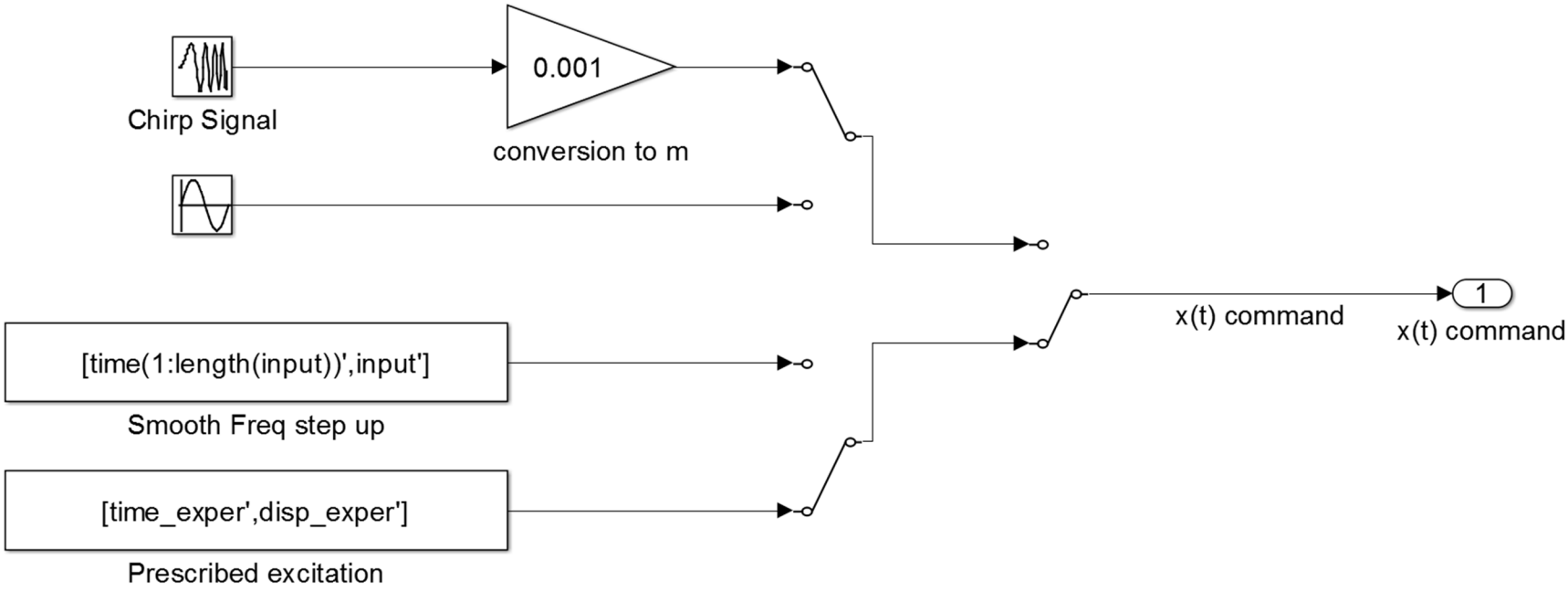

Figure 64: Excitation Input subsystem

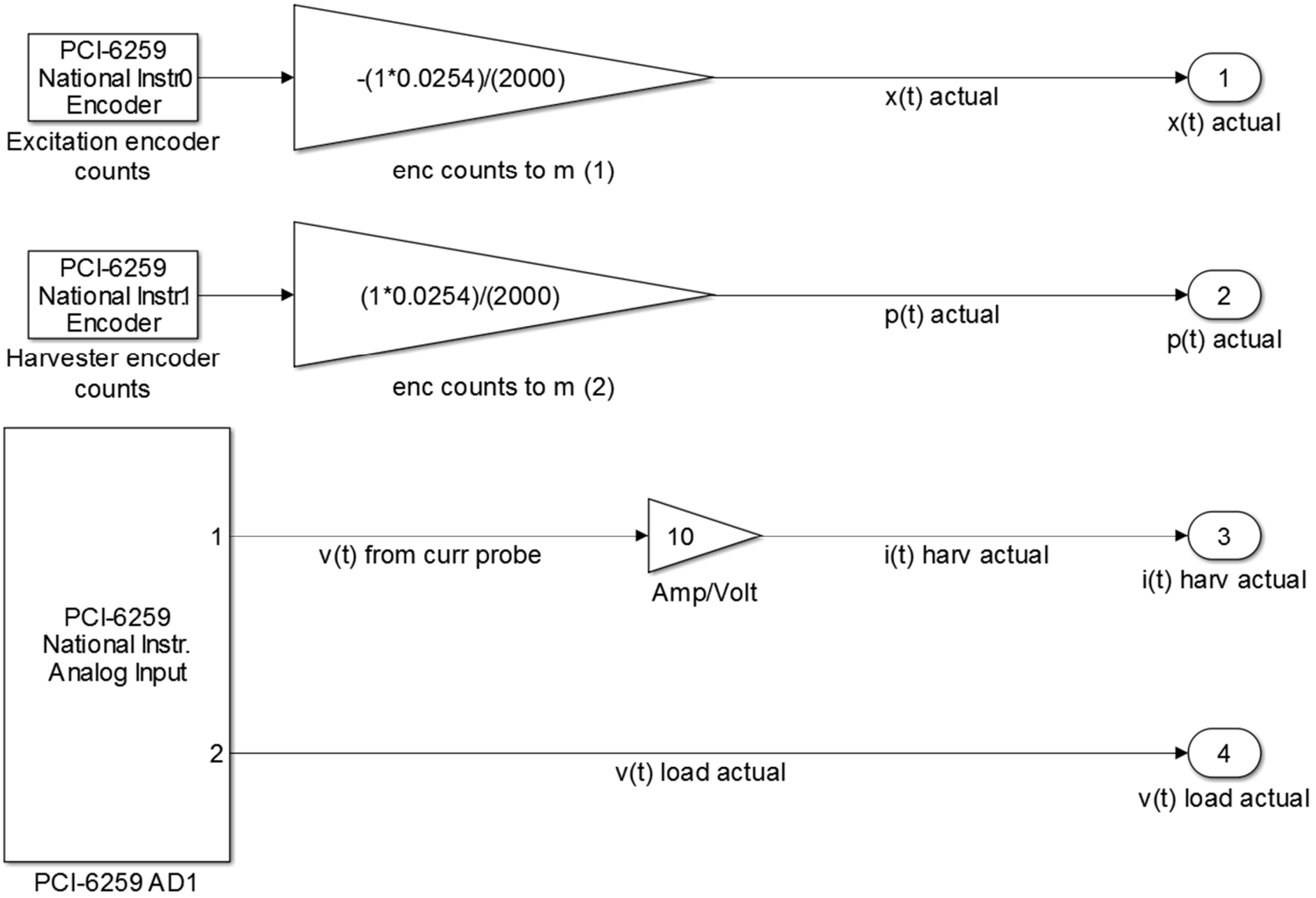

Figure 65: Analog Inputs subsystem

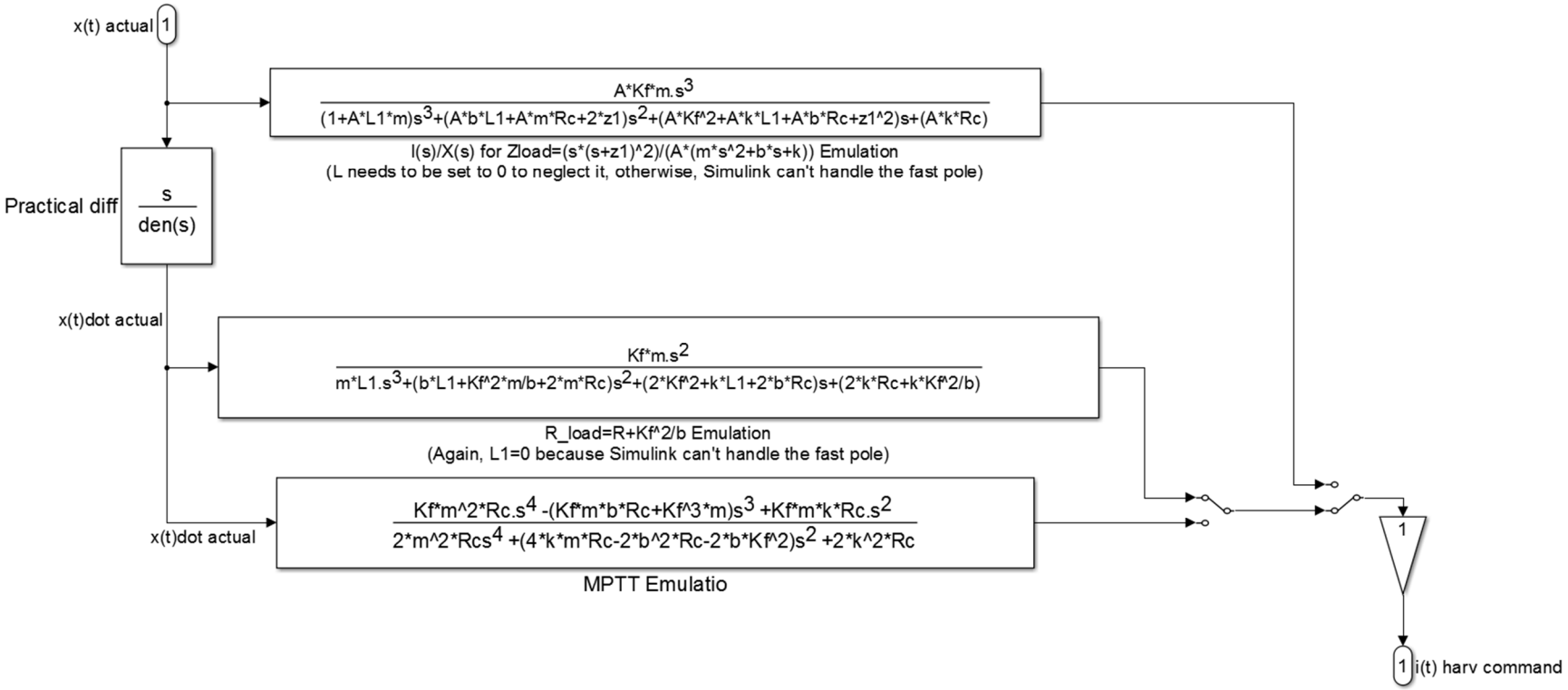

Figure 66: Active harvester loads and servo amp emulation of electrical loads subsystem

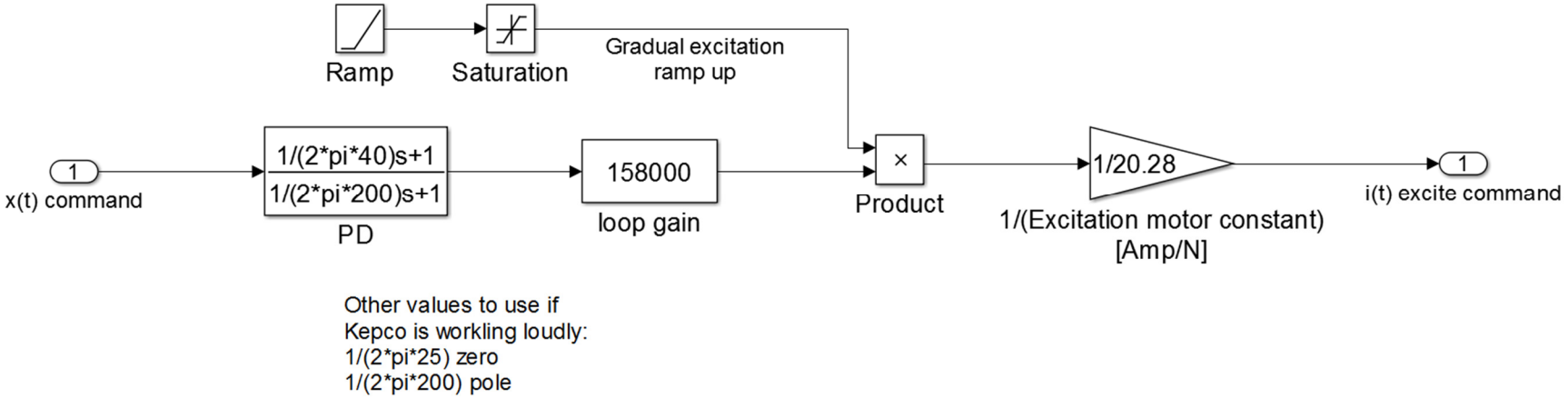

Figure 67: Position to servo amp control subsystem

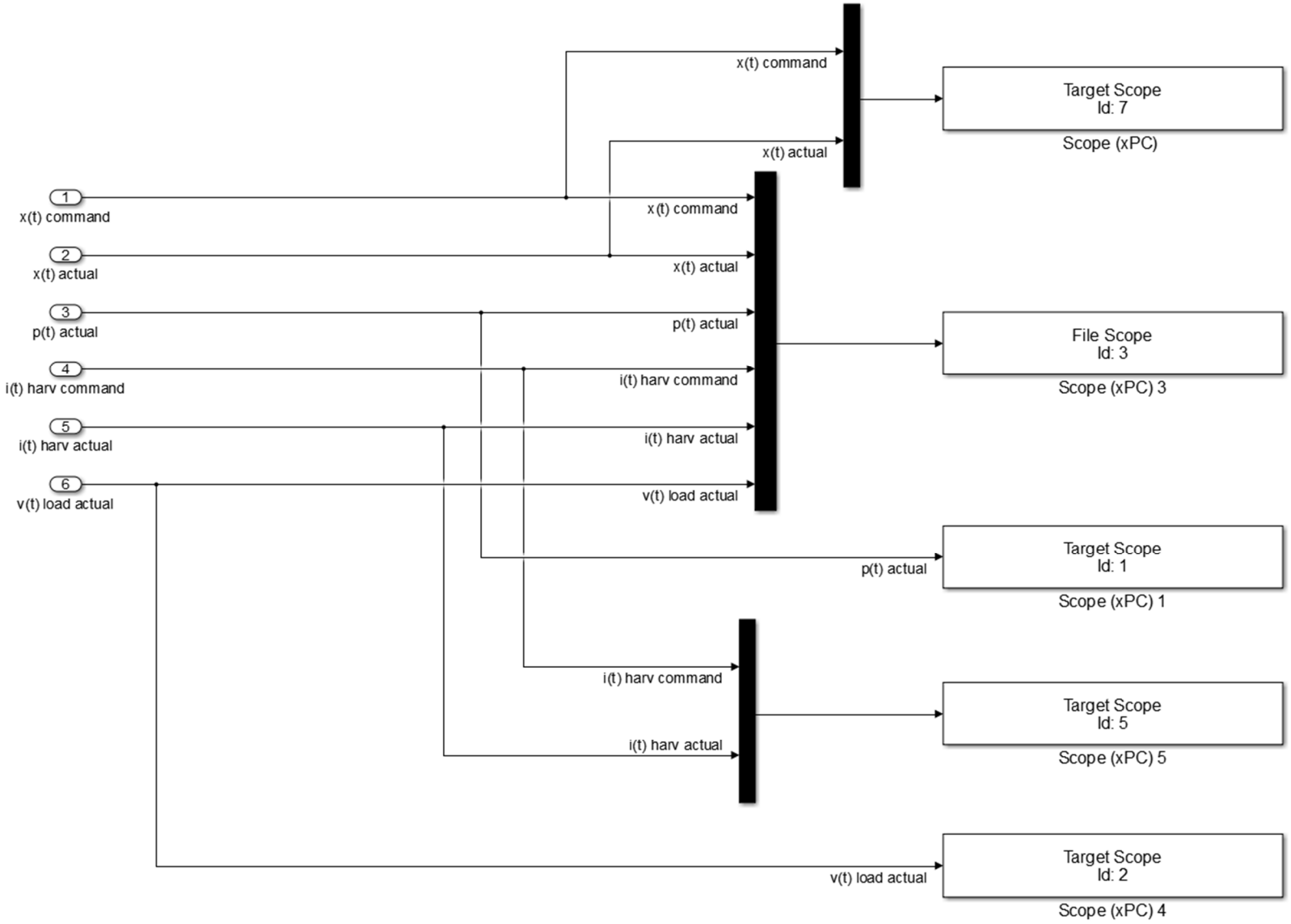

Figure 68: Data logging and scope display subsystem

2. *MATLAB Code*

2.1. Code for Running Experimental Setup Simulink and Analyzing Results

```
close all;
clear all;
%% DEFINING NON-CHANGING SYSTEM PARAMETERS

s=tf('s');              % Laplace domain s

m=0.698;                % Proof mass [kg]
b=7.060;                % Parasitic mechanical viscous damping [N/(m/s)]
k=1629;                 % Equivalent linear stiffness [N/m]
wn=sqrt(k/m);           % Natural freq of harv [rads/s]

% % New properties with clamps on
% m=0.766;              % Proof mass [kg]
% b=7.974;              % Parasitic mechanical viscous damping [N/(m/s)]
% k=3575.7;             % Equivalent linear stiffness [N/m]
% wn=sqrt(k/m);         % Natural freq of harv [rads/s]

Kf=17.8;                % Motor constant [N/A] or [V/(m/s)]
L=0.0031;               % Voic coil inductance [H]
L1=0;                   % Control law for Zload(s)=s*(s+z1)^2/(A*(m*s^2+b*s+k)) requires L=0 to be
stable
Rc=7;                   % Parasitic electrical resistance of the voice coil [Ohm]
R_load=Rc+Kf^2/b;       % Ideal load resistance to attach for passive case [Ohm]

Lc=0.0031;              % Voice coil inductance [H], neglected in many calculations as its contribution is
negligible in our frequency range of interest


% values from optimization routine for trial electrical load
z1=60;
A=20;


Zsource=Kf^2*s/(m*s^2+b*s+k)+L*s+Rc;    % Equivalent electrical source impedance
ZMPTT=Rc-L*s-Kf^2*s/(m*s^2-b*s+k);      % Load impedance dictated by MPTT


%% DEFINING PARTICULAR RUN PARAMETERS
% NOTE: excitation tuned to be 1 m/s^2 regardless of input frequency
freq=2;                 % Frequency to run excitation at

% PID constants
P=100;                  % Proportional gain
I=2;                    % Integrator gain
D=10;                   % Differentiator gain
tau_diff=1/(2*pi*100);      % Differentiator filter time constant
```

```
tau_leaky=1/(2*pi*0.3);     % Leaky integrator time constant

% Low-pass filter parameters for double differentiation of excitation
dd_filt=s^2/(s/(2*pi*250)+1)^4;
[num_dd_filt den_dd_filt]=tfdata(dd_filt);
num_dd_filt=num_dd_filt{1};
den_dd_filt=den_dd_filt{1};

close all

% CHOOSE A SAMPLING RATE AND SIMULATION TIME ****************************
% sampling=0.0002;
% sampling=1/2560;       % Use with actual Stones River bridge data
sampling=1/5120;       % Use with Bob Sheehan Memorial Bridge (greenway data)

% sim_time=120;             % For chirp test/parameter characterization
% sim_time=300;            % To use with 300 sec data sets (I-40 overpass 10-14)
% sim_time=405;             % To use with 405 sec data sets (Korean bridge 6-10)
sim_time=60;              % To use with 60 sec data sets (I-40 overpass 6-9)
% sim_time=1500;            % To use with 25 min data set (all I-40 overpass 5 min runs combined)
% sim_time=10;              % To use with 10 sec Bob Sheehan Memorial Bridge (greenway data)
% ************************************************************************

% Creating a smooth frequency step-up simulation input and using FFT to
% show how we have segments of discrete frequencies (USE WITH SIM_TIME=100)
time=[0:sampling:sim_time];
test_freqs=[3 4 5 6 7 7.4 7.8 8.2 8.8 9 10 11 12];

% CHOOSE number of cylces to run at each frequency **********************
% num_cycles=50;
num_cycles=1;
% ************************************************************************

input=[];
input_time=[];
for xx=1:1:length(test_freqs)
   input_time_new=time(1:floor((num_cycles/test_freqs(xx))*(1/sampling)));
   input_time=[input_time,input_time_new];
   input_new=0.002*sin(test_freqs(xx)*2*pi*time(1:floor((num_cycles/test_freqs(xx))*(1/sampling))));
   input=[input,input_new];
end

[peaks,locs]=findpeaks(input_time);
locs=[locs,length(input_time)];

ss=1/sampling;

for xx=0:1:length(locs)-1;
   if xx==0
      x_var=time(1:locs(1));
      y_var=input(1:locs(1));
```

```
    else
        x_var=input_time(locs(xx):locs(xx+1));
        y_var=input(locs(xx):locs(xx+1));
        x_var(1)=[];
        y_var(1)=[];
    end



%         figure;
%         subplot(2,1,1,'FontSize',16)
%         plot(x_var,y_var);
%         grid on;
%         xlabel('Time [sec]');
%         ylabel('Amplitude');
%         title('Free response of the harvester');
%         c=fft(y_var);
%         c(1)=[];
%         n=length(c);
%         % power=abs(c(1:floor(n/2))).^2;
%         mag=abs(c(1:floor(n/2)))*2/(n+1);
%         nyquist=1/2;
%         freq=((1:n/2))/((n/2))*nyquist*ss;
%
%
%         subplot(2,1,2,'FontSize',16)
%         plot(freq,mag);
%         grid on;
%         xlabel('Freq [Hz]');
%         ylabel('Amplitude');
%
end
% % Plotting frequency step-up input to use for experimentation (resulting
% % from above)
% plot(time(1:length(input)),input);
% ************************************************************************

% Loading Realistic bridge excitation off of Stones River Bridge
%Enter directory where data lives:
% directory='C:\Users\Alex Pedchenko\Desktop\Work\Energy Harvester\Real Bridge Data\Stones River
Greenway Data collected on July 2nd, 2015\';
directory='C:\Users\Alex Pedchenko\Desktop\Work\Energy Harvester\Real Bridge Data\Long runs with
Janette\BroadwayBridge\';
% directory='C:\Users\Alex Pedchenko\Desktop\Work\Energy Harvester\Real Bridge Data\Long runs
with Janette\KoreanMemorialBridge\';
% INPUT: FILE CONTAINING BRIDGE DISPLACEMENT FOR EXPERIMENTAL RUN AND
% CORRESPONDING REAL BRIDGE ACCELERATION DATA FILE**************************
% file_name='10mphleft_001';
% file_name='10mphleft_002';
% file_name='10mphright_002';
% file_name='20mphleft_001';
```

```
% file_name='20mphleft_002';
% file_name='20mphright_001';
% file_name='20mphright_002';
% file_name='30mphright_002';
% file_name='30mphright_003';

% file_name='dOct27a_Real_bridge_40overpass_data13.mat';
file_name='dOct27a_Real_bridge_40overpass_data9.mat';
% file_name='dOct28a_Real_bridge_40overpass_data14.mat';
% file_name='dOct28a_Real_bridge_40overpass_data8.mat';
% file_name='dOct28a_Real_bridge_Korean_data8.mat';
% file_name='dOct28a_Real_bridge_40overpass_data10.mat';
% file_name='dOct28a_Real_bridge_40overpass_data11.mat';
% file_name='dOct29a_Real_bridge_40overpass_data12.mat';
% file_name='dNov072015a_Real_bridge_40overpass_15min.mat'
% ********************************************************************

% INPUT: Choose which bridge data to process ****************************

% % (Stones Greenway data only) ***************************************
% % sensor_num=1;
% sensor_num=2;
% % sensor_num=3;
%
% load([directory '\dAug18a_Real_bridge_' file_name '_sens' num2str(sensor_num) '.mat'])
% time_exper=t;
% disp_exper=avg_disp_exper';
% % ********************************************************************

% I-40/I-65 or Korean bridge data only *********************************
load([directory file_name])
time_exper=t;
disp_exper=avg_disp_exper';
% ********************************************************************

% CHOOSE ELECTRICAL LOAD ATTACHED ACROSS HARVESTER LEADS
******************
% Rsimul=8.51;       % Ideal for 3 Hz
% Rsimul=10.22;      % Ideal for 4 Hz
% Rsimul=13.42;      % Ideal for 5 Hz
% Rsimul=20.23;      % Ideal for 6 Hz
% Rsimul=37.04;      % Ideal for 7 Hz
% Rsimul=47.51;      % Ideal for 7.4 Hz
% Rsimul=52.68;      % Ideal for 7.8 Hz
% Rsimul=46.79;      % Ideal for 8.2 Hz
% Rsimul=33.78;      % Ideal for 8.8 Hz
% Rsimul=30.53;      % Ideal for 9 Hz
% Rsimul=20.45;      % Ideal for 10 Hz
% Rsimul=15.88;      % Ideal for 11 Hz
% Rsimul=13.37;      % Ideal for 12 Hz
% Rsimul=50;
```

```
% Rsimul=52.7;
% Rsimul=23.6;
% Rsimul=26.5;
% Rsimul=100;
% Rsimul=20;
% Rsimul=20.3;
% Rsimul=19.7;
% Rsimul=48.7;
% Rsimul=48.4;
Rsimul=Rc+Kf^2/b;

% Csimul=300*10^-6;
% Csimul=280*10^-6;
% Csimul=240*10^-6;
% Csimul=240*10^-6;
% ************************************************************************
%% GRABBING DATA OFF OF XPC MACHINE
close all
f=xpctarget.fs;

h=fopen(f,'C:\Data.dat');   % Use with 'sJul0714b_table_top_setup_Rloadsimul_currprobe.slx'

data=fread(f,h);
fclose(f,h);

x=readxpcfile(data);
t_exper=x.data(:,length(x.data(1,:)));  % Simulation time [sec]
x_enc=x.data(:,2);                  % Bridge position from encoder (m)
x_ref=x.data(:,1);                  % Desired bridge position (m)
p_enc=x.data(:,3);                  % Relative harvester position from encoder (m)
v_load=x.data(:,6);                 % Actual load voltage (V)
i_probe=x.data(:,5);                % Current from inductive probe [A]
i_command=x.data(:,4);              % Command current for harvester active load control [A]
%% CALCULATING POWER FROM EXPERIMENTAL DATA AND COMPARING RESULTS TO
PHR
close all


i_load=i_probe;

% CHOOSE: a way to process experimentally recorded current ***************

% Method 1
i_load=i_probe-mean(i_probe);   % Simply subtracting DC component

% Method 2
% Filtfilting the current to get rid of suspected drift on current probe
% (i.e., DC drift over time that simply subtracting the average of
% current does not get rid of)
leaky_int=((s/(2*pi*1)/(s/(2*pi*1)+1)));
leaky_int_dig=c2d(leaky_int,t_exper(2)-t_exper(1));
```

```
[B_dig,A_dig]=tfdata(leaky_int_dig);
B_dig=B_dig{1};
A_dig=A_dig{1};
i_load=filtfilt(B_dig,A_dig,i_probe);

% plot(t_exper,i_load,t_exper,i_load_filtfilt);
% ************************************************************************

% Experimentally measured average power
Pow_inst=v_load.*i_load;          % Instantaneous power
Pow_avg=mean(Pow_inst);                  % Average power

% Theoretical avg power generation calculations (using PHR)

% FFT of the input excitation

v=x_enc;    % measured excitation displacement [m]
time_DFT=t_exper;       % time [s]

% Showing excitation displacement and FFT thereof
figure;
subplot(2,1,1,'FontSize',16)
plot(time_DFT,v*1000);      % Multiplied by 1000 to show results in [mm]
grid on;
xlabel('Time [sec]');
ylabel('Amplitude [mm]');
title('Free response of the harvester');
c=fft(v);
c(1)=[];
n=length(c);
mag=abs(c(1:floor(n/2)))*2/(n+1);
nyquist=1/2;
freq=((1:n/2))/((n/2))*nyquist*ss;
subplot(2,1,2,'FontSize',16)
plot(freq,mag*1000);       % Multiplied by 1000 to show results in [mm]
grid on;
xlabel('Freq [Hz]');
ylabel('Amplitude [mm]');


% INPUT: From FFT, pick a minimal frequency range which has significant
% magnitude contributions to the FFT ************************************
freq_range=freq(1:30/(freq(2)-freq(1)));   % PHR*FFT up to this frequency will be used to find total
power generated
w=freq_range*2*pi;      % Freq range in radians
accel_mag_sq=(mag(1:length(freq_range))'.*w.^2).^2; % Accel DFT squared
% ************************************************************************

% CODE FOR PHR CALCULATIONS ***********************************************

% INPUT: What was the used electrical load
```

```
% ************************************************************************
% Zservo=tf(Rsimul+1/(Csimul*s));
Zservo=tf([Rsimul],[1]);
% Zservo=s*(s+z1)^2/(A*(m*s^2+b*s+k));
% ************************************************************************

% Internal harvester dynamics
Zsource=Kf^2*s/(m*s^2+b*s+k)+L*s+Rc;    % Thevenin equivalent source impedance
Zmech=tf([Kf*m 0],[m b k]);             % Accel to Vexo TF


[magZs phaseZs]=bode(Zsource,w);
magZs=squeeze(magZs);
phaseZs=squeeze(phaseZs);
[magZservo phaseZservo]=bode(Zservo,w);
magZservo=squeeze(magZservo);
phaseZservo=squeeze(phaseZservo);
[magCL phaseCL]=bode(Zservo/(Zsource+Zservo)*Zmech,w);
magCL=squeeze(magCL);
phaseCL=squeeze(phaseCL);

% PHR equations expressed as logarithms
logphr=-log10(magZservo)+2*log10(magCL);
phr=0.5*10.^(logphr).*cos(phaseZservo*pi/180);   % Final PHR form W/(m/s^2)^2
phr=phr';
theor_avg_pow=sum(phr.*accel_mag_sq);

figure
[hAx,hLine1,hLine2] = plotyy(w./(2*pi),phr,w./(2*pi),accel_mag_sq)
title('Theoretical PHR');
xlabel('Freq [Hz]')
ylabel(hAx(1),'PHR [W/(m/s^2)^2]');
ylabel(hAx(2),'(Accel DFT)^2 [(m/s^2)^2]');


display(['Experimental avg pow generation = ',num2str(Pow_avg),' W']);
display(['Theoretical avg pow generation = ',num2str(theor_avg_pow),' W']);
display(['Error = ',num2str(100*(theor_avg_pow-Pow_avg)/Pow_avg),' %']);
```

2.2 Code for Comparing Power Outputs of the Three Architectures and Their Three Embodiments

```
close all;
clear all;

%% Loading real data to use as excitation
load(['C:\Users\Alex Pedchenko\Desktop\Work\Energy Harvester\DISSERTATION MATERIAL\Final
Defense\Matlab associated files\Idealistic excitation
cases\dNov082015a_Real_bridge_25min_I40_data']);

s=tf('s');
v=accel_long;                    % measured excitation accel [m/s^2]
time_DFT=time_long;              % time [s]
ss=1/(time_DFT(2)-time_DFT(1));     % sampling rate [Hz]

% Showing excitation displacement and FFT thereof
figure;
subplot(2,1,1,'FontSize',16)
plot(time_DFT,v,'k');
grid on;
xlabel('Time [sec]');
ylabel('Accel Amp [m/s^2]');
c=fft(v);
c(1)=[];
n=length(c);
mag=abs(c(1:floor(n/2)))*2/(n+1);
nyquist=1/2;
freq=((1:n/2))/((n/2))*nyquist*ss;

% INPUT: From FFT, pick a minimal frequency range which has significant
% magnitude contributions to the FFT
freq_range=freq(1:30/(freq(2)-freq(1)));   % PHR*(DFT of accel^2) up to
% this frequency will be used to find total power generated
w=freq_range*2*pi;  % Freq range in radians/s
accel_mag_sq=(mag(1:length(freq_range)).^2); % DFT of accel^2
% ************************************************************************

subplot(2,1,2,'FontSize',16)
plot(freq_range,(mag(1:length(freq_range))),'k');
grid on;
xlabel('Freq [Hz]');
ylabel('Accel amplitude [m/s^2]');

hold on
%% ************************************************************************
% BASIC TUNING CONVENTIONAL HARVESTER ************************************

m=0.697*2;              % Proof mass [kg]
k=(10.77*2*pi)^2*m;     % Stiffness [N/m]
b=7.294;                % Damping [N/(m/s)]
```

```
% Electrical parameters of EM harvester
Kf=17.8;              % Motor constant [N/A] or [V/(m/s)]
R=7;                 % Coil resistance [Ohms]
L=0.0031;             % Coil inductance [H]

% PHR TFs
Zservo=tf([R+Kf^2/b],[1]);
Zsource=L*s+R+Kf^2*s/(m*s^2+b*s+k);
Zmech=tf([Kf*m 0],[m b k]);

% PHR method
[magZs phaseZs]=bode(Zsource,w);
magZs=squeeze(magZs);
phaseZs=squeeze(phaseZs);
[magZservo phaseZservo]=bode(Zservo,w);
magZservo=squeeze(magZservo);
phaseZservo=squeeze(phaseZservo);
[magCL phaseCL]=bode(Zservo/(Zsource+Zservo)*Zmech,w);
magCL=squeeze(magCL);
phaseCL=squeeze(phaseCL);
logphr=-log10(magZservo)+2*log10(magCL);
phr=0.5*10.^(logphr).*cos(phaseZservo*pi/180);
phrconv=phr';                    % Conv harv conv tuned curve

Powconv=sum(phrconv.*accel_mag_sq); % Total power generated for conv tuned
% conv harv
% ************************************************************************
% ************************************************************************

%% ************************************************************************
% MPTT CONV HARVESTER (PHYSICALLY UNACHIEVABLE)**************************

% Enter vectors to search
k_vector=([11.3]*2*pi).^2*m;

Operations=length(k_vector)
counter=0;
theor_avg_pow=zeros(1,length(k_vector));

%% Begin optimization
tic;
for index1=1:1:length(k_vector)
   k=k_vector(index1);

   ZservoMPTT=-L*s+R-Kf^2*s/(m*s^2-b*s+k);
   Zsource=L*s+R+Kf^2*s/(m*s^2+b*s+k);
   Zmech=tf([Kf*m 0],[m b k]); % to get per m/Sec^2

   % PHR method
   w=freq_range*2*pi;
```

```
    [magZs phaseZs]=bode(Zsource,w);
    magZs=squeeze(magZs);
    phaseZs=squeeze(phaseZs);
    [magZservo phaseZservo]=bode(ZservoMPTT,w);
    magZservo=squeeze(magZservo);
    phaseZservo=squeeze(phaseZservo);
    [magCL phaseCL]=bode(ZservoMPTT/(Zsource+ZservoMPTT)*Zmech,w);
    magCL=squeeze(magCL);
    phaseCL=squeeze(phaseCL);
    logphr=-log10(magZservo)+2*log10(magCL);
    phrmptt=0.5*10.^(logphr).*cos(phaseZservo*pi/180);
    phrmptt=phrmptt';

    theor_avg_pow(index1)=sum(phrmptt.*accel_mag_sq);

    counter=counter+1;
    if mod(counter,50)==0
       display(['Approx ' num2str(toc/(counter/Operations)-toc) ' sec remaining.'])
    end
end

%% RECORDING AND DISPLAYING RESULTS OF OPTIMIZATION
Powmptt=max(theor_avg_pow)  % Total power generated for conv harv mptt
[k_index] = ind2sub(size(theor_avg_pow),find(theor_avg_pow == Powmptt));
k_idealmptt=k_vector(k_index);  % Stiffness that yields above max power

display(['Conv. Harvester with MPTT Load Results']);
display(['m is ' num2str(m)]);
display(['k should be ' num2str(k_idealmptt)]);
display(['This makes the natural frequency ' num2str(sqrt(k_idealmptt/m)/(2*pi)) ' Hz']);
display(['b is ' num2str(b)]);
display('Zload should be Zsource*');
display(['MPTT-dictated load would yield ' num2str(1000*Powmptt) ' mW from the excitation']);
display(['End of Conv.Harvester with MPTT Load Results']);

% PHR that yields the most power
ZservoMPTT=-L*s+R-Kf^2*s/(m*s^2-b*s+k_idealmptt);
Zsource=L*s+R+Kf^2*s/(m*s^2+b*s+k_idealmptt);
Zmech=tf([Kf*m 0],[m b k_idealmptt]); % to get per m/Sec^2

% PHR method
w=freq_range*2*pi;
[magZs phaseZs]=bode(Zsource,w);
magZs=squeeze(magZs);
phaseZs=squeeze(phaseZs);
[magZservo phaseZservo]=bode(ZservoMPTT,w);
magZservo=squeeze(magZservo);
phaseZservo=squeeze(phaseZservo);
[magCL phaseCL]=bode(ZservoMPTT/(Zsource+ZservoMPTT)*Zmech,w);
magCL=squeeze(magCL);
phaseCL=squeeze(phaseCL);
```

```
logphr=-log10(magZservo)+2*log10(magCL);
phrmptt=0.5*10.^(logphr).*cos(phaseZservo*pi/180);
phrmpttconv=phrmptt';   % Conv harv mptt curve

% ************************************************************************
% ************************************************************************

%% ************************************************************************
% PHR-TUNED CONV HARVESTER ************************************************

m=0.697*2; % Optimizing for set mass
b=7.294;

% Enter vectors to search
k_vector=([11.4]*2*pi).^2*m;
RL_vector=[32.5];

% Electrical parameters of EM harvester
Kf=17.8;
R=7;
L=0.0031;

Operations=length(RL_vector)*length(k_vector)
display(['RL vector length is ' num2str(length(RL_vector))]);
display(['k vector length is ' num2str(length(k_vector))]);
counter=0;

theor_avg_pow=zeros(length(RL_vector)*length(k_vector));
%% Running optimization
tic;
for index1=1:1:length(RL_vector)
        RL=RL_vector(index1);
        for index2=1:1:length(k_vector)
           k=k_vector(index2);

              Zsource_new=L*s+R+Kf^2*s/(m*s^2+b*s+k);
              Zmech_new=Kf*m*s/(m*s^2+b*s+k);
              Zload_new=tf(RL,1);

              % PHR method
              w=freq_range*2*pi;
              [magZs phaseZs]=bode(Zsource_new,w);
              magZs=squeeze(magZs);
              phaseZs=squeeze(phaseZs);
              [magZservo phaseZservo]=bode(Zload_new,w);
              magZservo=squeeze(magZservo);
              phaseZservo=squeeze(phaseZservo);
              [magCL phaseCL]=bode(Zload_new/(Zsource_new+Zload_new)*Zmech_new,w);
              magCL=squeeze(magCL);
              phaseCL=squeeze(phaseCL);
```

```
            logphr=-log10(magZservo)+2*log10(magCL);
            phrnew=0.5*10.^(logphr).*cos(phaseZservo*pi/180); % avg power ratio to excitation
W/(m/s^2)^2
            phrnew=phrnew';

            theor_avg_pow(index1,index2)=sum(phrnew.*accel_mag_sq);

            counter=counter+1;
            if mod(counter,50)==0
               display(['Approx ' num2str(toc/(counter/Operations)-toc) ' sec remaining.'])
            end
        end
end
%% RECORDING RESULTS OF OPTIMIZATION AND DISPLAYING/PLOTTING RESULTS
******
Powmaxconv=max(max(theor_avg_pow))  % Max pow for PHR-tuned conv harv
[RL_index,k_index] = ind2sub(size(theor_avg_pow),find(theor_avg_pow == Powmaxconv));
RL_idealconv=RL_vector(RL_index);   % Resistance that yields above max pow
k_idealconv=k_vector(k_index);      % Stiffness that yields above max pow

display(['Conventional Harvester Tuning Results']);
display(['m is ' num2str(m)]);
display(['k should be ' num2str(k_idealconv)]);
display(['This makes the natural frequency ' num2str(sqrt(k_idealconv/m)/(2*pi)) ' Hz']);
display(['b is ' num2str(b)]);
display(['Rload should be ' num2str(RL_idealconv)]);
display(['PHR-tuned would yield ' num2str(1000*Powmaxconv) ' mW from the excitation']);
display(['Conventional tuning would yield ' num2str(1000*Powconv) ' mW from the excitation']);
display(['MPTT-dictated load would yield ' num2str(1000*Powmptt) ' mW from the excitation']);
display(['End of Conventional Harvester Tuning Results']);

% PHR that yields the most power
Zsource_new=L*s+R+Kf^2*s/(m*s^2+b*s+k_idealconv);
Zmech_new=Kf*m*s/(m*s^2+b*s+k_idealconv);
Zload_new=tf(RL_idealconv,1);

% PHR method
w=freq_range*2*pi;
[magZs phaseZs]=bode(Zsource_new,w);
magZs=squeeze(magZs);
phaseZs=squeeze(phaseZs);
[magZservo phaseZservo]=bode(Zload_new,w);
magZservo=squeeze(magZservo);
phaseZservo=squeeze(phaseZservo);
[magCL phaseCL]=bode(Zload_new/(Zsource_new+Zload_new)*Zmech_new,w);
magCL=squeeze(magCL);
phaseCL=squeeze(phaseCL);

logphr=-log10(magZservo)+2*log10(magCL);
phrnew=0.5*10.^(logphr).*cos(phaseZservo*pi/180);
phrmaxconv=phrnew';     % PHR-tuned conv harv curve
```

```
%% Plot ALL results for Conventional Harvester with different loads
% p. 58 of Lab Notebook 6
figure
[hAx, PHR_plot, DFT_plot] = plotyy(freq_range,phrconv,freq_range,accel_mag_sq);
hold on;
grid on;
xlabel('Freq [Hz]');
ylabel(hAx(1),'PHR [W/(m/s^2)^2]');
ylabel(hAx(2),'Acceleration Amplitude Squared [m/s^2]^2');
hold on;
plot(freq_range,phrmpttconv,'k');
plot(freq_range,phrmaxconv,'r');
legend('Conventional','MPTT','PHR-guided');
set(hAx(1),'XLim',[0 25]);
set(hAx(2),'XLim',[0 25]);
set(hAx(1),'YLim',[0 0.03]);
%% Summary of total power results for conventional harvester
display(['PHR-tuned conv harv would yield ' num2str(1000*Powmaxconv) ' mW from the excitation']);
display(['Basic tuning of conv harv would yield ' num2str(1000*Powconv) ' mW from the excitation']);
display(['MPTT conv harv would yield ' num2str(1000*Powmptt) ' mW from the excitation']);
%% ************************************************************************
% BASIC TUNING OF HARVESTER ARRAY ***************************************

m1=0.697;
m2=0.697;
b1=7.294;
b2=7.294;

% Below values are set for conventional tuning/basic embodiment
k1_vector=([3.039]*2*pi).^2*m1;
k2_vector=([10.77]*2*pi).^2*m2;
RL1_vector=[R+Kf^2/b1];
RL2_vector=[R+Kf^2/b2];

Operations=length(RL1_vector)*length(RL2_vector)*length(k1_vector)*length(k2_vector);
display(['RL1 vector length is ' num2str(length(RL1_vector))]);
display(['RL2 vector length is ' num2str(length(RL2_vector))]);
display(['k1 vector length is ' num2str(length(k1_vector))]);
display(['k2 vector length is ' num2str(length(k2_vector))]);
counter=0;

theor_avg_pow=zeros(length(RL1_vector),length(RL2_vector),length(k1_vector),length(k2_vector));
%% Running optimization
for index1=1:1:length(RL1_vector)
   RL1=RL1_vector(index1);
   for index2=1:1:length(RL2_vector)
      RL2=RL2_vector(index2);
      for index3=1:1:length(k1_vector)
         k1=k1_vector(index3);
         for index4=1:1:length(k2_vector)
```

```
            k2=k2_vector(index4);

            Zservo1=tf(RL1,1);
            Zsource1=L*s+R+Kf^2*s/(m1*s^2+b1*s+k1);
            Zmech1=tf([Kf*m1 0],[m1 b1 k1]);

            Zservo2=tf(RL2,1);
            Zsource2=L*s+R+Kf^2*s/(m2*s^2+b2*s+k2);
            Zmech2=tf([Kf*m2 0],[m2 b2 k2]);

            % PHR method for 1st harvester of array avg pow gen
            w=freq_range*2*pi;
            [magZs phaseZs]=bode(Zsource1,w);
            magZs=squeeze(magZs);
            phaseZs=squeeze(phaseZs);
            [magZservo phaseZservo]=bode(Zservo1,w);
            magZservo=squeeze(magZservo);
            phaseZservo=squeeze(phaseZservo);
            [magCL phaseCL]=bode(Zservo1/(Zsource1+Zservo1)*Zmech1,w);
            magCL=squeeze(magCL);
            phaseCL=squeeze(phaseCL);
            logphr=-log10(magZservo)+2*log10(magCL);
            phr1=0.5*10.^(logphr).*cos(phaseZservo*pi/180);
            phr1=phr1';

            % PHR method for 2nd harvester of array avg pow gen
            [magZs phaseZs]=bode(Zsource2,w);
            magZs=squeeze(magZs);
            phaseZs=squeeze(phaseZs);
            [magZservo phaseZservo]=bode(Zservo2,w);
            magZservo=squeeze(magZservo);
            phaseZservo=squeeze(phaseZservo);
            [magCL phaseCL]=bode(Zservo2/(Zsource2+Zservo2)*Zmech2,w);
            magCL=squeeze(magCL);
            phaseCL=squeeze(phaseCL);
            logphr=-log10(magZservo)+2*log10(magCL);
            phr2=0.5*10.^(logphr).*cos(phaseZservo*pi/180);
            phr2=phr2';

            phrnew=phr1+phr2;
            theor_avg_pow(index1,index2,index3,index4)=sum(phrnew.*accel_mag_sq);

            counter=counter+1;
            if mod(counter,50)==0
               display(['Approx ' num2str(toc/(counter/Operations)-toc) ' sec remaining.'])
            end
         end
      end
   end
end
%% Recording results of optimization and plotting phr
```

```
Powarray=max(max(max(max(theor_avg_pow))))  % Total pow for conv tuning of harv array
[RL1_index,RL2_index,k1_index,k2_index] = ind2sub(size(theor_avg_pow),find(theor_avg_pow ==
Powarray));
RL1_array=RL1_vector(RL1_index);
RL2_array=RL2_vector(RL2_index);
k1_array=k1_vector(k1_index);
k2_array=k2_vector(k2_index);

display(['Conventional Array Results']);
display(['m1 is ' num2str(m1)]);
display(['m2 is ' num2str(m2)]);
display(['k1 is ' num2str(k1_array)]);
display(['k2 is ' num2str(k2_array)]);
display(['This makes the 1st natural frequency ' num2str(sqrt(k1_array/m1)/(2*pi)) ' Hz']);
display(['This makes the 2nd natural frequency ' num2str(sqrt(k2_array/m2)/(2*pi)) ' Hz']);
display(['b1 is ' num2str(b1)]);
display(['b2 is ' num2str(b1)]);
display(['Rload_1 is ' num2str(RL1_array)]);
display(['Rload_2 is ' num2str(RL2_array)]);
display(['Conv. array would yield ' num2str(1000*Powarray) ' mW from the excitation']);
display(['End of Conventional Array Results']);

% PHR that yields the most power
Zservo1=tf(RL1_array,1);
Zsource1=L*s+R+Kf^2*s/(m1*s^2+b1*s+k1_array);
Zmech1=tf([Kf*m1 0],[m1 b1 k1_array]);

Zservo2=tf(RL2_array,1);
Zsource2=L*s+R+Kf^2*s/(m2*s^2+b2*s+k2_array);
Zmech2=tf([Kf*m2 0],[m2 b2 k2_array]);

% PHR method for 1st harvester of array avg pow gen
w=freq_range*2*pi;
[magZs phaseZs]=bode(Zsource1,w);
magZs=squeeze(magZs);
phaseZs=squeeze(phaseZs);
[magZservo phaseZservo]=bode(Zservo1,w);
magZservo=squeeze(magZservo);
phaseZservo=squeeze(phaseZservo);
[magCL phaseCL]=bode(Zservo1/(Zsource1+Zservo1)*Zmech1,w);
magCL=squeeze(magCL);
phaseCL=squeeze(phaseCL);
logphr=-log10(magZservo)+2*log10(magCL);
phr1=0.5*10.^(logphr).*cos(phaseZservo*pi/180);
phr1=phr1';

% PHR method for 2nd harvester of array avg pow gen
[magZs phaseZs]=bode(Zsource2,w);
magZs=squeeze(magZs);
phaseZs=squeeze(phaseZs);
[magZservo phaseZservo]=bode(Zservo2,w);
```

```
magZservo=squeeze(magZservo);
phaseZservo=squeeze(phaseZservo);
[magCL phaseCL]=bode(Zservo2/(Zsource2+Zservo2)*Zmech2,w);
magCL=squeeze(magCL);
phaseCL=squeeze(phaseCL);
logphr=-log10(magZservo)+2*log10(magCL);
phr2=0.5*10.^(logphr).*cos(phaseZservo*pi/180);
phr2=phr2';

phrarray=phr1+phr2;     % Conv tuned harv array PHR curve

% Plot resulting PHR
figure
[hAx, PHR_plot, DFT_plot] = plotyy(freq_range,phrarray,freq_range,accel_mag_sq);
hold on;
grid on;
xlabel('Freq [Hz]');
ylabel(hAx(1),'PHR [W/(m/s^2)^2]');
ylabel(hAx(2),'Accel amplitude^2 [m/s^2]^2');
hold on;
%% ************************************************************************
% PHR-TUNED HARVESTER ARRAY ***********************************************

m1=0.697;
m2=0.697;
b1=7.294;
b2=7.294;

% Enter vectors to search
k1_vector=([3.25]*2*pi).^2*m1;
k2_vector=([11.25]*2*pi).^2*m2;
RL1_vector=[29.6];
RL2_vector=[39];



Operations=length(RL1_vector)*length(RL2_vector)*length(k1_vector)*length(k2_vector)
display(['RL1 vector length is ' num2str(length(RL1_vector))]);
display(['RL2 vector length is ' num2str(length(RL2_vector))]);
display(['k1 vector length is ' num2str(length(k1_vector))]);
display(['k2 vector length is ' num2str(length(k2_vector))]);
counter=0;

theor_avg_pow=zeros(length(RL1_vector),length(RL2_vector),length(k1_vector),length(k2_vector));
%% Running optimization
tic;
for index1=1:1:length(RL1_vector)
   RL1=RL1_vector(index1);
   for index2=1:1:length(RL2_vector)
      RL2=RL2_vector(index2);
      for index3=1:1:length(k1_vector)
```

```
        k1=k1_vector(index3);
        for index4=1:1:length(k2_vector)
            k2=k2_vector(index4);

            Zservo1=tf(RL1,1);
            Zsource1=L*s+R+Kf^2*s/(m1*s^2+b1*s+k1);
            Zmech1=tf([Kf*m1 0],[m1 b1 k1]);

            Zservo2=tf(RL2,1);
            Zsource2=L*s+R+Kf^2*s/(m2*s^2+b2*s+k2);
            Zmech2=tf([Kf*m2 0],[m2 b2 k2]);

            % PHR method for 1st harvester of array avg pow gen
            w=freq_range*2*pi;
            [magZs phaseZs]=bode(Zsource1,w);
            magZs=squeeze(magZs);
            phaseZs=squeeze(phaseZs);
            [magZservo phaseZservo]=bode(Zservo1,w);
            magZservo=squeeze(magZservo);
            phaseZservo=squeeze(phaseZservo);
            [magCL phaseCL]=bode(Zservo1/(Zsource1+Zservo1)*Zmech1,w);
            magCL=squeeze(magCL);
            phaseCL=squeeze(phaseCL);
            logphr=-log10(magZservo)+2*log10(magCL);
            phr1=0.5*10.^(logphr).*cos(phaseZservo*pi/180);
            phr1=phr1';

            % PHR method for 2nd harvester of array avg pow gen
            [magZs phaseZs]=bode(Zsource2,w);
            magZs=squeeze(magZs);
            phaseZs=squeeze(phaseZs);
            [magZservo phaseZservo]=bode(Zservo2,w);
            magZservo=squeeze(magZservo);
            phaseZservo=squeeze(phaseZservo);
            [magCL phaseCL]=bode(Zservo2/(Zsource2+Zservo2)*Zmech2,w);
            magCL=squeeze(magCL);
            phaseCL=squeeze(phaseCL);
            logphr=-log10(magZservo)+2*log10(magCL);
            phr2=0.5*10.^(logphr).*cos(phaseZservo*pi/180);
            phr2=phr2';

            phrnew=phr1+phr2;
            theor_avg_pow(index1,index2,index3,index4)=sum(phrnew.*accel_mag_sq);

            counter=counter+1;
            if mod(counter,50)==0
                display(['Approx ' num2str(toc/(counter/Operations)-toc) ' sec remaining.'])
            end
        end
    end
end
```

```
end
%% Recording results of optimization and plotting phr
Powarraymax=max(max(max(max(theor_avg_pow))));  % Tot power for PHR-tuned harv array
[RL1_index,RL2_index,k1_index,k2_index] = ind2sub(size(theor_avg_pow),find(theor_avg_pow ==
Powarraymax));
% Below resistances and stiffnesses yield total power for PHR-tuned array
RL1_arraymax=RL1_vector(RL1_index);
RL2_arraymax=RL2_vector(RL2_index);
k1_arraymax=k1_vector(k1_index);
k2_arraymax=k2_vector(k2_index);

display(['Conventional Array Results']);
display(['m1 is ' num2str(m1)]);
display(['m2 is ' num2str(m2)]);
display(['k1 is ' num2str(k1_arraymax)]);
display(['k2 is ' num2str(k2_arraymax)]);
display(['This makes the 1st natural frequency ' num2str(sqrt(k1_arraymax/m1)/(2*pi)) ' Hz']);
display(['This makes the 2nd natural frequency ' num2str(sqrt(k2_arraymax/m2)/(2*pi)) ' Hz']);
display(['b1 is ' num2str(b1)]);
display(['b2 is ' num2str(b1)]);
display(['Rload_1 is ' num2str(RL1_arraymax)]);
display(['Rload_2 is ' num2str(RL2_arraymax)]);
display(['Conv. array would yield ' num2str(1000*Powarraymax) ' mW from the excitation']);
display(['End of Conventional Array Results']);


Zservo1=tf(RL1_arraymax,1);
Zsource1=L*s+R+Kf^2*s/(m1*s^2+b1*s+k1_arraymax);
Zmech1=tf([Kf*m1 0],[m1 b1 k1_arraymax]);

Zservo2=tf(RL2_arraymax,1);
Zsource2=L*s+R+Kf^2*s/(m2*s^2+b2*s+k2_arraymax);
Zmech2=tf([Kf*m2 0],[m2 b2 k2_arraymax]);

% PHR method for 1st harvester of array avg pow gen
w=freq_range*2*pi;
[magZs phaseZs]=bode(Zsource1,w);
magZs=squeeze(magZs);
phaseZs=squeeze(phaseZs);
[magZservo phaseZservo]=bode(Zservo1,w);
magZservo=squeeze(magZservo);
phaseZservo=squeeze(phaseZservo);
[magCL phaseCL]=bode(Zservo1/(Zsource1+Zservo1)*Zmech1,w);
magCL=squeeze(magCL);
phaseCL=squeeze(phaseCL);
logphr=-log10(magZservo)+2*log10(magCL);
phr1=0.5*10.^(logphr).*cos(phaseZservo*pi/180);
phr1=phr1';

% PHR method for 2nd harvester of array avg pow gen
[magZs phaseZs]=bode(Zsource2,w);
```

```
magZs=squeeze(magZs);
phaseZs=squeeze(phaseZs);
[magZservo phaseZservo]=bode(Zservo2,w);
magZservo=squeeze(magZservo);
phaseZservo=squeeze(phaseZservo);
[magCL phaseCL]=bode(Zservo2/(Zsource2+Zservo2)*Zmech2,w);
magCL=squeeze(magCL);
phaseCL=squeeze(phaseCL);
logphr=-log10(magZservo)+2*log10(magCL);
phr2=0.5*10.^(logphr).*cos(phaseZservo*pi/180);
phr2=phr2';

phrarraymax=phr1+phr2;  % PHR-tuned harv array PHR curve

plot(freq_range,phrarraymax,'r');
%% ************************************************************************
% MPTT HARV ARRAY W/ MPTT LOAD (PHYSICALLY UNACHIEVABLE) ******************

% Enter vectors to search
k1_vector=([3.3]*2*pi).^2*m1;
k2_vector=([11.25]*2*pi).^2*m2;


Operations=length(k1_vector)*length(k2_vector)
display(['k1 vector length is ' num2str(length(k1_vector))]);
display(['k2 vector length is ' num2str(length(k2_vector))]);
counter=0;

theor_avg_pow=zeros(length(k1_vector),length(k2_vector));
%% Running optimization
tic;
for index1=1:1:length(k1_vector)
   k1=k1_vector(index1);
   for index2=1:1:length(k2_vector)
      k2=k2_vector(index2);

      Zservo1=-L*s+R-Kf^2*s/(m1*s^2-b1*s+k1);
      Zsource1=L*s+R+Kf^2*s/(m1*s^2+b1*s+k1);
      Zmech1=tf([Kf*m1 0],[m1 b1 k1]);

      Zservo2=-L*s+R-Kf^2*s/(m2*s^2-b2*s+k2);
      Zsource2=L*s+R+Kf^2*s/(m2*s^2+b2*s+k2);
      Zmech2=tf([Kf*m2 0],[m2 b2 k2]);

      % PHR method
      [magZs phaseZs]=bode(Zsource1,w);
      magZs=squeeze(magZs);
      phaseZs=squeeze(phaseZs);
      [magZservo phaseZservo]=bode(Zservo1,w);
      magZservo=squeeze(magZservo);
      phaseZservo=squeeze(phaseZservo);
```

```
        [magCL phaseCL]=bode(Zservo1/(Zsource1+Zservo1)*Zmech1,w);
        magCL=squeeze(magCL);
        phaseCL=squeeze(phaseCL);
        logphr=-log10(magZservo)+2*log10(magCL);
        phr1mptt=0.5*10.^(logphr).*cos(phaseZservo*pi/180);
        phr1mptt=phr1mptt';



        % PHR method
        [magZs phaseZs]=bode(Zsource2,w);
        magZs=squeeze(magZs);
        phaseZs=squeeze(phaseZs);
        [magZservo phaseZservo]=bode(Zservo2,w);
        magZservo=squeeze(magZservo);
        phaseZservo=squeeze(phaseZservo);
        [magCL phaseCL]=bode(Zservo2/(Zsource2+Zservo2)*Zmech2,w);
        magCL=squeeze(magCL);
        phaseCL=squeeze(phaseCL);
        logphr=-log10(magZservo)+2*log10(magCL);
        phr2mptt=0.5*10.^(logphr).*cos(phaseZservo*pi/180);
        phr2mptt=phr2mptt';

        phrarraymptt=phr1mptt+phr2mptt;
        theor_avg_pow(index1,index2)=sum(phrarraymptt.*accel_mag_sq);

        counter=counter+1;
        if mod(counter,50)==0
           display(['Approx ' num2str(toc/(counter/Operations)-toc) ' sec remaining.'])
        end

    end
end

%% Recording results of optimization and plotting phr of ALL ARRAY results
% on p. 59
Powarraymptt=max(max(theor_avg_pow)); % Total power generated for mptt harv array
[k1_index,k2_index] = ind2sub(size(theor_avg_pow),find(theor_avg_pow == Powarraymptt));
% Below stiffnesses yield total power for MPTT harv array
k1_arraymptt=k1_vector(k1_index);
k2_arraymptt=k2_vector(k2_index);

display(['MPTT Array Results']);
display(['m1 is ' num2str(m1)]);
display(['m2 is ' num2str(m2)]);
display(['k1 is ' num2str(k1_arraymptt)]);
display(['k2 is ' num2str(k2_arraymptt)]);
display(['This makes the 1st natural frequency ' num2str(sqrt(k1_arraymptt/m1)/(2*pi)) ' Hz']);
display(['This makes the 2nd natural freque              ncy ' num2str(sqrt(k2_arraymptt/m2)/(2*pi)) ' Hz']);
display(['b1 is ' num2str(b1)]);
display(['b2 is ' num2str(b1)]);
```

```
display('Zload1=Zsource1*');
display('Zload2=Zsource2*');
display(['Array with MPTT-dictated loads would yield ' num2str(1000*Powarraymptt) ' mW from the
excitation']);
display(['End of MPTT Array Results']);

plot(freq_range,phrarraymptt,'k');
%% Summary of total power results for harvester array
display(['PHR-tuned array would yield ' num2str(1000*Powarraymax) ' mW from the excitation']);
display(['Basic tuning of harv array would yield ' num2str(1000*Powarray) ' mW from the excitation']);
display(['MPTT harv array would yield ' num2str(1000*Powarraymptt) ' mW from the excitation']);
%% ************************************************************************
% BASIC TUNING OF COUPLED HARVESTER ***************************************

m1=0.697;
m2=0.697;
b1=7.294;
b2=7.294;

% Below values are set for conventional tuning/basic embodiment
k1_vector=([3.039]*2*pi).^2*m1;
k2_vector=([10.77]*2*pi).^2*m2;
RL_vector=[R+Kf^2/b1];

Operations=length(RL_vector)*length(k1_vector)*length(k2_vector);
display(['RL vector length is ' num2str(length(RL_vector))]);
display(['k1 vector length is ' num2str(length(k1_vector))]);
display(['k2 vector length is ' num2str(length(k2_vector))]);
counter=0;

theor_avg_pow=zeros(length(RL_vector),length(k1_vector),length(k2_vector));
%% Running optimization
tic;
for index1=1:1:length(RL_vector)
   RL=RL_vector(index1);
      for index2=1:1:length(k1_vector)
         k1=k1_vector(index2);
         for index3=1:1:length(k2_vector)
            k2=k2_vector(index3);

            Zservo_coup=tf(RL,1);
            psi1=m1*s^2+b1*s+k1;
            psi2=m2*s^2+b2*s+k2;
            Zsource_coup=((L*s+R)*psi1*psi2+Kf^2*s*(psi1+psi2))/(psi1*psi2);
            Zmech_coup=Kf*s*(m2*psi1-m1*psi2)/(psi1*psi2);

            % PHR method for 1st harvester of array avg pow gen
            [magZs phaseZs]=bode(Zsource_coup,w);
            magZs=squeeze(magZs);
            phaseZs=squeeze(phaseZs);
            [magZservo phaseZservo]=bode(Zservo_coup,w);
```

```
            magZservo=squeeze(magZservo);
            phaseZservo=squeeze(phaseZservo);
            [magCL phaseCL]=bode(Zservo_coup/(Zsource_coup+Zservo_coup)*Zmech_coup,w);
            magCL=squeeze(magCL);
            phaseCL=squeeze(phaseCL);
            logphr=-log10(magZservo)+2*log10(magCL);
            phr=0.5*10.^(logphr).*cos(phaseZservo*pi/180);
            phrnew=phr';

            theor_avg_pow(index1,index2,index3)=sum(phrnew.*accel_mag_sq);

            counter=counter+1;
            if mod(counter,50)==0
               display(['Approx ' num2str(toc/(counter/Operations)-toc) ' sec remaining.'])
            end
        end
    end
end

%% Recording results of optimization and plotting phr
Powcoup=max(max(max(theor_avg_pow)))  % Total power generated for basic
% tuning of coupled harv
[RL_index,k1_index,k2_index] = ind2sub(size(theor_avg_pow),find(theor_avg_pow == Powcoup));
% Resistance and stiffnesses values that give total power for basic tuning
% of coupled harv
RL_coup=RL_vector(RL_index);
k1_coup=k1_vector(k1_index);
k2_coup=k2_vector(k2_index);

display(['Coupled Harv Conv. Resistive Load Results']);
display(['m1 is ' num2str(m1)]);
display(['m2 is ' num2str(m2)]);
display(['k1 is ' num2str(k1_coup)]);
display(['k2 is ' num2str(k2_coup)]);
display(['This makes the 1st natural frequency ' num2str(sqrt(k1_coup/m1)/(2*pi)) ' Hz']);
display(['This makes the 2nd natural frequency ' num2str(sqrt(k2_coup/m2)/(2*pi)) ' Hz']);
display(['b1 is ' num2str(b1)]);
display(['b2 is ' num2str(b1)]);
display(['Rload is ' num2str(RL_coup)]);
display(['Conv. array would yield ' num2str(1000*Powcoup) ' mW from the excitation']);
display(['End of Coupled Harv Conv. Resistive Load Results']);

% PHR that yields the most power
Zservo_coup=tf(RL_coup,1);
psi1=m1*s^2+b1*s+k1_coup;
psi2=m2*s^2+b2*s+k2_coup;
Zsource_coup=((L*s+R)*psi1*psi2+Kf^2*s*(psi1+psi2))/(psi1*psi2);
Zmech_coup=Kf*s*(m2*psi1-m1*psi2)/(psi1*psi2);

% PHR method for 1st harvester of array avg pow gen
[magZs phaseZs]=bode(Zsource_coup,w);
```

```
magZs=squeeze(magZs);
phaseZs=squeeze(phaseZs);
[magZservo phaseZservo]=bode(Zservo_coup,w);
magZservo=squeeze(magZservo);
phaseZservo=squeeze(phaseZservo);
[magCL phaseCL]=bode(Zservo_coup/(Zsource_coup+Zservo_coup)*Zmech_coup,w);
magCL=squeeze(magCL);
phaseCL=squeeze(phaseCL);
logphr=-log10(magZservo)+2*log10(magCL);
phr=0.5*10.^(logphr).*cos(phaseZservo*pi/180);

phrcoup=phr';   % Basic tuning coup harv PHR curve

% Plot resulting PHR
figure
[hAx, PHR_plot, DFT_plot] = plotyy(freq_range,phrcoup,freq_range,accel_mag_sq);
hold on;
grid on;
xlabel('Freq [Hz]');
ylabel(hAx(1),'PHR [W/(m/s^2)^2]');
ylabel(hAx(2),'Accel amplitude^2 [m/s^2]^2');
hold on;
%% ************************************************************************
% PHR-TUNED COUPLED HARVESTER ***********************************************

m1=0.697;
m2=0.697;
b1=7.294;
b2=7.294;

% Enter vectors to search
k1_vector=([3.039]*2*pi).^2*m1;
k2_vector=([12.1]*2*pi).^2*m2;
RL_vector=[34];

Operations=length(RL_vector)*length(k1_vector)*length(k2_vector)
display(['RL vector length is ' num2str(length(RL_vector))]);
display(['k1 vector length is ' num2str(length(k1_vector))]);
display(['k2 vector length is ' num2str(length(k2_vector))]);
counter=0;

theor_avg_pow=zeros(length(RL_vector),length(k1_vector),length(k2_vector));
%% Running optimization
tic;
for index1=1:1:length(RL_vector)
   RL=RL_vector(index1);
      for index2=1:1:length(k1_vector)
         k1=k1_vector(index2);
         for index3=1:1:length(k2_vector)
            k2=k2_vector(index3);
```

```
            Zservo_coup=tf(RL,1);
            psi1=m1*s^2+b1*s+k1;
            psi2=m2*s^2+b2*s+k2;
            Zsource_coup=((L*s+R)*psi1*psi2+Kf^2*s*(psi1+psi2))/(psi1*psi2);
            Zmech_coup=Kf*s*(m2*psi1-m1*psi2)/(psi1*psi2);

            % PHR method for 1st harvester of array avg pow gen
            [magZs phaseZs]=bode(Zsource_coup,w);
            magZs=squeeze(magZs);
            phaseZs=squeeze(phaseZs);
            [magZservo phaseZservo]=bode(Zservo_coup,w);
            magZservo=squeeze(magZservo);
            phaseZservo=squeeze(phaseZservo);
            [magCL phaseCL]=bode(Zservo_coup/(Zsource_coup+Zservo_coup)*Zmech_coup,w);
            magCL=squeeze(magCL);
            phaseCL=squeeze(phaseCL);
            logphr=-log10(magZservo)+2*log10(magCL);
            phr=0.5*10.^(logphr).*cos(phaseZservo*pi/180);
            phrnew=phr';

            theor_avg_pow(index1,index2,index3)=sum(phrnew.*accel_mag_sq);

            counter=counter+1;
            if mod(counter,50)==0
               display(['Approx ' num2str(toc/(counter/Operations)-toc) ' sec remaining.'])
            end
        end
    end
end

%% Recording results of optimization and plotting phr
Powcoupmax=max(max(max(theor_avg_pow))) % Total pow for PHR-tuned coup harv
[RL_index,k1_index,k2_index] = ind2sub(size(theor_avg_pow),find(theor_avg_pow == Powcoupmax));
% Resistance and stiffnesses that yield the total pow for PHR-tuned coup
% harv
RL_coupmax=RL_vector(RL_index);
k1_coupmax=k1_vector(k1_index);
k2_coupmax=k2_vector(k2_index);

display(['Coupled Harv Conv. Resistive Load Results']);
display(['m1 is ' num2str(m1)]);
display(['m2 is ' num2str(m2)]);
display(['k1 is ' num2str(k1_coupmax)]);
display(['k2 is ' num2str(k2_coupmax)]);
display(['This makes the 1st natural frequency ' num2str(sqrt(k1_coupmax/m1)/(2*pi)) ' Hz']);
display(['This makes the 2nd natural frequency ' num2str(sqrt(k2_coupmax/m2)/(2*pi)) ' Hz']);
display(['b1 is ' num2str(b1)]);
display(['b2 is ' num2str(b1)]);
display(['Rload is ' num2str(RL_coupmax)]);
display(['Conv. array would yield ' num2str(1000*Powcoupmax) ' mW from the excitation']);
display(['End of Coupled Harv Conv. Resistive Load Results']);
```

```
% PHR that yields the most power
Zservo_coup=tf(RL_coupmax,1);
psi1=m1*s^2+b1*s+k1_coupmax;
psi2=m2*s^2+b2*s+k2_coupmax;
Zsource_coup=((L*s+R)*psi1*psi2+Kf^2*s*(psi1+psi2))/(psi1*psi2);
Zmech_coup=Kf*s*(m2*psi1-m1*psi2)/(psi1*psi2);

% PHR method for 1st harvester of array avg pow gen
[magZs phaseZs]=bode(Zsource_coup,w);
magZs=squeeze(magZs);
phaseZs=squeeze(phaseZs);
[magZservo phaseZservo]=bode(Zservo_coup,w);
magZservo=squeeze(magZservo);
phaseZservo=squeeze(phaseZservo);
[magCL phaseCL]=bode(Zservo_coup/(Zsource_coup+Zservo_coup)*Zmech_coup,w);
magCL=squeeze(magCL);
phaseCL=squeeze(phaseCL);
logphr=-log10(magZservo)+2*log10(magCL);
phr=0.5*10.^(logphr).*cos(phaseZservo*pi/180);

phrcoupmax=phr';    % PHR-tuned coupled harv PHR curve

plot(freq_range,phrcoupmax,'r');
%% ************************************************************************
% MPTT COUPLED HARVESTER (PHYSICALLY UNACHIEVABLE) ************************

% Enter vectors to search
k1_vector=([3.039]*2*pi).^2*m1;
k2_vector=([12.3]*2*pi).^2*m2;

Operations=length(k1_vector)*length(k2_vector)
display(['k1 vector length is ' num2str(length(k1_vector))]);
display(['k2 vector length is ' num2str(length(k2_vector))]);
counter=0;

theor_avg_pow=zeros(length(k1_vector),length(k2_vector));
%% Running optimization
tic;
for index1=1:1:length(k1_vector)
   k1=k1_vector(index1);
   for index2=1:1:length(k2_vector)
      k2=k2_vector(index2);

      Zservo_coup=((-L*s+R)*(m1*s^2-b1*s+k1)*(m2*s^2-b2*s+k2)-Kf^2*s*(m1*s^2-
b1*s+k1+m2*s^2-b2*s+k2))/((m1*s^2-b1*s+k1)*(m2*s^2-b2*s+k2));
      psi1=m1*s^2+b1*s+k1;
      psi2=m2*s^2+b2*s+k2;
      Zsource_coup=((L*s+R)*psi1*psi2+Kf^2*s*(psi1+psi2))/(psi1*psi2);
      Zmech_coup=Kf*s*(m2*psi1-m1*psi2)/(psi1*psi2);
```

```
        % PHR method for 1st harvester of array avg pow gen
        [magZs phaseZs]=bode(Zsource_coup,w);
        magZs=squeeze(magZs);
        phaseZs=squeeze(phaseZs);
        [magZservo phaseZservo]=bode(Zservo_coup,w);
        magZservo=squeeze(magZservo);
        phaseZservo=squeeze(phaseZservo);
        [magCL phaseCL]=bode(Zservo_coup/(Zsource_coup+Zservo_coup)*Zmech_coup,w);
        magCL=squeeze(magCL);
        phaseCL=squeeze(phaseCL);
        logphr=-log10(magZservo)+2*log10(magCL);
        phr=0.5*10.^(logphr).*cos(phaseZservo*pi/180);
        phrnew=phr';

        theor_avg_pow(index1,index2)=sum(phrnew.*accel_mag_sq);

        counter=counter+1;
        if mod(counter,50)==0
           display(['Approx ' num2str(toc/(counter/Operations)-toc) ' sec remaining.'])
        end

    end
end

%% Recording results of optimization and plotting phr of ALL ARRAY results
% on p. 59
Powcoupmptt=max(max(theor_avg_pow));    % Total pow for MPTT coup harv
[k1_index,k2_index] = ind2sub(size(theor_avg_pow),find(theor_avg_pow == Powcoupmptt));
% Stiffnesses that yield total pow for MPTT coupled harvester
k1_coupmptt=k1_vector(k1_index);
k2_coupmptt=k2_vector(k2_index);

display(['Coupled Harv. With MPTT-dictated Load Results']);
display(['m1 is ' num2str(m1)]);
display(['m2 is ' num2str(m2)]);
display(['k1 is ' num2str(k1_coupmptt)]);
display(['k2 is ' num2str(k2_coupmptt)]);
display(['This makes the 1st natural frequency ' num2str(sqrt(k1_coupmptt/m1)/(2*pi)) ' Hz']);
display(['This makes the 2nd natural frequency ' num2str(sqrt(k2_coupmptt/m2)/(2*pi)) ' Hz']);
display(['b1 is ' num2str(b1)]);
display(['b2 is ' num2str(b1)]);
display('Zload=Zsource*');
display(['Array with MPTT-dictated loads would yield ' num2str(1000*Powcoupmptt) ' mW from the
excitation']);
display(['End Coupled Harv. With MPTT-dictated Load Results']);

% PHR that yields the most power
Zservo_coup=((-L*s+R)*(m1*s^2-b1*s+k1_coupmptt)*(m2*s^2-b2*s+k2_coupmptt)-Kf^2*s*(m1*s^2-
b1*s+k1_coupmptt+m2*s^2-b2*s+k2_coupmptt))/((m1*s^2-b1*s+k1_coupmptt)*(m2*s^2-
b2*s+k2_coupmptt));
psi1=m1*s^2+b1*s+k1_coupmptt;
```

```
psi2=m2*s^2+b2*s+k2_coupmptt;
Zsource_coup=((L*s+R)*psi1*psi2+Kf^2*s*(psi1+psi2))/(psi1*psi2);
Zmech_coup=Kf*s*(m2*psi1-m1*psi2)/(psi1*psi2);

% PHR method for 1st harvester of array avg pow gen
[magZs phaseZs]=bode(Zsource_coup,w);
magZs=squeeze(magZs);
phaseZs=squeeze(phaseZs);
[magZservo phaseZservo]=bode(Zservo_coup,w);
magZservo=squeeze(magZservo);
phaseZservo=squeeze(phaseZservo);
[magCL phaseCL]=bode(Zservo_coup/(Zsource_coup+Zservo_coup)*Zmech_coup,w);
magCL=squeeze(magCL);
phaseCL=squeeze(phaseCL);
logphr=-log10(magZservo)+2*log10(magCL);
phr=0.5*10.^(logphr).*cos(phaseZservo*pi/180);

phrcoupmptt=phr';   % MPTT coupled harvester PHR curve

plot(freq_range,phrcoupmptt,'k');

%% Summary of total power results for coupled harvester
display(['PHR-tuned coupled harvester would yield ' num2str(1000*Powcoupmax) ' mW from the
excitation']);
display(['Basic tuning of cpoupled harvester would yield ' num2str(1000*Powcoup) ' mW from the
excitation']);
display(['MPTT coupled harvester would yield ' num2str(1000*Powcoupmptt) ' mW from the
excitation']);

%% Formatted figure of PHR-tuned embodiments of each architecture
close all

% Conventional Harvester PHR-tuned
[hAx,hLine1,hLine2] = plotyy(w./(2*pi),phrmaxconv,w./(2*pi),accel_mag_sq);
set(hLine1,'LineStyle','--','LineWidth',2.5)
set(hLine2,'Color','k','LineWidth',1.5);
xlabel('Freq [Hz]')
ylabel(hAx(1),'PHR [W/(m/s^2)^2]');
ylabel(hAx(2),'Acceleration Amplitude Squared [(m/s^2)^2]','Color','k');
set(hAx(2),'YColor','k');
set(hAx(1),'YColor','k');
set(hAx(1),'XLim',[0 25]);
set(hAx(2),'XLim',[0 25]);
set(hAx(1),'YLim',[0 0.03]);
set(hAx(1),'YTick',[0 0.01 0.02 0.03]);
hold on;
grid on;
set(gca,'LooseInset',[0 0 0 0]);

% Harvester array PHR-tuned
plot(w./(2*pi),phrarraymax,'g','LineWidth',2.5);
```

```
% Coupled harvester PHR-tuned
plot(w./(2*pi),phrcoupmax,'r:','LineWidth',2.5);

% Choose a legend (absolute power or normalized)
legend(['Conventional ' num2str(roundn(Powmaxconv,-7)) ' mW ('
num2str(roundn(100*Powmaxconv/Powmaxconv,2)) ' %)'],...
      ['Array ' num2str(roundn(Powarraymax,-7)) ' mW ('
num2str(roundn(100*Powarraymax/Powmaxconv,-1)) ' %)'],...
      ['Coupled ' num2str(roundn(Powcoupmax,-7)) ' mW ('
num2str(roundn(100*Powcoupmax/Powmaxconv,-1)) ' %)']);

% Create arrow
annotation(gcf,'arrow',[0.466071428571429 0.901785714285714],...
   [0.469047619047619 0.469047619047619],'LineWidth',3);
```

REFERENCES

[1] W. J. M. Robert S. Kirk, "Highway Bridge Conditions: Issues for Congress," ed. Online: Congressional Research Service, 2013, p. 12.

[2] J. Kim and J. P. Lynch, "Experimental analysis of vehicle–bridge interaction using a wireless monitoring system and a two-stage system identification technique," *Mechanical Systems and Signal Processing,* vol. 28, pp. 3-19, 4// 2012.

[3] F. H. Administration, "2013 Status of Nation's Highways, Bridges, and Transit: Conditions & Performance," U. S. D. o. Transportation, Ed., ed. Online: Federal Highway Administration, 2013, p. 11.

[4] R. J. D. Heather M. O'Connell and P. M. Bergson., "Fatigue Evaluation of the Deck Truss of Bridge 9340," University of Minnesota, Minnesota Department of Transportation Office of Research 2001.

[5] E. Sazonov, L. Haodong, D. Curry, and P. Pillay, "Self-Powered Sensors for Monitoring of Highway Bridges," *Sensors Journal, IEEE,* vol. 9, pp. 1422-1429, 2009.

[6] C. B. Williams, A. Pavic, R. S. Crouch, and R. C. Woods, "Feasibility study of vibration-electric generator for bridge vibration sensors," in *Proceedings of the 1998 16th International Modal Analysis Conference, IMAC. Part 1 (of 2), February 2, 1998 - February 5, 1998*, Santa Barbara, CA, USA, 1998, pp. 1111-1117.

[7] E. v. K. H. Ronnie K. Miller, Patrick O. Moore, *Nondestructive Testing Handbook*, 3 ed. vol. 6: American Society for Non-destructive Testing, 2005.

[8] J. P. Lynch, K. H. Law, A. S. Kiremidjian, E. Carryer, C. R. Farrar, H. Sohn*, et al.*, "Design and performance validation of a wireless sensing unit for structural monitoring applications," in *US-Korea Workshop on Smart Infrastructural Systems, 23-24 Aug. 2002*, South Korea, 2004, pp. 393-408.

[9] D. Zhu, S. Roberts, M. J. Tudor, and S. P. Beeby, "Design and experimental characterization of a tunable vibration-based electromagnetic micro-generator," *Sensors and Actuators A: Physical,* vol. 158, pp. 284-293, March 2010.

[10] S. P. Beeby, M. J. Tudor, and N. M. White, "Energy harvesting vibration sources for microsystems applications," *Measurement Science and Technology,* vol. 17, pp. R175-R195, 2006.

[11] S. Chalasani and J. M. Conrad, "A survey of energy harvesting sources for embedded systems," in *Southeastcon, 2008. IEEE*, 2008, pp. 442-447.

[12] R. Moghe, Y. Yi, F. Lambert, and D. Divan, "A scoping study of electric and magnetic field energy harvesting for wireless sensor networks in power system applications," in *Energy Conversion Congress and Exposition, 2009. ECCE 2009. IEEE*, 2009, pp. 3550-3557.

[13] L. Wang, T. J. Kazmierski, B. M. Al-Hashimi, S. P. Beeby, and R. N. Torah, "An integrated approach to energy harvester modeling and performance optimization," in *Behavioral Modeling and Simulation Workshop, 2007. BMAS 2007. IEEE International*, 2007, pp. 121-125.

[14] C. Peters, D. Maurath, W. Schock, F. Mezger, and Y. Manoli, "A closed-loop wide-range tunable mechanical resonator for energy harvesting systems," *Journal of Micromechanics and Microengineering,* vol. 19, p. 094004 (9 pp.), 2009.

[15] A. Cammarano, S. G. Burrow, D. A. W. Barton, A. Carrella, and L. R. Clare, "Tuning a resonant energy harvester using a generalized electrical load," *Smart Materials and Structures,* vol. 19, p. 055003 (7 pp.), May 2010.

[16] V. R. Challa, M. G. Prasad, and F. T. Fisher, "Towards an autonomous self-tuning vibration energy harvesting device for wireless sensor network applications," *Smart Materials and Structures,* vol. 20, 2011.

[17] H. Vocca, I. Neri, F. Travasso, and L. Gammaitoni, "Kinetic energy harvesting with bistable oscillators," *Applied Energy,* vol. 97, pp. 771-776, 2012.

[18] D. Zhu, M. J. Tudor, and S. P. Beeby, "Strategies for increasing the operating frequency range of vibration energy harvesters: A review," *Measurement Science and Technology,* vol. 21, 2010.

[19] D. Zhu, "Chapter 2: Vibration Energy Harvesting: Machinery Vibration, Human Movement and Flow Induced Vibration," in *Sustainable Energy Harvesting Technologies - Past, Present and Future*, Y. K. Tan, Ed., ed: InTech, 2011, pp. 25-40.

[20] A. V. Pedchenko, J. W. Hoke, and E. J. Barth, "A control approach for broadening the operating frequency range of a bridge vibration energy harvester," in *ASME 2011 Dynamic Systems and Control Conference and Bath/ASME Symposium on Fluid Power and Motion Control, DSCC 2011, October 31, 2011 - November 2, 2011*, Arlington, VA, United states, 2011, pp. 209-216.

[21] Z. Dibin, S. Roberts, M. J. Tudor, and S. P. Beeby, "Closed loop frequency tuning of a vibration-based micro-generator," in *8th International Workshop on Micro and Nanotechnology for Power Generation and Energy Conversion Applications with the 2nd Symposium on Micro Environmental Machine Systems, 9-12 Nov. 2008*, San Diego, CA, USA, 2008, pp. 229-32.

[22] A. Shahabadi, "Bridge Vibration Studies : Interim Report," Purdue University, West Lafayette, IN1977.

[23] I. Sari, T. Balkan, and H. Kulah, "A Wideband Electromagnetic Micro Power Generator for Wireless Microsystems," in *Solid-State Sensors, Actuators and Microsystems Conference, 2007. TRANSDUCERS 2007. International*, 2007, pp. 275-278.

[24] M. Ferrari, V. Ferrari, M. Guizzetti, D. Marioli, and A. Taroni, "Piezoelectric multifrequency energy converter for power harvesting in autonomous microsystems," *Sensors and Actuators A: Physical,* vol. 142, pp. 329-335, 3/10/ 2008.

[25] M. Lallart, S. R. Anton, and D. J. Inman, "Frequency Self-tuning Scheme for Broadband Vibration Energy Harvesting," *Journal of Intelligent Material Systems and Structures,* vol. 21, pp. 897-906, 2010.

[26] J. A. Bowden, S. G. Burrow, A. Cammarano, L. R. Clare, and P. D. Mitcheson, "Switched-Mode Load Impedance Synthesis to Parametrically Tune Electromagnetic Vibration Energy Harvesters," *Mechatronics, IEEE/ASME Transactions on,* vol. 20, pp. 603-610, 2015.

[27] J. M. Renno, M. F. Daqaq, and D. J. Inman, "On the optimal energy harvesting from a vibration source," *Journal of Sound and Vibration,* vol. 320, pp. 386-405, 2/6/ 2009.

[28] S. P. Beeby, R. N. Torah, M. J. Tudor, P. Glynne-Jones, T. O. Donnell, C. R. Saha*, et al.*, "A micro electromagnetic generator for vibration energy harvesting," *Journal of Micromechanics and Microengineering,* vol. 17, p. 1257, 2007.

[29] X. Tang and L. Zuo, "Enhanced vibration energy harvesting using dual-mass systems," *Journal of Sound and Vibration,* vol. 330, pp. 5199-5209, 10/10/ 2011.

[30] N. G. Stephen, "On the maximum power transfer theorem within electromechanical systems," *Proceedings of the Institution of Mechanical Engineers, Part C: Journal of Mechanical Engineering Science,* vol. 220, pp. 1261-1267, 2006.

[31] N. Kong, D. S. Ha, A. Erturk, and D. J. Inman, "Resistive Impedance Matching Circuit for Piezoelectric Energy Harvesting," *Journal of Intelligent Material Systems and Structures,* vol. 21, pp. 1293-1302, 2010.

[32] L. L. Howell, in *Compliant Mechanisms*, 1st ed New York, NY: Wiley-Interscience, 2001, p. 410.

[33] M. Gioffre, V. Gusella, R. Marsili, and G. Rossi, "Comparison between accelerometer and laser vibrometer to measure traffic excited vibrations on bridges," in *4th International Conference on Vibration Measurements by Laser Techniques: Advances and Applications, June 21, 2000 - June 23, 2000*, Ancona, Italy, 2000, pp. 230-238.

[34] M. Wang, "Embedded Strain Sensor With Power Scavenging From Bridge Vibration," Master of Science Master's, Civil Engineering, University of Maryland, 2004.

[35] N. G. Stephen, "On energy harvesting from ambient vibration," *Journal of Sound and Vibration,* vol. 293, pp. 409-425, 2006.

[36] R. J. Allemang and D. L. Brown, "A Correlation Coefficient for Modal Vector Analysis," in *1st International Modal Analysis Conference*, Orlando, USA, 1982, pp. 110-116.

[37] T. Galchev, J. McCullagh, R. L. Peterson, and K. Najafi, "Harvesting traffic-induced bridge vibrations," in *Solid-State Sensors, Actuators and Microsystems Conference (Transducers), 2011 16th International*, 2011, pp. 1661-1664.

[38] C. R. F. Hoon Sohn, Francois M Hemez, Devin D. Shunk, Daniel W. Stinemates, Brett R. Nadler, Jerry J. Czarnecki, "A Review of Structural Health Monitoring Literature: 1996-2001," Los Alamos National Laboratory LA-13976-MS, 2004.

[39] S. Cheng, N. Wang, and D. P. Arnold, "Modeling of magnetic vibrational energy harvesters using equivalent circuit representations," *Journal of Micromechanics and Microengineering,* vol. 17, pp. 2328-2335, 2007.

[40] S. Adhikari, M. I. Friswell, and D. J. Inman, "Piezoelectric energy harvesting from broadband random vibrations," *Smart Materials and Structures,* vol. 18, p. 115005, 2009.

[41] P. Constantinou, P. H. Mellor, and P. D. Wilcox, "A Magnetically Sprung Generator for Energy Harvesting Applications," *Mechatronics, IEEE/ASME Transactions on,* vol. 17, pp. 415-424, 2012.

[42] Q. Tang and X. Li, "Two-Stage Wideband Energy Harvester Driven by Multimode Coupled Vibration," *Mechatronics, IEEE/ASME Transactions on,* vol. 20, pp. 115-121, 2015.

[43] A. V. Pedchenko, E. B. Pitt, and E. J. Barth, "Analytical Tools for Investigating Stability and Power Generation of Electromagnetic Vibration Energy Harvesters," *Mechatronics, IEEE/ASME Transactions on,* vol. PP, pp. 1-1, 2015.

[44] R. J. Allemang, Brown, D.L., "A Complete Review of the Complex Mode Indicator Function (CMIF) with Applications," in *International Conference on Noise and Vibration Engineering (ISMA)*, Leuven, Belgium, 2006.

[45] G.-D. Zhou and T.-H. Yi, "A Summary Review of Correlations between Temperatures and Vibration Properties of Long-Span Bridges," *Mathematical Problems in Engineering,* vol. 2014, p. 19, 2014.